Advanced Radiation Pressure Modelling for Improving the Satellite Thermosphere Density and Wind Observations

Natalia Anna Hładczuk

ADVANCED RADIATION PRESSURE MODELLING FOR IMPROVING THE SATELLITE THERMOSPHERE DENSITY AND WIND OBSERVATIONS

ADVANCED RADIATION PRESSURE MODELLING FOR IMPROVING THE SATELLITE THERMOSPHERE DENSITY AND WIND OBSERVATIONS

Dissertation

for the purpose of obtaining the degree of doctor
at Delft University of Technology,
by the authority of the Rector Magnificus, prof.dr.ir. Hester Bijl,
chair of the Board of Doctorates,
to be defended publicly on Thursday 9 July 2026 at 12:30

by

Natalia Anna HŁADCZUK

This dissertation has been approved by the promotor and copromotor.

Composition of the doctoral committee:

Rector Magnificus	chairperson
Prof.dr.ir. P.N.A.M Visser	Delft University of Technology, *promotor*
Dr. C. Siemes	Delft University of Technology, *copromotor*
Independent members:	
Prof.dr.ir. M. Mulder	Delft University of Technology
Prof.dr.ing. E. Forootan	Aalborg Univesity, Denmark
Dr. T. Sarris	Democritus University of Thrace, Greece
Prof.dr.ing. T. Mayer-Gürr	Technische Universität Graz, Austria
Dr. G. March	European Space Agency, The Netherlands
Prof.dr. L.L.A. Vermeersen	Delft University of Technology, *reserve member*

Keywords: Thermosphere, Neutral mass density, Neutral winds, Satellite thermal emission, Radiation pressure, Uncertainty propagation

Printed by: Ipskamp Printing

Cover by: Natalia Hładczuk

Front & Back: The temperature profiles of the GRACE-FO left (front) and right (back) solar arrays during 2020. Each horizontal line represents one orbital revolution. The color scale ranges from blue to red, corresponding to low and high temperatures, respectively, within the 100–400 K range. Data gaps were removed for aesthetic purposes (Figure 2.2, Chapter 2).

ISBN 978-94-6536-165-9

An electronic version of this dissertation is available at
http://repository.tudelft.nl/.

The world is full of great and
wonderful things for those
who are ready for them.

—Moominpappa
Moominpappa at Sea
Tove Jansson

CONTENTS

SUMMARY

Knowledge of thermosphere mass density and wind is essential for a wide range of applications, including the development of thermosphere models and advancing the understanding of thermosphere–ionosphere coupling and solar–terrestrial physics. It is also widely used in space operations, such as mission planning, fuel budget estimation, reentry prediction, and collision risk assessment. Thermosphere mass density and wind can be obtained in situ from accelerometer measurements onboard Low Earth Orbit (LEO) satellites combined with precise GNSS positioning. Since the beginning of the 21st century, numerous LEO satellites equipped with accelerometers have been launched, providing several invaluable mass density and wind datasets. This dissertation focuses on two accelerometer-carrying LEO missions: the Gravity Field and Steady-State Ocean Circulation Explorer (GOCE), which was part of ESA's Living Planet Program, and the Gravity Recovery and Climate Experiment Follow-On (GRACE-FO), a joint initiative between NASA and DLR.

The accuracy of the accelerometer-derived thermosphere mass density and wind datasets is coupled with uncertainties in the aerodynamic and radiation pressure modelling, where the latter plays a major role, especially during the periods of low solar activity. This dissertation aims to advance the radiation pressure models for GRACE-FO and GOCE. This is achieved by using satellites' high-fidelity geometries supplemented by the thermo-optical properties of the surface materials. These thermo-optical properties are first redefined and fine-tuned using numerical optimisation, satellite photos and synergy with other missions. Finally, the augmented satellite models are analysed using the ray-tracing technique, which additionally accounts for self-shadowing and multiple reflections, to derive the force coefficients.

For Earth-orbiting satellites, the thermal radiation pressure accounts for one-fifth of the total cross-track radiation pressure acceleration. This research utilises the thermal model based on the concept of thermal inertia, in which the satellite heats up by absorbing incoming radiation and cools down by emitting radiation. This process was implemented using thermal model control parameters such as the internal heat generation from batteries and onboard electronics, heat capacity of the panels, conductance towards the satellite's inner parts, and efficiency of the solar panels. Moreover, this research leverages in-situ measurements from onboard thermistors, which provide additional insights for selecting realistic thermal model control parameters.

The goal of this dissertation was to improve the accelerometer-derived thermosphere mass density and wind datasets of the GRACE-FO and GOCE satellites by advancing the modelling of radiation pressure and satellite thermal emission. The newly produced datasets were then compared with the previously available products and models. Additionally, the impact of introducing various modelling approaches was assessed and quantified.

Current accelerometer-derived thermosphere mass density and wind data are provided without comprehensive uncertainty information. This information is particularly important for data assimilation and for comparing thermosphere products obtained by different measurement techniques. This dissertation builds on the recently developed thermosphere density error propagation method and extends it to propagate errors in wind data. In this research, a sensitivity analysis was performed to assess the impact of uncertainties arising from measurement noise, radiation pressure, relative velocity, and aerodynamics on the GRACE-B satellite thermosphere mass density and wind data. The objective of this study was to explore the potential of the propagation tool to augment the existing density and crosswind datasets with uncertainty information.

SAMENVATTING

Kennis van de massadichtheid en de wind in de thermosfeer is essentieel voor een breed scala aan toepassingen, waaronder de ontwikkeling van thermosfeermodellen en het vergroten van het begrip van de thermosfeer-ionosfeer koppeling en zonne-terrestrische fysica. Het wordt ook veel gebruikt in ruimtevaartoperaties, zoals missieplanning, schatting van brandstofverbruik, voorspelling van terugkeer in de atmosfeer en van mogelijke botsingen. De massadichtheid en wind in de thermosfeer kunnen in situ worden verkregen uit versnellingsmetermetingen aan boord van Low Earth Orbit (LEO) satellieten, gecombineerd met nauwkeurige GNSS-positiebepaling. Sinds het begin van de 21e eeuw zijn tal van LEO-satellieten uitgerust met versnellingsmeters gelanceerd, die verschillende waardevolle datasets over massadichtheid en wind hebben opgeleverd. Dit proefschrift richt zich op twee LEO-missies met versnellingsmeters: de Gravity Field and Steady-State Ocean Circulation Explorer (GOCE), die deel uitmaakte van ESA's Living Planet Program, en de Gravity Recovery and Climate Experiment Follow-On (GRACE-FO), een gezamenlijk initiatief van NASA en DLR.

De nauwkeurigheid van de uit versnellingsmeters afgeleide massadichtheid en wind in de thermosfeer hangt samen met onzekerheden in de modellering van aerodynamische en stralingsdruk, waarbij die laatste een grote rol speelt, vooral tijdens perioden met lage zonneactiviteit. Dit proefschrift heeft als doel de stralingsdrukmodellen voor GRACE-FO en GOCE verder te ontwikkelen. Dit wordt gerealiseerd door gebruik te maken van zeer gedetailleerde satellietgeometrieën die worden aangevuld met de thermo-optische eigenschappen van de uitwendige materialen. Deze thermo-optische eigenschappen worden eerst opnieuw gedefinieerd en verfijnd met behulp van numerieke optimalisatie, satellietfoto's en synergie met andere missies. Tot slot worden de gedetailleerde satellietmodellen geanalyseerd met behulp van de ray-tracingtechniek, die bovendien rekening houdt met zelfschaduw en meervoudige reflecties, om zo de krachtcoëfficiënten af te leiden.

Voor satellieten die om de aarde draaien, is de thermische stralingsdruk verantwoordelijk voor een vijfde van de totale zijdelingse stralingsdrukversnelling. In dit onderzoek wordt gebruikgemaakt van het thermische model dat gebaseerd is op het concept van thermische inertie, waarbij de satelliet opwarmt door het absorberen van inkomende straling en afkoelt door het uitzenden van straling. Dit proces is geïmplementeerd met behulp van controleparameters voor het thermische model, zoals de interne warmteontwikkeling door batterijen en boordelektronica, de warmtecapaciteit van de panelen, de geleiding naar de binnenkant van de satelliet en de efficiëntie van de zonnepanelen. Daarnaast maakt dit onderzoek gebruik van in-situ-metingen van boordthermistors, die extra inzicht geven bij het kiezen van realistische controleparameters voor het thermische model.

Het doel van deze dissertatie was om de uit versnellingsmeters afgeleide datasets van de massa- en windsnelheid van de thermosfeer, verkregen met de GRACE-FO- en

GOCE-satellieten, te verbeteren door het modelleren van stralingsdruk en thermische emissie van de satellieten verder te ontwikkelen. De nieuw geproduceerde datasets zijn vervolgens vergeleken met eerder beschikbare producten en modellen. Daarnaast werd de impact van het toepassen van verschillende modelleerbenaderingen geëvalueerd en gekwantificeerd.

Huidige datasets van uit versnellingsmeters afgeleide massadichtheid en wind in de thermosfeer worden aangeboden zonder uitgebreide onzekerheidsinformatie. Deze informatie is met name belangrijk voor data-assimilatie en voor het vergelijken van thermosfeerproducten verkregen met verschillende meettechnieken. Dit proefschrift bouwt voort op de recent ontwikkelde methode voor foutvoortplanting van thermosfeermassadichtheid en breidt deze uit om ook fouten in windgegevens te kunnen voortplanten. In dit onderzoek werd een gevoeligheidsanalyse uitgevoerd om de impact te beoordelen van onzekerheden die voortkomen uit meetruis, stralingsdruk, relatieve snelheid en aerodynamica op de massadichtheid- en windgegevens van de GRACE-B-satelliet. Het doel van deze studie was om de potentie van het propagatie-instrument te verkennen om de bestaande densiteits- en crosswind-datasets aan te vullen met onzekerheidsinformatie.

1

INTRODUCTION

The conceptual boundary that defines the frontier of space is the so-called Kármán line. Below it lie the layers of the atmosphere most familiar to humans, where most weather phenomena form, commercial flights operate, and the ozone layer protects life on Earth from harmful ultraviolet radiation. Above the Kármán line (100 km altitude) we enter the realm of space, into the **thermosphere**. In this layer, we no longer experience weather as it is known on Earth; instead, we encounter space weather phenomena, driven by the activity of the Sun. Though unfavourable to human life, the thermosphere hosts some of the most beautiful natural phenomena: the Aurora Borealis and Aurora Australis. These stunning displays occur when some of the charged particles from solar wind penetrate the Earth's magnetosphere and interact with atmospheric gases.

The thermosphere is also where many of the Low Earth Orbit satellites operate, continuously orbiting the Earth, roughly every 90 minutes, allowing us to enjoy high-speed internet access, precise weather forecasting, and timely warnings about natural hazards, such as floods or wildfires.

In recent years, the growing demand and availability of space technologies have led to an exponential increase in space traffic in Low Earth Orbit. Moreover, many satellites remain in space even after the end of their operational lifetime, sometimes fragmenting into dangerous clouds of debris. Increased congestion in Low Earth Orbit amplifies the likelihood of collisions. This could potentially trigger a cascade of an increasingly dense population of debris around Earth, eventually impeding the satellite operations and manoeuvres, causing what is called the Kessler Syndrome (Kessler & Cour-Palais, 1978). With increasing launch rates and without active space debris removal systems, this poses one of the most challenging risks of the modern space era.

The Low Earth Orbit satellites operating within the thermosphere layer (between 100 km to 600 km) encounter various orbital perturbations, with aerodynamic drag being the biggest one after gravity. The density of the thermosphere is at least a billion times lower compared to the air density we experience at Earth's surface. However, due to the high temperatures, the gas particles have high kinetic energy and thus move at high speeds. Although the atmosphere is much thinner than at Earth's surface, repeated

collisions between the gas particles and fast-moving satellites cause aerodynamic drag, which can alter their orbits. Moreover, the variations in thermosphere density result in thermospheric horizontal winds, which affect the dynamics of the upper atmosphere and its interaction with the ionosphere.

Therefore, accurate knowledge of thermosphere density and wind is essential for multiple applications. It is needed for precise prediction of satellite motion to plan space operations, including issuing collision warnings, planning manoeuvres, predicting satellite re-entry, or estimating mission lifetime. Furthermore, it is essential for scientific space missions, where accurate knowledge of the satellites' trajectory is a prerequisite to meet the research objectives. The scientific investigation of solar-terrestrial physics also relies on the thermosphere density and wind measurements for developing mathematical models describing the upper atmosphere's dynamics.

The goal of the dissertation is to improve in-situ thermosphere density and wind datasets using satellite observations. The main focus of this research is modelling the non-gravitational accelerations which act on satellites, besides the aerodynamic drag, specifically: the accelerations due to radiation pressure and satellite thermal emission. Furthermore, this work advances the method for quantifying uncertainties in the density and wind datasets.

This chapter introduces the relevant concepts and provides an overview of the topics that will be further elaborated in this work. Sections 1.1.1 and 1.1.2 give background on the thermosphere dynamics, as well as thermosphere modelling and observation techniques. The following two sections 1.2 and 1.3 cover the core of this work: the radiation pressure and thermal emission modelling techniques. Section 1.4 describes the space missions analysed within this dissertation. Last but not least, Section 1.5 summarises the overarching objective of the work and lists research questions.

1.1. THERMOSPHERE

The Earth's atmosphere is composed of five major layers characterised by different composition and temperature profile, which, besides the altitude depends on the solar activity (Figure 1.1). The first layer, spanning from the Earth's surface up to 10 km, is the troposphere. While travelling upward through the troposphere, the atmospheric pressure decreases, causing the air warmed by the Earth's surface to expand and cool. Above the troposphere lies the stratosphere (10 km to 50 km), hosting the ozone layer. The ozone molecules absorb ultraviolet radiation from the Sun, converting it into heat, causing the temperature to rise. In the third layer, called the mesosphere (50 km to 100 km), the temperature gets progressively colder to increase again in the thermosphere (100 km to 600 km), a layer abundant in atomic oxygen and nitrogen molecules absorbing the ultraviolet radiation from the Sun. Below the thermosphere, the mean free path, described as the average distance a gas molecule must travel before colliding with another, is short, resulting in a well-mixed gas. When entering the thermosphere, the mean free path is much longer, which means that the collisions between the satellite and the particles are more frequent than the collisions between particles. We call this a free molecular regime. Above the thermosphere lies the exosphere, whose outer boundary is usually not strictly defined; instead, it gradually extends into the vacuum of space.

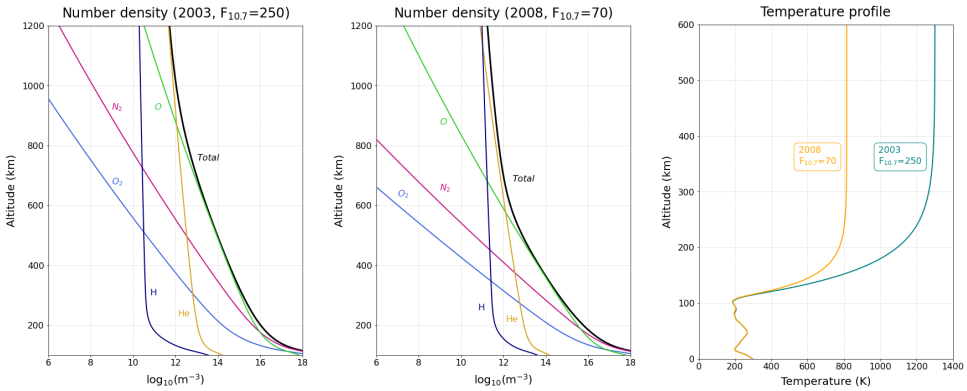

Figure 1.1: Altitude profile for number density (left, middle) and temperature (right) from the NRLMSISE-00 model for high solar activity (1-Nov-2003) and low solar activity (1-Nov-2008) above Bilbao, Spain. The $F_{10.7}$ stands for solar radio flux at a wavelength of 10.7 cm and is provided in solar flux units (sfu), where 1 sfu = $10^{-22}\,\mathrm{Wm^{-2}\,Hz^{-1}}$.

1.1.1. THERMOSPHERE DYNAMICS

The primary source of changes in thermospheric temperature is absorption of ultraviolet (UV) radiation from the Sun (Knipp et al., 2004), which ionises, dissociates, and excites the thermospheric constituents. An increased amount of UV radiation heats the thermosphere, causing it to expand, which results in higher density and consequently in higher aerodynamic drag acting on the satellites. On the contrary, when receiving less UV light, the thermosphere contracts and density decreases. While the solar spectrum remains relatively constant in the visible range, it is highly variable at shorter wavelengths, such as UV and X-rays.

Multiple factors are driving the changes in the thermosphere density, including the Sun-Earth geometry, solar irradiance variability, and geomagnetic activity.

The changes in Sun-Earth geometry result in the **diurnal and seasonal variations**. During the day, the illuminated part of the globe develops a diurnal bulge, resulting in a density increase of up to a factor of 5 at an altitude above 500 km (E. Doornbos, 2011). Variations in the density are also observed, depending on the season, due to the change in the Sun-Earth geometry, including the Sun-Earth distance, and the tilt of Earth's axis. These changes are usually smaller (up to a factor of 1) in comparison to the diurnal variations, with the maximum near the equinoxes, and the minimum in the northern hemisphere in summer, and the southern hemisphere during winter (Paetzold & Zschörner, 1961; Qian et al., 2009).

The second driver is the variability of solar irradiance triggered by the **11-year solar cycle** and **solar rotation**. Approximately every 11 years, the Sun's magnetic poles reverse. During this phase, the Sun is at its most active state, producing more UV radiation together with more frequent outbursts of energy and charged particles. These outbursts usually come from active regions, visible as sunspots. The amplitude of the thermosphere density changes is individual for each solar cycle, but typically increases by a factor of 10 during the solar maximum (at 400 km altitude) (Emmert, 2015). The density changes due to the 27-day solar rotation are smaller, and their effect is mostly

prominent during high solar activity.

Effects mentioned above cause slow, cyclical variations in the thermosphere density. More dynamic, short-lived changes are triggered by **geomagnetic storms** caused by the interaction between the solar wind, consisting of charged particles, and Earth's magnetic field. Such storms can pose operational disturbances for satellites in LEO orbit due to an abrupt increase in aerodynamic drag. One of the recent examples is the geomagnetic storm that occurred in February 2022, causing the loss of 38 deployed Starlink satellites (Fang et al., 2022; He et al., 2023). While the storm was classified as moderate in magnitude, stronger storms, such as the one in May 2024, can result in a density increase of up to six times (Parker & Linares, 2024).

The thermosphere density cannot be decoupled from the thermosphere winds, creating a complex dynamic system that interacts and influences each other. Thermosphere winds have two primary components: horizontal (zonal and meridional) and vertical. Zonal flow refers to the wind that blows parallel to lines of latitude in east-west or west-east direction. The meridional flow indicates north-to-south or south-to-north air motion. Typical horizontal wind speed varies between $0\,\mathrm{m\,s^{-1}}$ to $200\,\mathrm{m\,s^{-1}}$; however, in the polar cap region, it can reach $1000\,\mathrm{m\,s^{-1}}$ (Förster et al., 2008; Lühr et al., 2007).

The horizontal winds are primarily driven by the pressure gradients caused by the spatial differences in the thermosphere density and temperature. The diurnal variation in the thermosphere density drives a strong horizontal wind flow towards the nightside. Around the poles, ions, set in motion by magnetospheric convection, drag the neutral particles, producing high-latitude wind (Förster et al., 2011). This effect is particularly strong during geomagnetic storms.

Contrary to the horizontal winds, the exact drivers for the vertical winds are still not well understood (Larsen & Meriwether, 2012). The magnitude of the vertical wind flow is smaller and more localised, with the strongest wind magnitude observed around the polar caps and aurora oval (Innis & Conde, 2002).

1.1.2. THERMOSPHERE: MODELS AND OBSERVATIONS

Deriving information about the thermosphere density and wind is possible both through models and in-situ observations. There are two main types of thermosphere models: empirical and physics-based. **Physics-based models** rely on first-principles physics and, therefore, allow for a better understanding of the processes driving thermospheric dynamics and have good forecasting capabilities (Mehta et al., 2018). However, this comes at the cost of higher computational demand. Among the most commonly used physics-based models are TIE-GCM (Peymirat, 1998) and WACCM (Liu et al., 2010).

Availability of observational thermospheric data in the 1970s drove the rapid increase in development of **empirical models**. These models use past measurements from multiple instruments to provide a parameterised mathematical description of the thermosphere (Mutschler et al., 2023). Empirical models specify the average behaviour of the thermosphere and are effective for real-time satellite operations, while being less computationally demanding in comparison to the physics-based models. On the other hand, their forecasting capabilities are limited (Mehta et al., 2019). The most commonly used empirical models include NRLMSISE-00 (Picone et al., 2002), Jacchia-Bowman (Bowman et al., 2008), and the DTM-2020 (Bruinsma, 2014). The work presented in this

dissertation relies primarily on NRLMSISE-00 for thermospheric density modelling and dataset comparison.

The most comprehensive empirical wind model currently available is the Horizontal Wind Model (HWM). This model is based on incoherent scatter radar, Fabry–Perot interferometer, rocket and satellite measurements and provides information on zonal and meridional winds. The most recent version of the model, HWM14 (Drob et al., 2015), extended the previous HWM07 (Drob et al., 2008) by including additional satellite and ground-based wind observations.

Besides the two main types, another class are **data-assimilation models**, in which observed measurements are incorporated to update and correct the respective model, either empirical or physics-based, resulting in better forecasting abilities. An example of the assimilative density model is High Accuracy Satellite Drag Model (HASDM) (Storz, 2005), which uses an empirical background model (originally Jacchia 1970) and assimilates satellite drag measurements to produce updated global density fields.

Finally, the thermosphere density and wind can be **observed in-situ** using ground and space-based observations (Lühr et al., 2007). A large amount of wind observations comes from the Fabry-Perot interferometers (FPI) (T. Killeen et al., 1986; Rees et al., 1980). FPIs are optical remote-sensing instruments measuring the Doppler shift of the spectral emission lines from airglow. A number of ground-based FPIs are located in high-latitude regions, around the South and North poles. FPIs have limitations: observations can only be made when it is dark and under clear skies. Besides ground-based observations, multiple spaceborn interferometers successfully measured thermosphere winds onboard satellites such as Dynamics Explorer 2 (DE-2) (T. Killeen & Roble, 1992), Upper Atmosphere Research Satellite (UARS) (Emmert et al., 2001) and the TIMED mission (Thermosphere, Ionosphere, Mesosphere Energetics and Dynamics) (T. Killeen et al., 2006; Niciejewski et al., 2006).

Another ground-based technique for deriving wind data is through incoherent scatter radars, such as EISCAT (Aruliah et al., 1996; Witasse et al., 1998), which consists of multiple radar stations located in Northern Europe. The downside of this type of measurement is its strict limitation to the observation site.

To derive in-situ thermosphere density, the most straightforward and long-established approach is the analysis of the spacecraft orbital decay rate (Swartz et al., 1972). If the spacecraft is additionally equipped with a GNSS receiver, its trajectory can be continuously tracked. This allows to retrieve the thermosphere density using techniques such as precise orbit determination (POD) (van den IJssel et al., 2020), or by monitoring orbital energy dissipation from the semi-major axis (Fitzpatrick et al., 2025).

The most precise technique to derive both thermosphere density and thermosphere wind is to combine a precise GNSS receiver with a high-accuracy onboard accelerometer. In the last 20 years, the number of LEO satellites carrying accelerometers has increased (Section 1.4). Although these missions' primary objectives are typically related to Earth observation, gravimetry, or geodesy, they also enable the retrieval of thermosphere density and wind. These satellites typically carry a high-accuracy electrostatic accelerometer placed in the satellite's centre of mass, sensing non-gravitational accelerations acting on the spacecraft. The working principle of such an accelerometer is based on the measurement of the electrostatic force necessary to maintain the proof-mass motionless with

respect to the surrounding sensor cage (Touboul et al., 1999). The thermosphere density and wind can be derived using information on aerodynamic acceleration, measured by the accelerometer (Bruinsma & Biancale, 2003; Hładczuk et al., 2025; Siemes et al., 2023). However, an accelerometer measures the total non-gravitational acceleration, i.e. besides the aerodynamic force, this instrument also measures other non-gravitational accelerations such as radiation pressure originating from the Sun, Earth, and the satellite itself. To arrive at aerodynamic acceleration, these signals must be separated, which is done using various modelling techniques. The modelling of radiation pressure and thermal emission is the core of this work, and the necessary concepts and details are discussed in Sections 1.2 and 1.3.

1.2. RADIATON PRESSURE ACCELERATION

In January 2008, the NASA MESSENGER robotic space probe was preparing for its first flyby of Mercury. The original flyby plan relied on using the proven strategy of propulsion manoeuvres. However, during the approach phase, the engineers realised that instead of using extra propulsion, a simple adjustment of the solar panels' orientation could produce an additional force, sufficient to successfully perform a flyby (O'Shaughnessy et al., 2009). This additional force was produced by the pressure of photons from the Sun, known as **solar radiation pressure** (SRP). After the success of the first Mercury flyby, the MESSENGER team continued to use SRP, eliminating some planned propulsive manoeuvres. This allowed to save fuel and enabled a planned 1 year orbital mission to be extended to 4 years of operations (Gold et al., 2017).

The example of MESSENGER illustrates the effect of intentional use of the SRP to impact the trajectory of a spacecraft. SRP is the force caused by the exchange of momentum between the photons emitted by the Sun and the satellite's surface. The incoming photons can be either absorbed or reflected, depending on the properties of the materials (Farrés et al., 2023). This concept lies the foundation of solar sailing, an innovative way of propelling a spacecraft without using fuel. The core idea of a solar sail is a large, reflective surface that transfers momentum from photons emitted by the Sun, generating acceleration (Farrés et al., 2023).

Contrary to the missions using the solar sail as a propulsion, most Low Earth Orbit (LEO) satellites treat the SRP as a disturbance. The effect of SRP on LEO satellites is particularly profound during low solar activity. The amount of photons emitted by the Sun in the visible range remains relatively stable through the solar cycle. However, during low solar activity, the Sun produces less ultraviolet radiation, resulting in a less dense thermosphere and thus less aerodynamic drag on satellites. In such a condition, the solar radiation pressure becomes a significant non-gravitational disturbance.

Apart from the Sun, any illuminated planetary body can exert radiation pressure on the spacecraft. In the case of Earth, the **Earth radiation pressure** (ERP) consists of two elements: Earth's infrared emission and planetary albedo. In comparison to the SRP, the effect of ERP on the LEO satellite is smaller, but cannot be neglected for satellite operations (Vielberg & Kusche, 2020).

To evaluate the impact of the SRP and ERP on spacecraft, various models are developed. The most crucial part of these models is the exact knowledge of the spacecraft geometry together with the material properties (Siemes et al., 2023), followed by precisely

modelling the Earth's eclipses (Robertson et al., 2015), and knowledge of Earth albedo, among others.

1.3. THERMAL EMISSION ACCELERATION

A spacecraft continuously loses heat towards its environment through **thermal emission** (P. W. Fortescue et al., 2011), with the largest temperature variation occurring while transitioning from the sunlight into the shadowed part of the orbit. Dissipation of the excess heat generated by spacecraft electronics is usually done by installing radiators. To maintain optimal temperature for its instruments, the spacecrafts are covered in thermal insulation, such as multi-layer insulation (MLI) blankets.

The heat loss results in a thermal acceleration, which, according to the Stefan-Boltzmann law, is proportional to the temperature of the surface to the power of four. Thermal emission, together with the solar radiation pressure and Earth radiation pressure, represents three main non-gravitational radiative forces acting on spacecraft.

A prerequisite for modelling a satellite's thermal emission is accurate knowledge of the materials' infrared absorption and emissivity properties. There are various modelling approaches, ranging from instantaneous heat re-radiation models (Montenbruck et al., 2015; Vielberg & Kusche, 2020), through panel models (Siemes et al., 2023; Y. Wang et al., 2023; Wöske et al., 2019), to finite element models (Vigue et al., 1994). If the spacecraft is additionally equipped with in-situ temperature sensors, the thermal emission model can be additionally verified and improved (Hładczuk et al., 2024).

1.4. ANALYSED LOW EARTH ORBIT MISSIONS

Since the beginning of the 21st century, multiple satellites carrying precise accelerometers have been launched, allowing for continuous in-situ observations of thermospheric density across multiple solar cycles (Figure 1.2).

The mission that paved the way for modern thermospheric density observations was the CHAllenging Minisatellite Payload (CHAMP), launched in 2000. Its objective was to generate exact and simultaneous gravity and magnetic field measurements, and to perform GPS-based radio-occultation measurements for atmospheric profiling. CHAMP was the first mission equipped with a high-precision accelerometer combined with a high-quality dual-frequency GPS receiver (Reigber et al., 2002). Following CHAMP, the Gravity Recovery and Climate Experiment (GRACE) mission was launched in 2002. This pioneering mission consisted of twin satellites that measured temporal changes in Earth's gravity field with unprecedented precision (S. V. Bettadpur, 2007). In 2009, the Gravity Field and Steady-State Ocean Circulation Explorer (GOCE) was launched (Floberghagen et al., 2011a), followed by the three Swarm satellites in 2013 (Olsen et al., 2013). Finally, in 2018, shortly after the decommissioning of GRACE, the GRACE Follow-On (GRACE-FO) mission was placed in orbit. It continues the work of tracking the temporal variations in Earth's gravity field, started by its predecessor, to this day.

This dissertation relies primarily on data from the GOCE and GRACE-FO satellites, which are described in more detail in the following subsections.

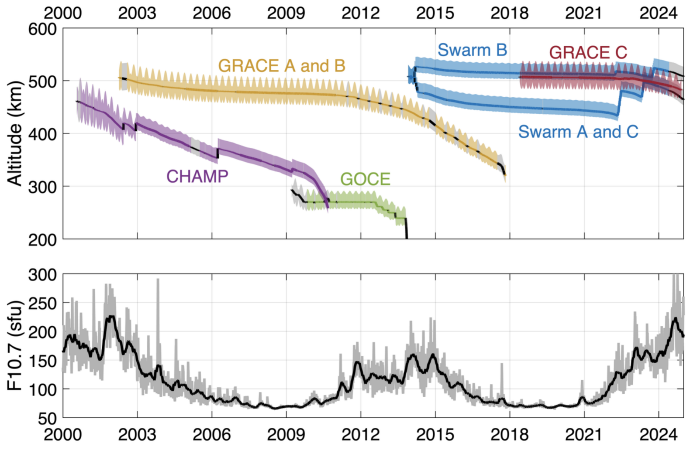

Figure 1.2: Historical and present missions enabling retrieval of thermosphere density and thermosphere wind data. The top panel shows the altitude. The bottom panel shows the solar activity described by 10.7 cm solar radio flux ($F_{10.7}$). 1 sfu = 10^{-22} $Wm^{-2}Hz^{-1}$.

1.4.1. GOCE

The Gravity Field and Steady-State Ocean Circulation Explorer (GOCE), which was launched on 17 of March 2009 and re-entered the atmosphere on 11 November 2013, was the first satellite mission within the framework of the Living Planet Program of the European Space Agency. GOCE operated in a near-circular, Sun-synchronous dusk-dawn orbit. The objective of the mission was to map Earth's gravity field and model the geoid height with unprecedented accuracy and spatial resolution. To make it possible, GOCE was placed close to Earth, just 260 km above the surface. The satellite carried the state-of-the-art Electrostatic Gravity Gradiometer (EGG), measuring the gravity gradients along its orbit. To meet its scientific objectives, the mission design had to comply with stringent mechanical requirements, making the satellite a pioneer in the development of several novel technologies.

The low operational altitude allowed the satellite to precisely sense the small-scale structure of Earth's gravity field. However, this came with the challenge of overcoming increased aerodynamic drag. To mitigate this, GOCE featured a prominent, arrow-shaped aerodynamic design, as visible in Figure 1.3. In addition to its sleek shape, GOCE continuously counteracted aerodynamic drag by employing a novel drag compensation system including electric ion propulsion.

To ensure optimal performance of the scientific instruments, the mission was designed using a large low-expansion 3D carbon–carbon honeycomb structure (Fehringer et al., 2008), assuring structural stability. The satellite subsystems were powered by four body-mounted and two wing-mounted solar panels with triple-junction gallium arsenide (GaAs) solar cells, making GOCE the first gravimetry mission to use this technology.

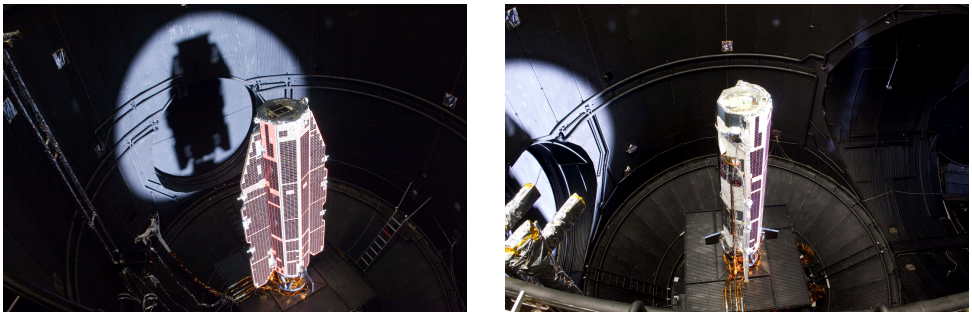

Figure 1.3: GOCE in the Large Space Simulator at ESA's Test Centre in Noordwijk, the Netherlands. Source: ESA Multimedia.

1.4.2. GRACE-FO

The Gravity Recovery And Climate Experiment Follow-On (GRACE-FO) is continuing the successful legacy of the GRACE mission, measuring the temporal changes in Earth's gravity field, to monitor surface mass changes, e.g., due to the terrestrial water cycle. The mission, consisting of the twin satellites shown in Figure 1.4, was launched on 22 May 2018 and continues operation up to this day (Kornfeld et al., 2019). As for GOCE, both satellites carry GPS receivers for precise positioning and timing, and high-accuracy accelerometers. The satellites share the same orbital plane, flying in a near-polar orbit with an initial altitude of approximately 510 km, separated by 220±50 km along the orbit.

Figure 1.4: GRACE-FO twin satellites. Testing the dispenser structure (left). Source NASA. Preparations for the acoustic noise test (right). Source: AIRBUS.

The measurement concept is based on the change in along-track separation between the leading and trailing satellite induced by the gravitational pull (Wolff, 1969). To detect the small variations in the inter-satellite distance, the satellites are equipped with a micrometre-level precision microwave ranging instrument. In addition to the microwave ranging instrument, the mission carries a laser ranging interferometer as a technology demonstration and pathfinder for future gravity missions.

1

1.5. GOAL AND RESEARCH QUESTIONS

Deriving in-situ thermosphere mass density and wind data using accelerometer measurements requires modelling of non-gravitational forces acting on the spacecraft (Section 1.1.2). This dissertation focuses specifically on modelling the forces due to **radiation pressure** and the satellite's **thermal emission**.

The basic approach to modelling radiation pressure relies on a so-called panel model, in which the satellite shape is approximated by a set of flat panels. Each panel is augmented with thermo-optical coefficients describing the surface material's reflective and absorptive properties, enabling the efficient evaluation of radiation pressure using analytic expressions (E. Doornbos, 2011). This approach is suitable for simple, convex satellite shapes but cannot account for self-shadowing and multiple reflections. State-of-the-art approaches overcome this limitation by using highly detailed geometric models of the satellite's shape, also augmented with coefficients describing the surface material's reflective and absorptive properties. This is done in combination with the ray-tracing method, which models the intersection between the rays emitted by the radiation source and the satellite surface (Bhattarai et al., 2022b; Li et al., 2018; Ziebart, 2004). Therefore, the accuracy of the radiation pressure model is driven, among other factors, by knowledge of the satellite geometry and the surface material's thermo-optical properties, which are usually provided by the manufacturer in the satellite handbook. Highly detailed geometric models have been developed for satellites carrying accelerometers (March, Doornbos, & Visser, 2019; Siemes et al., 2023), thereby reducing errors arising from incorrect geometric representation. In contrast, the material's thermo-optical properties are sometimes poorly documented in the satellite handbooks. For instance, the GRACE-FO and its predecessor GRACE mission had the same set of solar panels thermo-optical coefficients specified in the missions' handbooks. However, it is known that GRACE used silicon solar cells, while GRACE-FO used state-of-the-art triple junction gallium arsenide cells (Kornfeld et al., 2019; *NASA GRACE Fact Sheet*, 2004), which results in different cell efficiency and absorption characteristics.

Satellite thermal emission can be modelled using the instantaneous heat re-radiation approach (Montenbruck et al., 2015; Vielberg & Kusche, 2020), which assumes that the absorbed energy is immediately re-emitted as thermal radiation. Such a simplified approach has the advantage that it can be easily applied by solely changing the thermo-optical coefficients, and often is less computationally demanding. However, it does not account for thermal inertia and assumes that there is no heat conduction between satellite panels or heat gain from the satellite's onboard electronics. In recent years, significant progress has been made in modelling of the satellite thermal emission, where state-of-the-art models reproduce the satellite outer temperature, taking into account their thermal inertia (W. Wang et al., 2021; Wöske et al., 2019) and use in-situ temperature measurements from thermistors (Vielberg et al., 2025). Nevertheless, these models still rely on assumptions, e.g., on the heat capacity of the satellite's outer panels, and it is often unclear where thermistors are located, making it difficult to assess how accurately the thermal emission is modelled. A final complication arises for solar arrays, which convert part of the absorbed radiation into electricity instead of heat. To model a solar array's temperature more realistically, a parameter describing the efficiency of the solar cells is introduced (Adhya, 2005; Duan & Hugentobler, 2022; Y. Wang et al., 2023).

The accelerometer measurements not only allow for deriving density and wind observations. They also offer a valuable opportunity to verify advances in radiation pressure and thermal emission modelling. From all satellites carrying accelerometers, the GRACE-FO and the GOCE satellites provide the most precise accelerometer measurements.

The GRACE-FO satellites were launched at an altitude of about 510 km during a period of very low solar activity. In these conditions, the acceleration due to radiation pressure and thermal emission is far larger than the aerodynamic acceleration. Therefore, when comparing modelled non-gravitational accelerations with calibrated accelerometer measurements, differences are expected to arise primarily from errors in radiation pressure and thermal emission. Such differences can be used as input for numerically optimising the thermo-optical coefficients, while also leveraging documentation and photos of the satellites, as well as similarities to other satellites, e.g., GRACE or the Swarm satellites. Furthermore, the GRACE-FO satellites have thermistors located on the outside of the solar arrays, enabling the estimation of the thermal emission model's parameters.

In contrast, the GOCE satellite was orbiting at an extremely low altitude of approximately 250 km, experiencing much larger aerodynamic accelerations than the GRACE-FO satellites. Consequently, errors in modelling radiation pressure and thermal emission are expected to have a much smaller impact on GOCE density and wind observations compared to those from GRACE-FO. Thus, the GOCE satellite serves to test whether accurate modelling of radiation pressure and thermal emission is relevant at such low altitudes, when the objective is to derive thermosphere mass density and wind observations. Further, several thermistors were placed on the backside of the GOCE satellite's wings, enabling further verification of the thermal emission model.

Based on the above, the overarching objective of this dissertation can be defined as follows:

The goal of this dissertation is to improve the accelerometer-derived thermosphere mass density and wind datasets of the GRACE-FO and GOCE satellites by advancing the modelling of radiation pressure and satellite thermal emission.

This goal can be achieved by answering the following research questions:

1. How do various radiation pressure modelling approaches affect the modelled radiation pressure acceleration?

2. What thermal emission modelling accuracy can be achieved using the data from the satellite on-board thermistors, and what are the associated limitations?

3. What is the impact of enhanced radiation pressure and thermal emission modelling on the thermosphere mass density and wind observations derived from accelerometer measurements?

Accelerometer-based in-situ thermosphere mass density and wind data are subject to uncertainties, which are particularly relevant for data assimilation and observation-

model comparison purposes. Quantifying these uncertainties is difficult due to the number and diversity of error sources. Recently, a method for propagating the errors and quantifying their impact on thermosphere density observations was developed by Siemes et al. (2024). However, the method neither addresses wind observations nor identifies the error sources to which density and wind observations are most sensitive. Thus, an additional objective of this dissertation is to extend the method developed by Siemes et al. (2024) to quantify the uncertainty in wind observations and identify which parameters have the most significant impact on the output uncertainty.

This leads to the additional research question:

4. Which parameters are the most impactful drivers on the thermosphere mass density and winds uncertainty?

The first three research questions are addressed in both Chapter 2 (Hładczuk et al., 2024) and Chapter 3 (Hładczuk et al., 2025). While Chapter 2 focuses on the GRACE-FO satellite, Chapter 3 answers these questions for GOCE. The fourth research question is answered in Chapter 4. Finally, Chapter 5 concludes this research and includes recommendations for future missions, as well as an outlook on future work.

2

GRACE-FO RADIATION PRESSURE MODELLING FOR ACCURATE DENSITY AND CROSSWIND RETRIEVAL

N.A. Hładczuk, J. van den IJssel, T.Kodikara, C. Siemes, P.N.A.M. Visser

Uncertainties in radiation pressure modelling play a significant role in the thermospheric density and crosswind observations derived from the GRACE-FO accelerometer, especially during low solar activity. Under such conditions, the radiation pressure acceleration matches the magnitude of the aerodynamic acceleration along the track and exceeds it in the cross-track direction. The GRACE-FO mission has been operating for several years at such high altitudes during both low and rising solar activity, providing a perfect opportunity to study the effects of radiation pressure. This research uses ray tracing based on a high-fidelity satellite geometry model to calculate the radiation pressure acceleration. We numerically fine-tuned the coefficients describing the thermo-optical surface properties to obtain more accurate radiation pressure accelerations than those specified in the GRACE-FO mission manual. We also used in-situ temperature measurements from thermistors on the solar arrays to model the satellite's thermal emission. These temperature measurements allowed a realistic setup of the thermal model, extended by the parameter describing the efficiency of the solar cells, and reproduced the acceleration of the thermal emission with an accuracy of RMS $0.148\,\mathrm{nm\,s^{-2}}$*. The combination of the updated thermal*

This chapter has been published in Advances in Space Research **73**(5), 2355-2373, 2024 Hładczuk et al., 2024.

model and the fine-tuning of the surface coefficients improved the accuracy of the crosswind acceleration to an RMS of $0.55\,\mathrm{nm\,s^{-2}}$*, compared to an RMS of* $4.22\,\mathrm{nm\,s^{-2}}$ *when using panel models and instantaneous thermal radiation. We compared the observed crosswind with two models: HWM14 and TIE-GCM. While both models capture most of the salient features of the observed crosswind, HWM14 shows particularly good agreement at high latitudes. Compared to the previously employed radiation pressure model, the crosswind observations have been improved in low and mid-latitudes, especially during periods of higher solar activity. Since the effect of radiation pressure is most significant in the crosswind direction, the effect on density was small compared to previously published datasets.*

2.1. INTRODUCTION

The Gravity Recovery And Climate Experiment Follow-On (GRACE-FO) mission's primary objective is measuring Earth's time-variable gravity field to deduce mass changes with high precision. GRACE-FO was launched in May 2018 and remains operational until today. The mission consists of two identical satellites flying in a near-polar orbit around Earth at an initial altitude of approximately 510 km (Kornfeld et al., 2019), and a current altitude of 500 km, as of September 2023. The satellites share the same orbital plane with a nominal along-track separation of 220±50 km, continuously measuring the relative distance between each other. GRACE-FO extends the scientific legacy of its predecessor, the GRACE mission (Tapley et al., 2004). Both missions share the same principal design features, however, a laser-ranging interferometer was added to GRACE-FO as a technology demonstration. The GRACE-FO satellites are equipped with a dual-frequency GPS receiver, star trackers and high-precision accelerometers. These instruments allow for measuring the non-gravitational forces acting on the satellites, from which we deduce neutral mass density and crosswind observations (E. Doornbos, 2011). Shortly after launch, the GRACE-D accelerometer data degraded, and its measurements were replaced by a synthetic data transplant (Landerer et al. (2020), Harvey et al. (2022)). Therefore, this article focuses solely on the better-performing GRACE-C satellite. This study will enhance the radiation pressure and thermal emission models for GRACE-FO to obtain a more accurate neutral mass density and crosswind dataset, which complements earlier published data from the CHAMP, GRACE, GOCE, and Swarm missions (Siemes et al., 2023). Producing thermosphere density and crosswind observations relies on the aerodynamic acceleration obtained by subtracting the radiation pressure from the calibrated acceleration. Therefore, uncertainties in the radiation pressure modelling propagate directly into the density and crosswind datasets. This effect is particularly profound for GRACE-FO altitude during low solar activity. In such conditions, the radiation pressure matches the magnitude of the aerodynamic acceleration in the along-track direction and even surpasses it in the cross-track. Since the GRACE-FO mission has been operating for several years at such high altitudes during both low (2018–2021) and rising solar activity, it provides a perfect opportunity to study the effects of radiation pressure. The foundation of the non-gravitational force modelling is the definition of the satellite geometry model. Its complexity varies, starting from the straightforward approach based on a satellite panel model. Such a model implies using a limited number of flat panels to characterise the satellite's outer geometry (S. Bettadpur, 2012). Replacing commonly used panel models with high-fidelity geometries for aerodynamic modelling has increased the accuracy and consistency of thermospheric density and crosswind data (March, Doornbos, & Visser, 2019). To take advantage of the high-fidelity geometry models for the radiation pressure modelling, we must first augment them with thermo-optical surface properties. These models can then be used in ray-tracing simulations to determine the radiation pressure force coefficients. Ray-tracing is an efficient method for modelling the momentum exchange between each ray and satellite surface. It can cope with complex satellite shapes while accounting for self-shadowing and multiple reflections. One way to implement the ray-tracing simulation is to perform calculations for each position along the orbit independently (Kenneally & Schaub, 2020). Regardless of its simple implementation, this method requires high computational resources

and is, therefore, not a feasible option to process the entire GRACE-FO mission data. In this study, we perform the ray-tracing simulations in advance and store the results as a lookup table. This approach is very similar to the one proposed by Klinkrad et al. (1991) and applied by E. Doornbos et al. (2002). It has been later adopted by different groups working on GNSS precise orbit determination (Ziebart (2004), Li et al. (2018), Bhattarai et al. (2022a)).

Thermal acceleration typically accounts for one-fourth of total cross-track radiation pressure acceleration. A common approach to model thermal emission relies on the assumption of simple instantaneous heat reradiation and no heat conduction between and through elements (Montenbruck et al. (2015), Vielberg and Kusche (2020)). The state-of-the-art thermal models reproduce the temperatures of the outer panels, taking into account their thermal inertia (Wöske et al. (2019), Y. Wang et al. (2023)). In this scenario, the satellite surface heats up by absorbing incoming radiation and cools down by emitting radiation. This process can be implemented using thermal model control parameters such as internal heat generation, heat capacity of the panels, and conductance towards the inner parts.

Within the last few years, significant progress has been made in the field of radiation pressure and thermal emission modelling. Nevertheless, specific gaps can still be identified, such as insufficient knowledge of the thermo-optical properties of the satellite material. According to the GRACE-FO Level-1 Data Product User Handbook (Ying et al., 2019), the reflection coefficients do not differ between GRACE and GRACE-FO. However, there are numerous design differences between the two missions. One of them is the solar arrays illustrated in Fig. 2.1, which were upgraded from silicon ones used on GRACE to triple-junction panels (GaAs), previously qualified for the Swarm mission and characterised by higher absorption of visible light (Kornfeld et al., 2019). The need to update the thermo-optical surface properties for GRACE-FO has already been addressed by Siemes et al. (2023). However, the proposed set of reflection coefficients was selected empirically based on the visual inspection of the accelerometer data and prelaunch satellite photos. The same publication introduced the thermal inertia model, with the heat capacity and conductivity of the panels based on the theoretical values of the respective panels. However, it ignored that part of the radiation absorbed by the solar arrays converts to electricity, commonly referred to as the electric efficiency of the solar arrays.

This research aims to provide new insights into selecting the thermo-optical surface coefficients for GRACE-FO using numerical optimisation. Additionally, we tuned a thermal model to accurately match the actual surface temperature measurements obtained from the GRACE-FO thermistors. To achieve even more realistic thermal behaviour, we introduced the efficiency of the solar arrays (Duan & Hugentobler, 2022), which was not the case in previously published GRACE-FO data (Siemes et al., 2023).

This paper is organised as follows. Section 2.2 describes the input data and models used in this study. Section 2.3 elaborates on methodology in the context of thermal emission and radiation pressure modelling. We summarise the results in Section 2.4, comprising the thermal modelling and surface reflection coefficients fine-tuning, the effect on the cross-track acceleration and updated crosswind and density datasets. Finally, Section 2.5 provides conclusions and an outlook on future work.

(a) GRACE-FO[1]

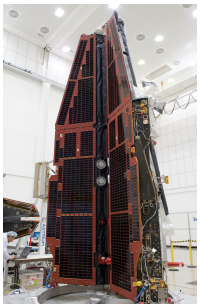

(b) Swarm[2]

(c) GRACE[3]

Figure 2.1: Comparison between the solar arrays of Swarm, GRACE and GRACE-FO.

2.2. DATA AND MODELS

2.2.1. GRACE-FO DATA

This study utilises Level 1 GRACE-FO data publicly available via FTP ftp://isdcftp.gfz-potsdam.de, specifically, the acceleration, attitude, position, velocity, thruster, satellite mass, and accelerometer temperature data. We rely on the higher temporal resolution of the Level 1A accelerometer data to enable easier removal of the acceleration due to thruster activations. Additionally, we use the NRLMSISE-00 model (Picone et al., 2002) to model the atmospheric composition and temperature. Wind in the direction of the satellite's x-axis is accounted for by the HWM07 model (Drob et al., 2008). To measure the non-gravitational accelerations, the GRACE-FO satellites were equipped with the SuperSTAR-FO accelerometers, an advanced version of the ones used previously for the GRACE mission (Christophe et al., 2015). The accelerometer noise level in the along-track is about 0.1 nm s^{-2}, whereas the cross-track measurements are about 10 times less precise by design.

[1] URL https://www.airbus.com/en/newsroom/press-releases/2017-05-grace-fo-satellites-get-an-earful, accessed on 03/10/2023.

[2] URL https://www.esa.int/ESA_Multimedia/Images/2012/02/Swarm_constellation_in_IABG_cleanroom2, accessed on 03/10/2023.

[3] URL https://www.wetteronline.de/wetternews/astro, accessed on 19/10/2023.

2.2.2. THERMISTOR DATA

This study took advantage of in-situ measurements from GRACE-FO thermistors provided by NASA Jet Propulsion Laboratory (JPL) to select realistic thermal model control parameters. Thermistors monitor the temperature on the inner and outer satellite's surfaces in several locations. Sensors on the solar arrays were particularly useful since they provided the most representative temperature readings due to their external location. Numerous other thermistors were mounted on the inner side of the panels or below insulating foils, making their measurements unsuitable for thermal analysis.

Fig. 2.2 shows the location of the temperature sensors on GRACE-FO solar arrays and their registered temperature measurements for the year 2020. The horizontal and vertical axis of the temperature data correspond to time and the argument of latitude. Each column denotes a single orbital revolution, where 0° is the ascending equator crossing, 90° indicates the northernmost point of the orbit, 180° marks the descending equator crossing, and 270° is the southernmost point of the orbit. The 360° point marks the start of the next revolution at the equator.

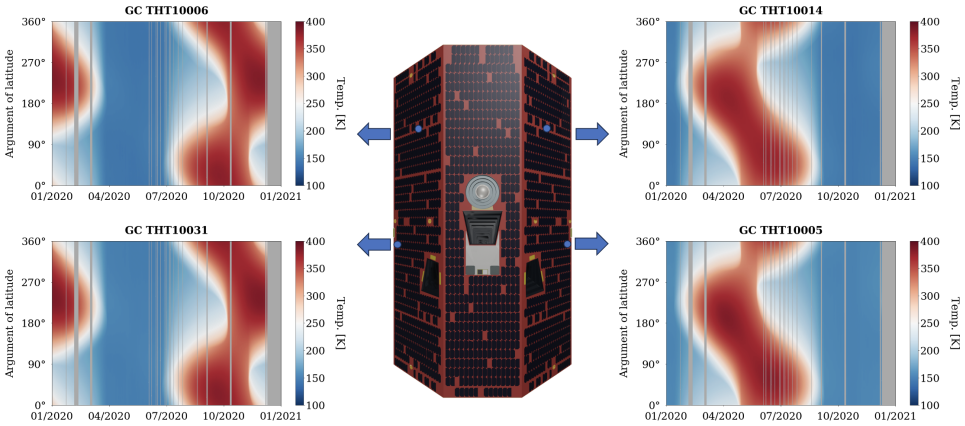

Figure 2.2: GRACE-FO top view with the thermistors' location on solar arrays (indicated by blue dots) and corresponding temperature measurements. The thermistors' IDs are indicated in the title (e.g., THT10014). The grey colour indicates data gaps.

We compared the temperature readings from thermistors on the same panel to examine thermal gradients across the surface. Thermistors located closer to the satellite's rear register at maximum 10 K higher temperatures, in comparison to the central sensors (Fig. 2.3). We consider such temperature differences small enough to assume a uniform temperature over the whole panel area.

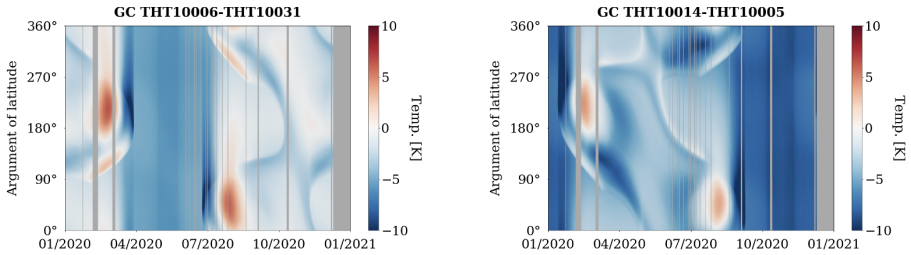

Figure 2.3: Comparison between the temperature measurements from thermistors on the same solar array. The thermistors' IDs are indicated in the title (e.g., THT10014).

2.2.3. GEOMETRY MODELS

Accurate aerodynamic and radiation pressure modelling requires detailed satellite geometries rather than simple panel models. Such geometries were already created for multiple low Earth orbit satellites such as CHAMP, Swarm, GOCE and GRACE (March, Doornbos, & Visser, 2019). This article relies on the high-fidelity GRACE-FO geometry (Fig. 2.4), first published by Siemes et al. (2023). This model, which consists of 23,746 facets, acted as a baseline for deriving aerodynamic coefficients and calculating radiation pressure accelerations. For the radiation pressure modelling, different surface properties were assigned to individual materials, defining absorption and reflection coefficients for both visible and infrared parts of the spectrum. We initially selected the thermo-optical surface properties from the GRACE-FO Level-1 Data Product User Handbook (Ying et al., 2019). For materials that remained unspecified in the documentation, we used the properties specified by P. Fortescue et al. (2011a).

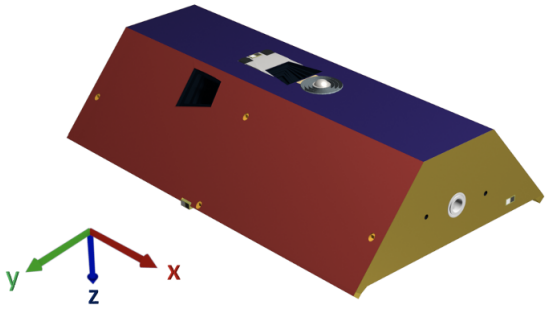

Figure 2.4: Rendered GRACE-FO geometry model used as an input for the ray-tracing algorithm. Colours correspond to individual material properties. The axes are aligned with the satellite reference frame.

2.2.4. TIE-GCM

We use the physics-based thermosphere-ionosphere-electrodynamics general circulation model (TIE-GCM; Richmond et al., 1992) to validate the crosswind data. It is a

time-dependent three-dimensional numerical model of the coupled thermosphere and ionosphere system. This work is based on TIE-GCM version 2.0 (2016) and resolves the system at a horizontal resolution of 2.5°x2.5° in latitude and longitude and a vertical resolution of 0.25 scale height. The exact configuration of the model used in this study along with the simulated data are provided in Kodikara (2023).

2.2.5. HWM14

The Horizontal Wind Model is an empirical model of the horizontal neutral wind in the upper thermosphere. The model consisted primarly of data from two NASA satellites (Explorer 55 and Dynamics Explorer 2), ground-based incoherent scatter radar and Fabry-Perot optical interferometers (FPI). As described in subsection 2.2.1 we used the HWM07 model (Drob et al., 2008) to account for wind in the direction of the satellite's x-axis. However, for the comparison with observation data, we used the most recent model version HWM14, which was updated with ground-based 630 nm FPI measurements in the equatorial and polar regions, as well as cross-track winds from the Gravity Field and Steady State Ocean Circulation Explorer (GOCE) satellite (Drob et al., 2015). The updates in HWM14 fill important gaps in both latitude and local time coverage and provide an improved specification of the upper atmospheric tides and general circulation patterns. Currently, the model does not account for solar activity dependence. The variations with geomagnetic activity are specified via the Ap index.

2.2.6. DTM2020

The Drag Temperature Model (DTM2020) is a semi-empirical model providing information on the Earth's thermosphere temperature, density and compositions (Bruinsma & Boniface, 2021). This study used the operational version of the model to assess the neutral mass density datasets. The DTM2020 is driven by the F10.7 and Kp indices for solar and geomagnetic activity. The core of the model is CHAMP, GOCE and GRACE accelerometer data together with GNSS measurements from the Swarm-A satellite. In addition, very accurate laser tracking data from the Stella satellite have been incorporated.

2.2.7. NRLMSISE-00 MODEL

NRLMSISE-00 is a semi-empirical atmosphere model based on a wide range of data, including mass spectrometer and incoherent scatter radar data. It is also based on neutral mass density datasets derived from accelerometer measurements and orbital decay of objects that flew during the 1960s and 1980s (Picone et al., 2002). We point out that the NRLMSISE-00 model is independent of the density datasets produced after 2000. The model provides the thermosphere density, temperature, and composition. We used the latter two as input for density and crosswind data processing and the first for comparing to the density observations.

2.3. METHODOLOGY

For satellites, such as GRACE-FO, where the accelerometer placement coincides with the satellite's centre of mass, the aerodynamic acceleration vector $\boldsymbol{a}_{\text{aero}}$ can be obtained by subtracting the radiation pressure acceleration, $\boldsymbol{a}_{\text{rp}}$, and thermal acceleration, $\boldsymbol{a}_{\text{the}}$,

from the calibrated accelerometer acceleration, $\boldsymbol{a}_{\text{cal}}$:

$$\boldsymbol{a}_{\text{aero}} = \boldsymbol{a}_{\text{cal}} - \boldsymbol{a}_{\text{rp}} - \boldsymbol{a}_{\text{the}}. \tag{2.1}$$

The total radiation pressure acceleration is the sum

$$\boldsymbol{a}_{\text{rp}} = \boldsymbol{a}_{\text{srp}} + \boldsymbol{a}_{\text{ir}} + \boldsymbol{a}_{\text{alb}}, \tag{2.2}$$

where $\boldsymbol{a}_{\text{srp}}$ stands for the solar radiation pressure acceleration, and $\boldsymbol{a}_{\text{ir}}$ and $\boldsymbol{a}_{\text{alb}}$ are Earth's infrared radiation and albedo, respectively.

Figure 2.4 shows the satellite body-fixed reference frame. During nominal operations, the satellite x-axis is oriented in the anti-flight and in-flight directions for the leading and trailing satellites, respectively. The y-axis corresponds to the direction perpendicular to the orbital plane (cross-track), and the z-axis to the nadir direction (toward Earth). Since the satellite's x-axis is approximately aligned with the flight direction, it captures most of the drag signal. Therefore, we use the x-component of the aerodynamic acceleration, $a_{aero,x}$, to derive the neutral mass density:

$$\rho = \frac{2\, m\, a_{\text{aero},x}}{C_{\text{aero},x}\, V_{rel}^2}. \tag{2.3}$$

Here, m denotes the satellite mass, $C_{aero,x}$ is the x-component of the aerodynamic coefficient vector intrinsically multiplied by the reference area, and V_{rel} is the velocity relative to the atmosphere. Neutral mass density and crosswinds retrieval rely on accurate aerodynamic acceleration estimation, formerly derived using the radiation pressure acceleration (Eq. 2.1). This reliance creates a dependency between the radiation pressure modelling uncertainty and the density and crosswind quality. The impact of radiation pressure modelling errors is most prominent at altitudes above 450 km during low solar activity. In such conditions, the along-track component of radiation pressure acceleration matches or even surpasses the magnitude of the aerodynamic acceleration. This effect was already quantified for the Swarm satellites (van den IJssel et al., 2020), as well as GRACE (Wöske et al., 2019), and GRACE-FO, in which case the radiation pressure acceleration doubled the magnitude of aerodynamic acceleration during deep solar minimum in 2018-2020 (Siemes et al., 2023).

The crosswind retrieval is based on the iterative algorithm proposed by E. Doornbos et al. (2010). In the cross-track direction, the aerodynamic acceleration signal is much smaller (Fig. 2.5), resulting in a strong impact of radiation pressure modelling errors on the crosswind estimate.

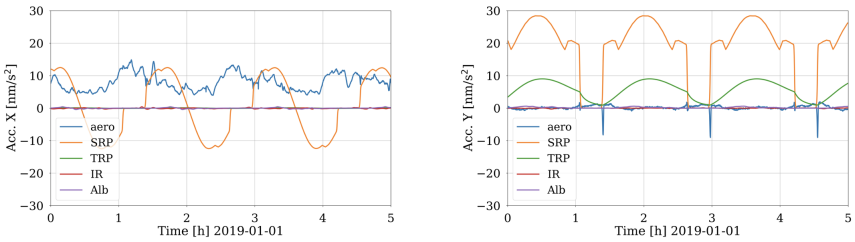

Figure 2.5: Non-gravitational forces acting on the GRACE-C satellite: aerodynamic acceleration (aero), Solar Radiation Pressure (SRP), Thermal Radiation Pressure (TRP), Earth's Infrared radiation (IR), Earth's Albedo (Alb).

This chapter presents the methodology, starting from the radiation pressure modelling approach in Section 2.3.1, complemented by thermo-optical surface coefficients finetuning in Section 2.3.3, and the thermal emission modelling description in Section 2.3.2.

2.3.1. RADIATION PRESSURE MODELLING

Radiation pressure acceleration acting on the satellite can be calculated as

$$\boldsymbol{a}_{\text{ext}}(\alpha,\beta) = \frac{P_{\text{ext}}(\alpha,\beta)}{m}\boldsymbol{C}_{\text{w}}(\alpha,\beta), \tag{2.4}$$

where P_{ext} stands for the radiation pressure originating from external sources such as solar radiation, Earth's infrared radiation and Earth's albedo, $\boldsymbol{C}_w$ is the coefficient integrated over the relevant wavelength domain, and m is the satellite mass. The α and β angles describe the satellite orientation toward the incident radiation. They can be derived using a unit vector fixed to the satellite reference frame, $\boldsymbol{u}_{sat}$, pointing from the radiation source towards the satellite:

$$\boldsymbol{u}_{\text{sat}} = \begin{bmatrix} u_x \\ u_y \\ u_z \end{bmatrix}, \quad \alpha = \arcsin(u_z), \quad \beta = \arctan_2(u_y, -u_z). \tag{2.5}$$

The main contributor to the radiation pressure is solar radiation pressure, commonly defined as

$$P_{\text{srp}} = \left(\frac{1\text{AU}}{\|\boldsymbol{r}_{sat} - \boldsymbol{r}_{Sun}\|}\right)^2 P_{1\text{AU}}, \tag{2.6}$$

where $\boldsymbol{r}_{sat}$ and $\boldsymbol{r}_{Sun}$ are the positions of the satellite and Sun, respectively. $P_{1\text{AU}}$ is the solar radiation pressure at one astronomical unit (AU), commonly calculated as the ratio of the solar constant $\Phi = 1367\,\text{W}\,\text{m}^{-2}$ and the speed of light c, i.e. $P_{1\text{AU}} = \Phi/c = 4.56\,\mu\text{N}\,\text{m}^{-2}$. The calculation of radiation forces originating from Earth's albedo and infrared radiation is described by Vielberg and Kusche (2020), noting that we use monthly averaged albedo and Earth infrared emission maps based on Earth Radiation Budget Experiment (ERBE) satellite data (E. Doornbos et al., 2014).

This study employs a ray-tracing technique to calculate the radiation pressure coefficient $\boldsymbol{C}_w$. This technique uses the high-fidelity GRACE-FO geometry as input, previously described in Section 2.2.3. Ray-tracing simulates the scenario in which a distant radiation source emits parallel rays towards a much smaller satellite body. The algorithm accounts for both self-shadowing and multiple reflections. Emitted rays intersect with the satellite surface and spawn additional rays, whose energy depends on the surface properties. We use the ray tracing technique to calculate the solar radiation pressure, Earth's infrared radiation, and albedo (Siemes et al., 2023).

2.3.2. THERMAL EMISSION MODELLING

The thermal model proposed in this article is similar to the approach suggested and implemented by Wöske et al. (2019). We modelled the satellites by 12 independent panels and the inner body. The panels heat up uniformly by absorbing incoming radiation $\dot{Q}_{\mathrm{abs},j}$, cool down by emitting radiation $\dot{Q}_{\mathrm{emit},j}$ and exchange heat $\dot{Q}_{\mathrm{cond},j}$ conductively with the satellite body, resulting in the net heat change

$$\dot{Q}_j = (1 - e_j)\,\dot{Q}_{\mathrm{abs},j} - \dot{Q}_{\mathrm{emit},j} - \dot{Q}_{\mathrm{cond},j}, \tag{2.7}$$

where e_j stands for the electric efficiency, and subscript j indicates the panel. The electric efficiency represents the fraction of absorbed energy converted into electricity. Therefore, $e_j > 0$ for the solar arrays while $e_j = 0$ for the other panels not covered by photovoltaic cells. Introducing the efficiency parameter into the thermal model has been done by multiple authors (Duan and Hugentobler (2022), Y. Wang et al. (2023)). However, it was not the case in formerly published GRACE-FO datasets (Siemes et al., 2023).

The radiation Φ that originates from solar and Earth fluxes, as well as albedo, is absorbed in both visible and infrared bandwidths following the equation

$$\dot{Q}_{\mathrm{abs},j} = \Phi c_{\mathrm{a},j} A_j \cos\theta_j, \tag{2.8}$$

where $c_{\mathrm{a},j}$ is the absorption coefficient, A_j is the area of the panel, and θ is the angle between the panel's normal and the vector from the satellite to the radiation source. The heat loss toward space follows the Stefan-Boltzmann law of diffuse irradiation:

$$\dot{Q}_{\mathrm{emit},j} = A_j \varepsilon_j \sigma T_j^4, \tag{2.9}$$

where ε_j is the emissivity, σ is the Stefan-Boltzmann constant and T_j is the absolute temperature of the satellite panels.

The thermal conduction between the satellite walls and the inner body T_{body} is

$$\dot{Q}_{\mathrm{cond},j} = k_j (T_j - T_{\mathrm{body}}), \tag{2.10}$$

where k_j is the thermal conductivity. The total heat exchange for the satellite body is

$$\dot{Q}_{\mathrm{body}} = \dot{Q}_{\mathrm{gen}} + \sum_j \dot{Q}_{\mathrm{cond},j}, \tag{2.11}$$

where $\dot{Q}_{\mathrm{gen}}$ stands for the internal heat generated by, e.g., the batteries and electronics. The $\dot{Q}_{\mathrm{gen}}$ value was selected to assure the realistic operational inner temperature T_{body} of about 25 °C.

In the numerical implementation, panels and body temperatures are updated at each timestep following the equations

$$T_j(t+\Delta t) = T_j(t) + \frac{\dot{Q}_j}{C_j}\Delta t, \tag{2.12}$$

and

$$T_{\text{body}}(t+\Delta t) = T_{\text{body}}(t) + \frac{\dot{Q}_{\text{body}}}{C_{\text{body}}}\Delta t, \tag{2.13}$$

where C_j and C_{body} are the thermal capacity of the panels and the satellite body, respectively.

Finally, the thermal radiation pressure acceleration is derived using the following formula

$$\boldsymbol{a}_{\text{the}} = -\frac{2}{3}\sum_j \frac{\dot{Q}_{\text{emit},j}}{m\,c}\boldsymbol{n}_j, \tag{2.14}$$

where $\boldsymbol{n}_j$ is the outer panel normal of the j surface element.

The following control parameters describe the thermal model: heat capacity of the panels, thermal conductance towards the inner parts, solar cell efficiency, and internal heat generated by the payload and other electronic parts. We optimise the control parameters by minimising the Root Mean Square (RMS) of the difference in the y-component of the accelerations $a_{\text{the,y}}$ as calculated in Eq. 2.14 and $\hat{a}_{\text{the,y}}$ derived directly from the thermistor measurements:

$$RMS = \sqrt{\frac{\sum_{n=1}^{n}(\hat{a}_{\text{the,y}} - a_{\text{the,y}})^2}{n}}, \tag{2.15}$$

where n is the number of data points in 2020. We selected this year because of the satellite's high altitude and low solar activity.

2.3.3. SURFACE COEFFICIENTS FINE-TUNING

As previously explained in Section 2.3.1, the radiation pressure coefficients were derived using the ray-tracing algorithm. We introduce the sum of the contributions of the individual materials m:

$$\boldsymbol{a}_{\text{rp}}(\alpha,\beta) = \frac{P_{\text{ext}}(\alpha,\beta)}{m}\sum_m \left(\boldsymbol{C}_{\text{a,m}}c_{\text{a,m}} + \boldsymbol{C}_{\text{d,m}}c_{\text{d,m}} + \boldsymbol{C}_{\text{s,m}}c_{\text{s,m}}\right). \tag{2.16}$$

The factors $c_{\text{a,m}}$, $c_{\text{d,m}}$, and $c_{\text{s,m}}$ denote coefficients of absorption, diffuse and specular reflections, respectively, while $\boldsymbol{C}_{\text{a,m}}$, $\boldsymbol{C}_{\text{d,m}}$, and $\boldsymbol{C}_{\text{s,m}}$ are radiation pressure coefficient vectors. These vectors originating from the intersection of the i-th ray, with the j-th surface element, and then summing all intersections with surface elements of the same material (sum over index i), are defined as

$$\boldsymbol{C}_{\text{a,m}} = \sum_i A_i \boldsymbol{r}_i \tag{2.17}$$

for absorption,

$$\boldsymbol{C}_{\mathrm{d,m}} = \sum_i A_i (r_i - \frac{2}{3}\boldsymbol{n}_j) \tag{2.18}$$

for diffuse reflection, and

$$\boldsymbol{C}_{\mathrm{s,m}} = \sum_i 2A_i (r_i \cdot \boldsymbol{n}_j) \cdot \boldsymbol{n}_j \tag{2.19}$$

for specular reflection. Calculating the sum of all surface elements with the same material allows us to extract the individual materials' contribution to the total radiation pressure. This equation holds for both infrared and visible light. However, this analysis focuses only on the latter. It is because the magnitude of the Earth's infrared radiation is much smaller than the solar radiation in the along-track and cross-track directions (Vielberg & Kusche, 2020), which are relevant for the density and crosswind observations. In the selected period for GRACE-C, the infrared radiation pressure acceleration was smaller than 0.5 nm s^{-2} in both x and y directions. In comparison, the size of the SRP acceleration was about 12 nm s^{-2} in the along-track and about 28 nm s^{-2} in the cross-track direction, respectively.

To realistically represent GRACE-FO characteristics, a new set of finetuned coefficients c_m, describing surface properties is necessary. In the first step, the density based on the along-track acceleration (Eq. 2.3) was used to derive the acceleration in the y-direction due to aerodynamic side forces,

$$a_{\mathrm{aero},y,der} = \frac{C_{\mathrm{aero},y}}{C_{\mathrm{aero},x}} a_{\mathrm{aero},x}, \tag{2.20}$$

where $C_{\mathrm{aero,y}}$ is the aerodynamic coefficient vector, multiplied by the corresponding cross-section area, and $a_{\mathrm{aero},y,der}$ stands for the y-component of aerodynamic acceleration derived from the along-track signal.

Afterwards, we calculated the difference

$$\Delta a_{\mathrm{aero},y} = a_{\mathrm{aero},y} - a_{\mathrm{aero},y,der}, \tag{2.21}$$

between the derived cross-track acceleration and the observed one. We selected a time period of one year (2020) to optimise the radiation pressure model. This selection is motivated by the high GRACE-FO altitude of approximately 510 km, the very low solar activity during that period, and the fact that all local solar times are covered within one year. Under such conditions, the acceleration due to crosswind is negligible, and $\Delta a_{\mathrm{aero},y}$ should thus equal zero. Since the aerodynamic acceleration depends on the radiation pressure acceleration $\boldsymbol{a}_{\mathrm{rp}}$ and thermal acceleration $\boldsymbol{a}_{the}$ (cf. Eq. 2.1 and Eq. 2.2), we used it directly to determine new coefficients. We note that $\boldsymbol{a}_{the}$ was calculated from the thermistor measurements as described in Section 2.3.2.

In the next step, a highpass filter was applied to $\Delta a_{\mathrm{aero},y}$ to eliminate the influence of the accelerometer data calibration, which affects daily and longer periods (Siemes et al., 2023):

$$\Delta a_{\mathrm{aero},y,filt} = \mathrm{filt}\,(\Delta a_{\mathrm{aero},y}). \tag{2.22}$$

In contrast to the accelerometer data calibration, radiation pressure modelling errors also affect the sub-daily variations in $\Delta a_{\text{aero},y}$, e.g., step-like changes at the eclipse entry and exit locations. Applying a highpass filter allows us to focus on these errors and, therefore, optimise the reflection coefficients without any impact from the accelerometer data calibration.

The radiation pressure acceleration can be defined as a function of the absorption and reflection coefficients per material:

$$f(c_{a,m}, c_{d,m}, c_{s,m}) = \| \Delta a_{\text{aero},y,filt} \|. \tag{2.23}$$

Finally, we use the Sequential Least SQuares Programming (SLSQP) technique originally implemented by Kraft (1988) to minimise $f(c_{a,m}, c_{d,m}, c_{s,m})$. The SLSQP algorithm allows minimising a linear function of several variables subject to bounds and constraints, here defined as:

$$c_{\text{a,m}} \in [0,1], \;\; c_{\text{d,m}} \in [0,1], \;\; c_{\text{s,m}} \in [0,1], \quad c_{\text{a,m}} + c_{\text{d,m}} + c_{\text{s,m}} = 1. \tag{2.24}$$

The optimum solution was computed after 15 iterations. The fine-tuned surface coefficients are provided in Table 2.2 (Section 2.4.2).

Apart from optimising the surface properties, $\Delta a_{\text{aero},y}$ as defined in Eq. 2.21 serves to calibrate the cross-track acceleration. When the calibration is only based on precise orbit determination (POD), the cross-track calibration accuracy suffers from, e.g., dynamic force model errors, which renders the crosswind observations unusable. To resolve this, we first optimise the radiation pressure modelling to mitigate errors from this source as much as possible. Then, we recalculate $\Delta a_{\text{aero},y}$ and apply a lowpass filter that removes sub-daily variations to extract the accelerometer data calibration and remaining radiation pressure modelling errors (Siemes et al., 2023). The lowpass filtered $\Delta a_{\text{aero},y}$ is directly applied as a correction to the cross-track accelerations.

2.4. RESULTS AND DISCUSSION

2.4.1. THERMAL EMISSION MODELLING

The design of solar arrays of GRACE and GRACE-FO differs. While the GRACE satellites were equipped with silicon cells, its successors utilize modern triple-junction gallium arsenide (GaAs) cells with an efficiency of 28% (Kornfeld et al., 2019). Since the proposed thermal model is based on the panel model, we must distinguish between the area covered by photovoltaic cells and the panel area, partly covered by multi-layer insulation (MLI) foil, star trackers, and other elements. Based on the technical drawings (Fig. 2.2) the exact number of solar cells n was estimated for solar arrays $n_{SA} = 656$ and the zenith panel $n_{zenith} = 479$. The area of the individual cell is known to be A_{cell}=31.36 cm. Using this information, the packing factor p can be calculated as a ratio between the effective area covered by the solar cells, and the total panel area

$$p = \frac{A_{cell} * n}{A_{total}}. \tag{2.25}$$

Following this equation the packing factor was estimated to be 0.66 for the side panels and 0.69 for the zenith panel, resulting in the panel efficiency of 18% and 19%, respectively.

The design difference between GRACE and GRACE-FO solar arrays also affects the visible and infrared surface coefficients as they control how much energy is absorbed or reemitted. Table 2.2 provides optimised coefficients for visible light. The emissivity was specified according to the Swarm technical note on thermo-optical properties (Siemes, 2019), noting that the Swarm solar array is the same as on GRACE-FO. In the proposed modelling approach the emissivity, as well as efficiency, fulfil the same function of controlling how much radiation is reemitted. This means that both parameters have almost the same effect on the cross-track acceleration, and therefore cannot disentangle. For this reason, we only modify the efficiency.

We used the in-situ thermistor measurements to select the remaining thermal model control parameters, the heat capacity and conductivity. As described in Section 2.2.2, only external thermistors located on the solar arrays on the side panels and the zenith panel were suitable for such analysis. Since the thermal emission contributes mainly to the cross-track acceleration, the thermistor's locations perfectly align with our modelling requirements.

The first step in optimising the heat capacity and conductivity was to convert thermistors measurements and modelled temperatures into the accelerations following Eq. 2.14. Since each solar array on the side panels has two temperature sensors, we determined the acceleration difference between both sensor pairs. Fig. 2.6 shows that the differences do not surpass $0.6\,\mathrm{nm\,s^{-2}}$, which was used as a reference for the maximum reachable modelling accuracy, noting that our model assumes a uniform temperature per panel.

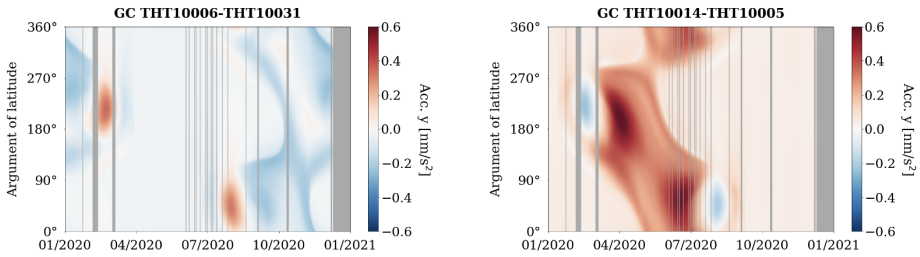

Figure 2.6: Comparison between the measurements of thermistors located on the same solar array, translated into acceleration.

In the second step, we compared the accelerations based on the measured temperatures, $\hat{a}_{the,y}$, and the modelled temperatures, $a_{the,y}$, for a range of capacity and conductivity values using the RMS defined in Eq. 2.15. Fig. 2.7 and Fig. 2.8 summarise the results. For the solar arrays, the best fit (RMS = $0.148\,\mathrm{nm\,s^{-2}}$) was obtained for heat capacity $C = 8200.0\,\mathrm{J\,K^{-1}}$ and conductivity $k = 0.4\,\mathrm{W\,K^{-1}}$. Such parameter selection assures that the thermal model accuracy is within the earlier defined range of $0.6\,\mathrm{nm\,s^{-2}}$ (Fig. 2.6).

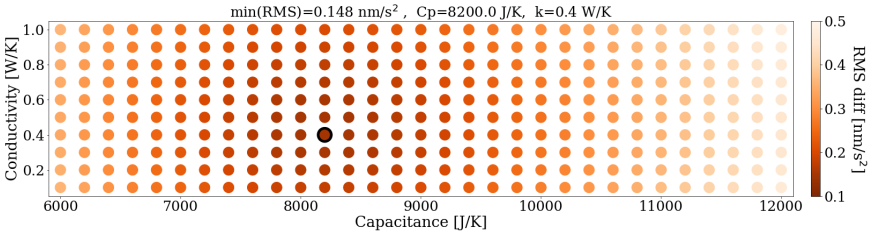

Figure 2.7: Root Mean Square (RMS) acceleration difference between the thermal model and the THT10005/THT10031 thermistors. The best fit was obtained for capacity C=8200.0 J K^{-1} and conductivity k=0.4 W K^{-1} The best RMS fit is indicated with the dark circle.

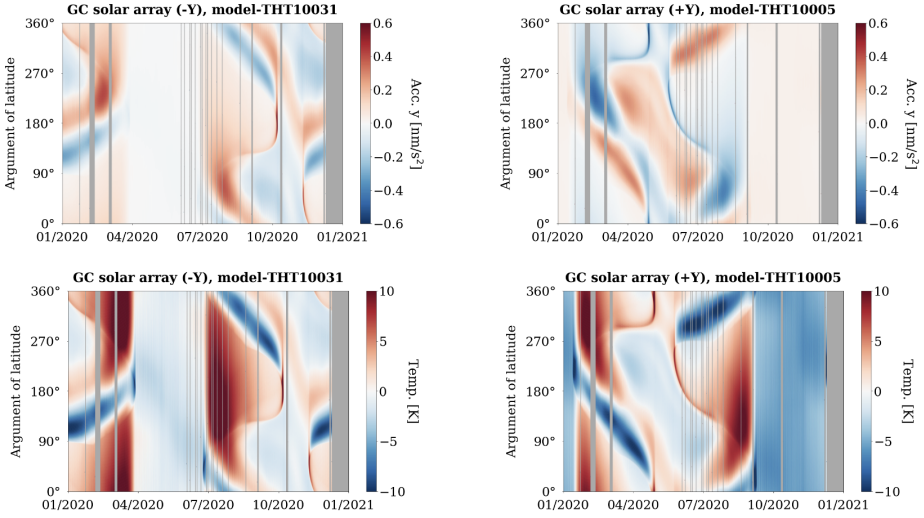

Figure 2.8: Differences between the accelerations (top) and the temperatures (bottom), derived from the thermal model and measured by thermistors.

We performed a similar analysis for the zenith panel, for which external temperature sensors are also available. The best fit was found for $C = 5800.0\,\mathrm{J\,K^{-1}}$ and $k = 0.7\,\mathrm{W\,K^{-1}}$. The difference between solar arrays and zenith thermal parameters is likely caused by different packing factors of the solar cells.

This analysis focused on optimising the thermal model for the panels for which the thermistor measurements were available. The remaining values of heat capacities and conductivities were defined according to the GRACE-FO thermal model developed by Siemes et al. (2023). Table 2.1 summarises the updated parameters and previously used values.

Table 2.1: GRACE-FO thermal radiation panel model. The internal heat generation was set to 55 W, and the satellite body heat capacity to 1×10^5 JK^{-1}.

Panel	A_j (m^2)	$n_{x,j}$ (-)	$n_{y,j}$ (-)	$n_{z,j}$ (-)	Siemes et al. (2023) C_j (JK^{-1})	Siemes et al. (2023) k_j (WK^{-1})	New thermal model C_j (JK^{-1})	New thermal model k_j (WK^{-1})	New thermal model e_j (-)
Front	0.9552	1.0	0.0	0.0	4000.0	0.1	4000.0	0.1	-
Rear	0.9552	-1.0	0.0	0.0	4000.0	0.1	4000.0	0.1	-
Starboard (outer)	3.1555	0.0	0.7660	-0.6428	18000.0	0.1	8200.0	0.4	0.18
Starboard (inner)	0.2283	0.0	-0.7660	0.6428	800.0	0.1	800.0	0.1	-
Port (outer)	3.1555	0.0	-0.7660	-0.6428	18000.0	0.1	8200.0	0.4	0.18
Port (inner)	0.2283	0.0	0.7660	0.6428	800.0	0.1	800.0	0.1	-
Nadir	6.0711	0.0	0.0	1.0	10000.0	0.5	10000.0	0.5	-
Zenith	2.1674	0.0	0.0	-1.0	12000.0	0.1	5800.0	0.7	0.19
Boom	0.0462	-	-	-	400.0	0.01	400.0	0.01	-

* Planar projection area of the cylindrical Boom, along X-Y plane.

2.4.2. SURFACE COEFFICIENTS FINE-TUNING

This section reports the results of the surface coefficient optimization using the method described in Section 2.3.3 and summarized in Table 2.2. The first column describes the material, whereas the next column provides initial values of the optical coefficients from the GRACE-FO Level-1 Data Product User Handbook (Ying et al., 2019) and recently re-defined values from Siemes et al. (2023). The last columns consist of the coefficients optimized within this study. The coefficients for infrared radiation are defined in the handbook and were not modified. These coefficients have an insignificant effect on the y-acceleration and could not be finetuned with the method presented in this paper.

Table 2.2: Comparison between GRACE-FO surface coefficients for visible light: defined in Level-1 Data Product User Handbook (Ying et al., 2019) (1), provided by Siemes et al. (2023) (2), and fine-tuned within this study (3). Surface coefficients for infrared radiation are defined in Level-1 Data Product User Handbook.

(1) Material	(1) Level-1 Handbook			(2) Siemes et al. (2023)			(3) Fine-tuned coefficients		
	c_a	c_d	c_s	c_a	c_d	c_s	c_a	c_d	c_s
SiOx/Kapton (Front/Rear)	0.34	0.26	0.40	0.34	0.26	0.40	0.14	0.15	0.71
SiOx/Kapton (Apron)	0.34	0.26	0.40	0.34	0.26	0.40	0.05	0.79	0.16
Si Glass (Solar Arrays)	0.65	0.30	0.05	0.90	0.07	0.03	0.90	0.10	0.00
Si Glass (Zenith)	0.65	0.30	0.05	0.90	0.07	0.03	0.88	0.00	0.12
Teflon (Nadir)	0.12	0.20	0.68	0.12	0.20	0.68	0.00	0.05	0.95

In addition to the SLSQP fitting of the coefficients, we inspected the satellite photos visually to cross-check updated thermo-optical surface coefficients. One of the fundamental design differences between GRACE-FO (Fig. 2.1) and its predecessor was replacing the silicon solar cells (Si Glass) with state-of-the-art triple-junction gallium arsenide (GaAs) cells, previously certified for the Swarm mission (Kornfeld et al., 2019). These solar arrays absorb more light and, thus, have a higher efficiency. This design similarity between Swarm and GRACE-FO justifies the selection of optical absorption (c_a=0.90), which coincides with the value provided in Swarm technical note on thermo-optical

properties (Siemes, 2019).

The second dissimilarity visible in the prelaunch photos (Fig. 2.1) is the difference in the solar arrays' packing factor of the side panels and the zenith panel. The zenith panel is more densely populated by the solar cells (black) compared to the two side panels, which reveal more of the background MLI foil (red). Since the ray-tracing algorithm treats the MLI and solar cells (depicted as red and black surface elements) uniformly, the packing factor affects the overall absorptivity of this material (c_s=0.90 → c_s=0.88).

Another distinctive element between GRACE and GRACE-FO is the nadir panel (red circles in Figs. 2.9a and 2.9b). The GRACE nadir panel has a much more creased surface than the reflective GRACE-FO material. This difference justifies finetuning the specular reflection coefficient to the higher value (c_s=0.68 → c_s=0.95).

Ultimately, we finetuned the satellite's apron surface coefficients. This small geometry element proved to have a significant impact on the radiation pressure acceleration. The Handbook defines the surface properties of the apron and the rear/front panels as identical. However, the photos reveal that the front/rear panels have a reflective surface, whereas the apron is creased and, thus, reflects light more diffusely than a flat surface of the same material (Fig. 2.9c). Such difference validates the increase in the diffuse reflection component (c_d=0.26 → c_d=0.79).

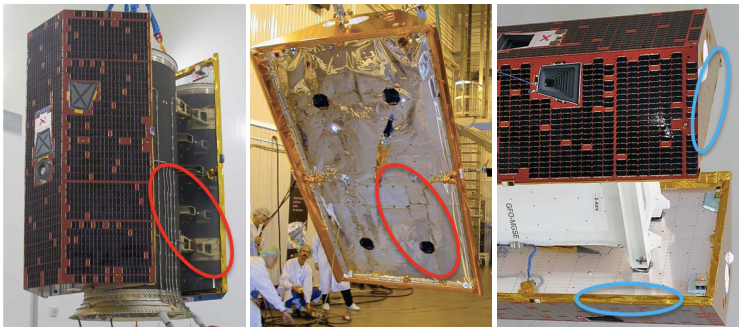

(a) GRACE-FO[4] (b) GRACE[5] (c) GRACE-FO[6]

Figure 2.9: Prelaunch photos of GRACE and GRACE-FO satellites. Red circles (a) and (b) show the differences in the nadir panel design between two satellites. Blue circles (c) indicate the differences in the material of the apron and the rear panel.

2.4.3. EFFECT OF RADIATION PRESSURE MODEL ACCURACY ON THE CROSS-TRACK ACCELERATION

As discussed before, the cross-track calibration purely based on POD suffers from low accuracy, affecting the quality of crosswind data. The exact steps undertaken to resolve

[4] URL https://www.airbus.com/en/newsroom/press-releases/2017-05-grace-fo-satellites-get-an-earful, accessed on 03/10/2023.

[5] Gath (2016)

[6] https://www.airbus.com/en/newsroom/press-releases/2017-05-grace-fo-satellites-get-an-earful, accessed on 03/10/2023.

this issue were described in Section 2.3. Here, we used the $\Delta a_{aero,y}$ parameter derived in Eq. 2.21 to assess the performance of various radiation pressure and thermal emission modelling approaches. The calibration parameters were estimated based on the final model (Case (e), Table 2.3) and applied consistently to all previous cases. This approach enabled disentangling the calibration parameters' accuracy and focus on the sole impact of the radiation pressure modelling.

Table 2.3 summarises models used in this study, together with their input parameters: thermal emission model, geometry model and the thermo-optical surface coefficients used. The last column states the RMS estimate as the model quality indicator.

Table 2.3: Summary of GRACE-FO radiation pressure modelling approaches implemented in this study.

Case	Thermal model	Geometry model	Surface properties	RMS
	-	-	-	($\mathrm{nm\,s^{-2}}$)
(a)	-	Panel	Level-1 Handbook	4.22
(b)	Instantaneous reradiation	Panel	Level-1 Handbook	3.04
(c)	Thermal inertia	Panel	Level-1 Handbook	1.70
(d)	Thermal inertia	Ray-tracing	Siemes et al. (2023)	0.88
(e)	Thermal inertia	Ray-tracing	Fine-tuned coefficients	0.55

The most straightforward approach to radiation pressure modelling is presented in Fig. 2.10a. It utilizes the simplest geometry consisting of 6 panels and does not account for thermal emission. The thermo-optical surface properties used for the radiation pressure modelling follow the guidelines provided in the Level-1 Handbook. In this modelling variant, the acceleration difference $\Delta a_{aero,y}$ exceeds the RMS of 4.22 $\mathrm{nm\,s^{-2}}$. The largest offset occurs when the satellite solar arrays on the sides of the satellite (red area in Fig. 2.4) are oriented perpendicular to the Sun. These locations are indicated by yellow dashed rectangles (Fig. 2.10a). At this stage, the cross-track acceleration errors originate mainly from ignoring the thermal emission of the solar arrays, as demonstrated in the next paragraphs.

The second model, illustrated in Fig. 2.10b, assumes instantaneous heat reradiation for all panels (Montenbruck et al., 2015), i.e. the absorbed radiation is instantly re-emitted in accordance with Lambert's cosine law. The main difference in comparison to Case (a) can be noted in the radiation pressure errors originating from the solar arrays. It occurs when the solar arrays are oriented approximately perpendicular to the Sun, which takes place between the arguments of latitude 90° and 270°, during April 2020 for the (+Y) solar array and November 2020 for (-Y) solar array. Similar to the previous figure, these locations are indicated by yellow dashed rectangles. The second effect can be spotted near the eclipse regions, which can be identified based on the shadow function shown in Fig. 2.10f, indicated as green crosses. This effect occurs when the satellite enters the eclipse, and the nadir panel receives direct radiation, which is then re-radiated. Since this scenario better reflects reality, the radiation pressure errors decrease compared to Case (a). Using the instantaneous heat re-radiation model, the overall radiation pressure error $\Delta a_{\mathrm{aero},y}$ reduces to RMS 3.04 $\mathrm{nm\,s^{-2}}$.

Figure 2.10c was produced using a thermal model that accounts for the thermal inertia of the panels as described in Section 2.3.2. The optimized thermal control param-

eters are provided in Table 2.1. In this variant, the panel geometry was used for both radiation pressure and thermal emission modelling. After accounting for the thermal inertia the $\Delta a_{\text{aero},y}$ decreases significantly, to RMS 1.70 nm s^{-2}. In the next step, we complemented the advanced thermal modelling with ray-tracing utilizing the high-fidelity geometry and the thermo-optical surface coefficients proposed by Siemes et al. (2023), provided in Table 2.2. The model's output is depicted in Fig. 2.10d. Including additional geometry elements creates a more uniform error pattern. An interesting effect, exhibiting as $\Delta a_{\text{aero},y}$ reduction around the eclipse transitions, was identified as a shadowing effect from the satellite's apron. In this step, the cross-track acceleration RMS is reduced to 0.88 nm s^{-2}.

Last but not least, Fig. 2.10e shows the thermal emission modelling improvements combined with the ray-tracing method, detailed satellite geometry, and fine-tuned thermo-optical surface coefficients (Table 2.2). Introducing these improvements altogether results in the significant reduction of the $\Delta a_{\text{aero},y}$ errors below 0.55 nm s^{-2}.

The remaining radiation pressure residuals could be caused by errors in the thermistors' measurements, as well as the modelling limitations, e.g., the assumption of the uniform temperature of the panels. To resolve this issue, we could introduce a finite element thermal model. However, such a modelling approach is computationally demanding and unlikely to give significant improvement due to other error sources, which are out of the scope of this work. These error sources include the assumption about negligible cross-wind during low solar activity while fine-tuning the surface coefficients, aerodynamic coefficient modelling errors originating from the gas-surface interaction modelling uncertainties, and accelerometer data calibration errors. To model the penumbra transitions, this paper utilizes the Solar radiation pressure with Oblateness and Lower Atmospheric Absorption, Refraction, and Scattering Curve Fit (SOLAARS-CF) (Robertson et al., 2015). However, using this approach results in noticeable artefacts remaining around the eclipse entrances/exits. Therefore, these times were excluded while calculating the RMS.

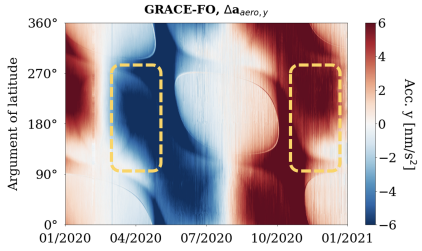

(a) Not accounting for the thermal emission acceleration.

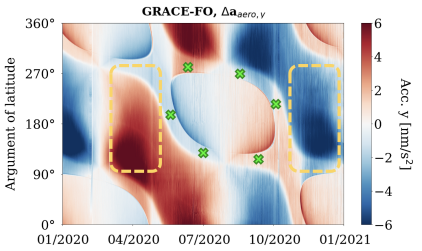

(b) Instantaneous thermal reradiation.

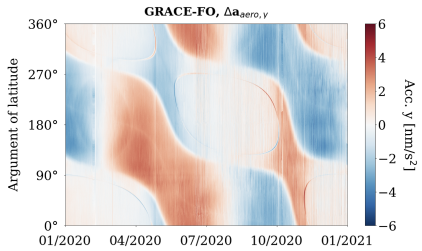

(c) Thermal inertia and panel method.

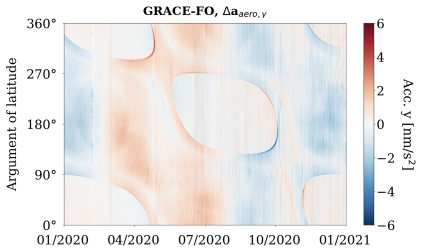

(d) Thermal inertia and ray-tracing method.

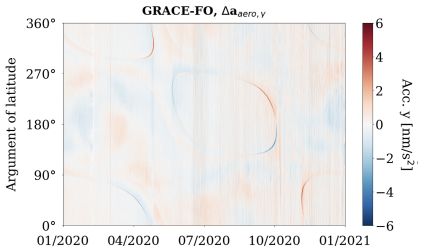

(e) Thermal inertia and fine-tuned thermo-optical surface properties.

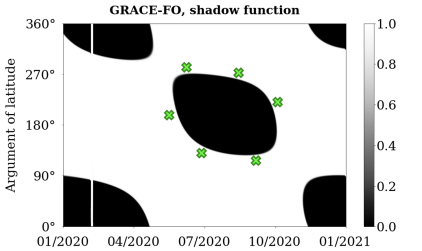

(f) Shadow function.

Figure 2.10: Difference between observed and derived cross-track acceleration $\Delta a_{\text{aero},y}$ defined in Eq. 2.20 for cases (a)–(e) (cf. Table 2.3) and the shadow function. White and black areas indicate when the satellite is in the sunlight or shadow. The yellow dashed-line rectangles indicate when the satellite solar arrays were oriented perpendicular to the Sun. The green crosses mark locations when the satellite is close to the penumbra regions.

2.4.4. DENSITY AND CROSSWIND OBSERVATIONS

The new GRACE-FO density and crosswind datasets, labelled V2b, are available from the FTP server ftp://thermosphere.tudelft.nl[7]. Compared to the previous version V2 in Siemes et al. (2023), this new version contains two major improvements. Firstly, it is based on the fine-tuned surface coefficients for the radiation pressure modelling. Secondly, it introduces the electrical efficiency of the solar arrays into the thermal model and optimises its parameters based on real temperature data.

[7] Since 2026 HTTPS Server https://thermosphere.tudelft.nl/data/

2

CROSSWIND

To analyse the impact of the radiation pressure modelling on the crosswind data, we selected a time period of increasing solar activity from 2022 until mid-2023. Figure 2.11 shows the 3-hourly geomagnetic activity index ap and 10.7cm solar radio flux ($F_{10.7}$). Figure 2.12 compares the log RMS ratio of the radiation pressure acceleration to the aerodynamic acceleration for GRACE-C with a sliding window of one week. For the selected period, the magnitude of the aerodynamic acceleration surpasses the magnitude of radiation pressure in the along-track direction. For the cross-track direction, the RMS ratio reflects the trend of the $F_{10.7}$ curve (Figure 2.11). At the beginning of 2022, the magnitude of the radiation pressure acceleration is 10 times larger in comparison to the aerodynamic acceleration. Figure 12 shows that this difference gradually decreases with increasing solar activity in 2023. The low periodic RMS ratio values for cross-track acceleration occur when the Sun is aligned with the orbital plane, resulting in accelerations from the right and left solar array cancelling out.

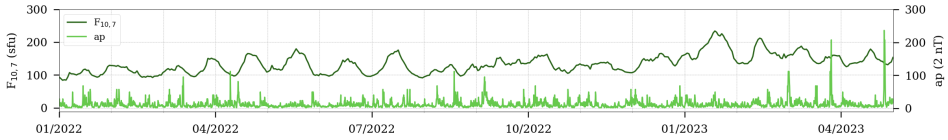

Figure 2.11: 3-hour ap (source: GFZ German Research Center for Geosciences) and 10.7cm solar radio flux ($F_{10.7}$). 1 sfu = $10^{-22} \cdot \mathrm{W} \cdot \mathrm{m}^{-2} \cdot \mathrm{Hz}^{-1}$.

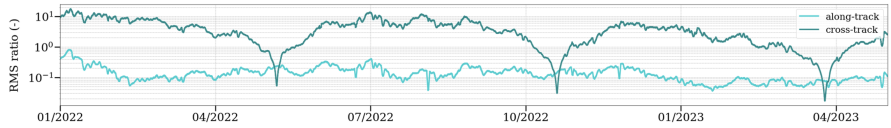

Figure 2.12: Size of the radiation pressure acceleration relative to the aerodynamic acceleration for GRACE-C, where the size is measured by the RMS of the acceleration within a sliding one-week window.

Figure 2.13 compares versions V2 and V2b of the observed GRACE-C crosswind. The argument of latitude used in the figures in this section is described in Section 2.2.2. Qualitatively, both versions have several similarities. The wind speeds peak near the poles (close to arguments of latitude 90° and 270°), which is associated with the auroral oval (Lühr et al., 2007), and are generally less than 150 $\mathrm{m\,s^{-1}}$ in the low- and mid-latitudes. Around the north pole (90°±20°), 4% of wind speed exceeds 500 $\mathrm{m\,s^{-1}}$, whereas 9% is larger than 400 $\mathrm{m\,s^{-1}}$. Around the south pole (270°±20°) the wind speed is slightly lower, with only 2% exceeding 500 $\mathrm{m\,s^{-1}}$, and 5% being larger than 400 $\mathrm{m\,s^{-1}}$. Magnetospheric convection and particle precipitation contribute to energy and momentum transfer between ions, drifting rapidly in electric and magnetic fields, and neutrals, which strongly influence the high-latitude thermosphere, including neutral winds (e.g., Barreto-Schuler et al., 2021; T. L. Killeen & Roble, 1984; Richmond et al., 2003).

The sharp curve features present in both V2 and V2b in Figure 2.13 are an artefact

due to eclipse transitions caused by inaccurate modelling of the Earth's shadow. The high wind speeds around January and August/September 2022 visible in both versions in Figure 2.13 also correspond to periods of low signal-to-noise in the measured along track acceleration. Under such conditions, meaningful wind retrieval is limited. This results in spurious features that cannot be mitigated by improvements in radiation pressure modelling alone. In order to distinguish the useful wind data from the spurious features, we have introduced flagging in the published dataset.

The two versions show large differences in 2022, when the ratio of the radiation pressure to aerodynamic acceleration is still significant (see Fig. 2.12). This demonstrates that the radiation pressure models used to produce V2b are superior to V2. In 2023, as solar activity and hence density increase, the difference between the two versions gradually converges. However, the improvements are still visible in periods such as February/March 2023 during the entry and exit of the eclipse, when the wind speed decreases at mid-latitudes.

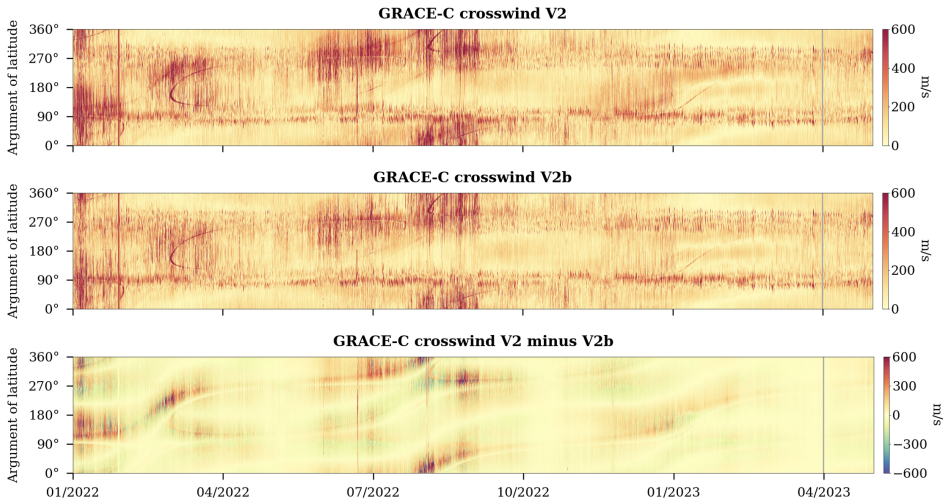

Figure 2.13: GRACE-C crosswind speed version V2 (top, cf. Siemes et al. (2023)), version V2b (middle, this work), and the difference between the two versions (bottom). The values on the x-axis are common for all plots.

In Figure 2.14, we compare the new V2b crosswind data with the physics-based TIE-GCM and the empirical HWM14 models. The crosswind data are given in the same reference frame as the models, and the zonal (east-west), meridional (north-south) and vertical unit vector components are provided in the dataset to accurately project the model winds. The contributions from the vertical wind component are much weaker than the horizontal components and are therefore ignored in this study, similar to Lühr et al. (2011) using CHAMP observations. The model wind vector projected onto the direction of the observed crosswind is obtained as follows:

$$\mathbf{M}_{cw,i} = \mathbf{M}_{zonal,i} \cdot \mathbf{u}_{zonal,i} + \mathbf{M}_{merid,i} \cdot \mathbf{u}_{merid,i}, \tag{2.26}$$

where $\mathbf{M}_{cw,i}$ is the projected model crosswind at time epoch i, and $\mathbf{M}_{zonal}$ and $\mathbf{M}_{merid}$ are the model zonal and meridional wind vectors, respectively. $\mathbf{u}_{zonal}$ and $\mathbf{u}_{merid}$ are the corresponding unit vector components.

Figure 2.14 shows that both models capture most of the salient features of the observed crosswind, especially at low and mid latitudes. The time period shown in the figure corresponds to relatively high solar activity, which improves the quality of the retrieved wind signal. Compared to the TIE-GCM, the HWM14 shows better agreement at high latitudes and well reflects some of the high wind speed around 90° and 270° occurring during the significant geomagnetic storms in late February, March, and April 2023 (see Fig. 2.11). In general, the data-model agreement is better in 2023 than in 2022. While the crosswind speeds are greater than the model estimates, this agreement has improved in 2023 to the extent that the mean model wind speed is about half that of the observed crosswind. Further investigation is needed to determine the extent to which the TIE-GCM underestimates the winds, particularly at high latitudes. Neutral winds at high latitudes are strongly influenced by the direction and strength of the interplanetary magnetic field (IMF) and ion collisions (Richmond et al., 2003). The TIE-GCM runs in this study do not use observed IMF conditions and use, among other parameterisations, an empirical ion convection model based on the 3-hr Kp index, which may have some limitations in accurately modelling ion drag and winds on the observed timescale.

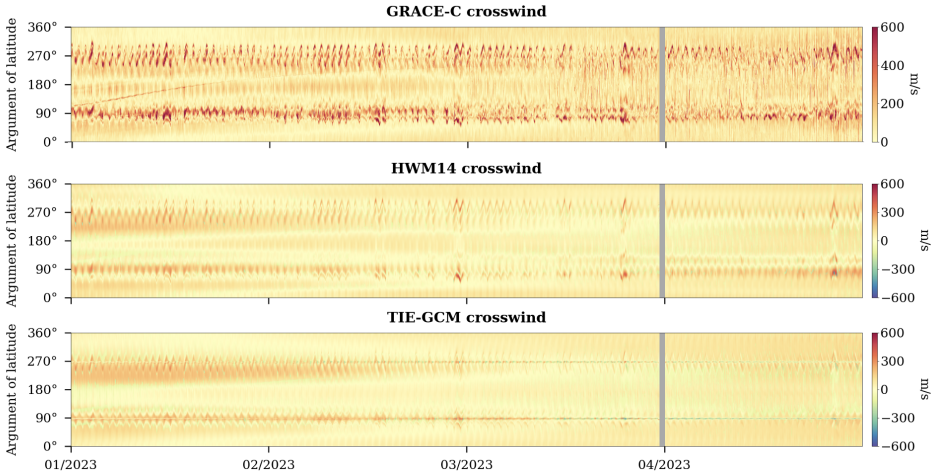

Figure 2.14: Crosswind speed observed by the GRACE-C satellite (top), wind speed from the HWM14 model (middle) and TIE-GCM (bottom). The negative values in the model winds indicate that the wind direction is opposite to the observed wind. The values on the x-axis are common for all plots.

Figure 2.15 shows some general statistics of the data-model comparison from January 2022 to April 2023. The two top panels show the daily mean and standard deviation, respectively. Two bottom panels show the Pearson correlation coefficient, which describes the linear correlation between the models and the observations. Since both TIE-GCM and HWM14 underestimate the high-latitude wind speeds (Fig. 2.14) the Pearson coefficient was calculated for two subsets: including all data, and considering only

low- and mid-latitude crosswinds, by excluding data between arguments of latitude 60°–120° and 240°–300°. The penumbra regions were discarded while calculating the statistical data.

The figure shows a remarkable improvement in the GRACE-C retrieved winds after September 2022, when the daily mean stabilises, the standard deviation is consistently low, and the correlation increases. We observe an exceptionally good correlation after January 2023 reaching 0.6 for all data and 0.8 if only low- and mid-latitude wind speeds are considered. The figure also shows that the GRACE-C crosswinds are quite stable from April to June 2022. There are a few periods in 2022 with large wind speeds and high standard deviations (e.g. January, March and August). As explained earlier, this is due to the spurious features in the crosswind data resulting from an insufficient signal-to-noise ratio in the acceleration data (see Fig. 2.13). Finally, the figure also highlights the importance of a comprehensive further analysis of the winds to identify the reasons for different model responses to observed geophysical conditions, including the periods of anticorrelated winds in October 2022 and late March 2023.

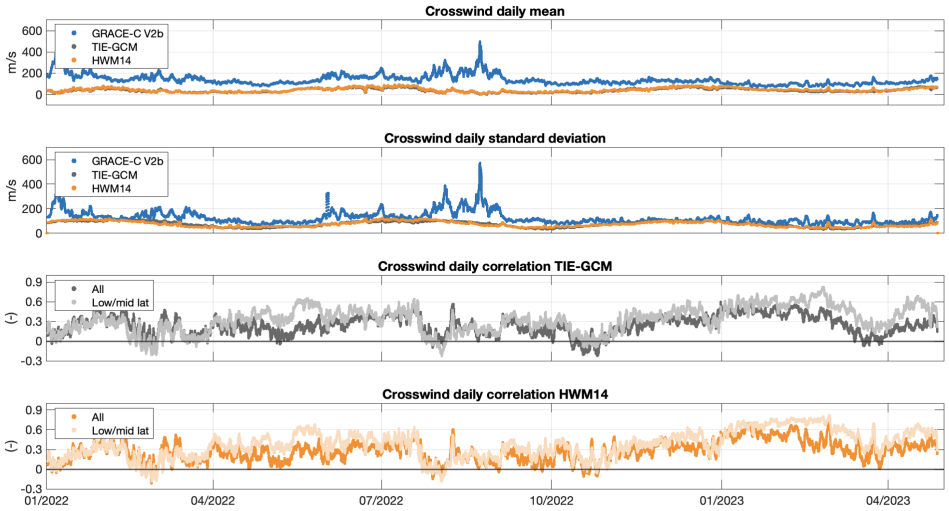

Figure 2.15: Statistical comparison of the crosswind speed observed by the GRACE-C and model estimates from HWM14 and TIE-GCM. Two top panels show the daily mean and the daily standard deviation. Two bottom panels show the Pearson's correlation coefficient for TIE-GCM and HWM14, respectively, for two types of subsets: all data and low- to mid-latitudes. The values on the x-axis are common for all plots.

DENSITY

The newly estimated neutral mass density (V2b) was compared with the previously published data (V2) and two thermosphere models: NRLMSIS 2.0 and DTM2020. The mean density ratio (Sutton, 2018) was used for comparison

$$\mu(\rho_1, \rho_2) = \exp\left(\frac{1}{N}\sum_{n=1}^{N} \ln\frac{\rho_{1,n}}{\rho_{2,n}}\right), \tag{2.27}$$

where ρ_1/ρ_2 is the ratio between the observed and modelled density.

Fig. 2.16a shows the yearly mean of the observation-model density ratio. The solid lines represent the comparison between atmospheric models and version V2 (Siemes et al., 2023), whereas the dashed lines introduce version V2b, produced using new radiation pressure and thermal emission models. It can be seen that the ratio between the observations and DTM2020 is always larger than unity. This means that both previous and new observations consistently show a 5–10% higher density than the DTM2020 model. The only exception is 2021, where the annual mean increases to 25%. The observation-model ratio for NRLMSIS 2.0 is about 0.65 during the solar minimum (2018–2020). This indicates the model's tendency to overestimate the density, which was already pointed out for Swarm data (van den IJssel et al., 2020). As solar activity increases from 2021 onward, the mean density ratio gets closer to one, indicating better agreement between observations and model during medium–high solar activity.

Comparison within versions does not show significant scale differences. This is expected since both V2 and V2b datasets share the same aerodynamic model and differ only in the radiation pressure and thermal emission, which average to zero in the yearly mean.

To compare the variability across the density data, the standard deviation of the density ratio was used:

$$\sigma(\rho_1, \rho_2) = \exp\left(\sqrt{\frac{1}{N-1}\sum_{n=1}^{N}\left(\ln\frac{\rho_{1,n}}{\rho_{2,n}} - \ln\mu(\rho_1, \rho_2)\right)^2}\right) \tag{2.28}$$

Fig. 2.16b shows the annual standard deviation. The annual standard deviations have continuously decreased since the beginning of the mission in 2018. This is likely caused by radiation pressure modelling errors playing a smaller role when the solar activity, and hence density, increases towards 2023. The annual standard deviation for DTM2020 is always lower compared to NRLMSIS 2.0, which indicates a better model agreement with observations' variability. Nevertheless, considerable values can still be seen for DTM2020, starting from 32% in 2018 to 22% in 2023. For NRLMSIS 2.0, the standard deviations range from 45% in 2018 to 28% in 2023. These larger values could be explained by the fact that the NRLMSIS 2.0 model is independent of the density observations produced after 2000.

Similarly to the annual mean, the standard deviations of V2 and V2b follow almost the same pattern. However, a small difference of about 1–2% can be spotted for the DTM2020 model. One may conclude that the V2b density observations are slightly worse. Yet, it is important to note that DTM2020 is based on the data where not all advances in radiation pressure modelling have been implemented. NRLMSIS 2.0 also indicates that the V2b data agrees less with the model, though the standard deviations are much larger than those of DTM2020, obscuring the subtle differences between V2 and V2b. Given the clear improvements in the crosswind observations, further investigation is needed to confirm if the changes in the variability of the V2b density data represent a worsening or improvement.

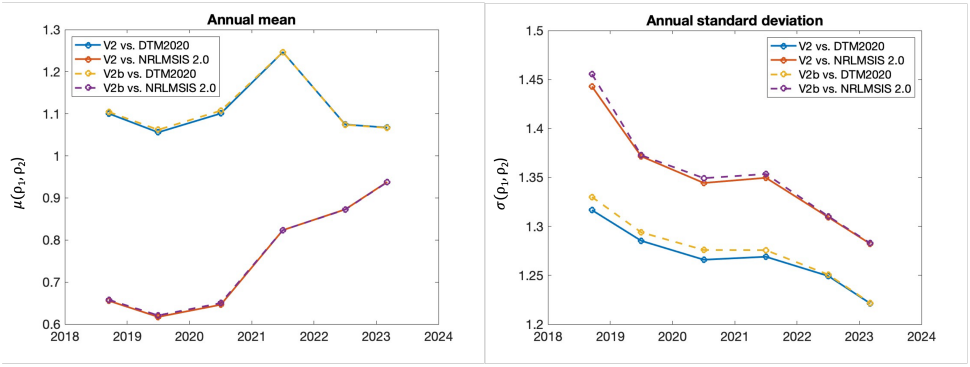

(a) GRACE-FO observation-model mean.

(b) GRACE-FO Observation-model standard deviation.

Figure 2.16: Comparison of GRACE-FO density observations to DTM2020 and NRLMSIS 2.0. Observations of version V2 are based on Siemes et al. (2023) and V2b was developed within this study.

2.5. CONCLUSIONS AND OUTLOOK

The motivation for this study was twofold: to determine the impact of radiation pressure and thermal emission modelling during periods of low solar activity and to derive updated density and crosswind datasets. The first was achieved by fine-tuning the reflection coefficients to characterise satellite surface properties better. A thermal emission model based on heat transfer was introduced together with the solar panel electric efficiency parameter. Achievements in radiation pressure modelling allowed for better cross-track calibration and improved crosswind datasets.

The accessibility of the thermistor measurements from the top and side panels was key to the success of this research. By knowing the external surface temperature, it was possible to disentangle the thermal emission from the other sources of radiation pressure and model it separately. To further improve the radiation pressure modelling accuracy, reliable data from thermistors in suitable locations on accelerometer-carrying satellites would be desired. Equipping future missions with thermistors that are distributed externally in multiple places would allow for an even more advanced modelling approach, for example, a finite-element thermal analysis. On the contrary, the inaccessibility of meaningful thermistor readings poses limitations on thermal emission modelling for past missions. This is the case for GRACE, where multiple temperature sensors were placed below the insulation foil, making a similar analysis as the one performed in this study meaningless since the thermistor data do not represent the topside temperature of the panel.

The thermal model accounting for thermal inertia significantly reduced the error compared to the instantaneous heat re-radiation. However, it is also more computationally demanding, as the calculations cannot be performed up-front but must be done along the orbit instead. Therefore, the choice of the appropriate thermal model depends on the required accuracy.

Taking into account the design similarities between GRACE-FO and Swarm solar arrays, it would be recommended to update the GRACE-FO documentation with the solar arrays' thermo-optical surface properties as specified for the Swarm mission. The sur-

face coefficients defined for other materials should also be revisited. It was shown for the GRACE-FO apron, that in the case of foils, the reflection coefficients may vary depending on the wrinkling, and thus should be specified per separate foil sheet, and not globally for the whole material.

The improvements in the radiation pressure modelling did not have a significant impact on the density observations. In the case of the crosswind, a low aerodynamic signal along the track prevented the derivation of usable observations for some periods and manifested itself as spurious features in the crosswind data. To distinguish these spurious features from real geophysical signals, and to better attribute observation-model discrepancies, it would be be beneficial to define reliable error bounds. Such error quantification should include errors in radiation pressure modelling, aerodynamic coefficient estimation, calibration errors and accelerometer measurement noise, as well as errors in external models providing thermosphere characteristics, such as uncertainty in the radiation fluxes and thermosphere composition. This work is currently in progress.

ACKNOWLEDGMENTS

The authors would like to thank Christopher Mccullough from NASA Jet Propulsion Laboratory for granting access to GRACE-FO thermistors data. An additional acknowledgement goes to Airbus Defence and Space for providing the CAD model of the GRACE-FO satellites and the information on the thermistors' location.

3

SOLAR AND THERMAL RADIATION PRESSURE MODELLING FOR IMPROVING THE GOCE HORIZONTAL WIND DATASET

N.A. Hładczuk, J. van den IJssel, F. Jacobs, C. Siemes, P.N.A.M. Visser

The Gravity Field and Steady-State Ocean Circulation Explorer (GOCE) satellite, which operated at an altitude of ~250 km, *provided neutral thermosphere mass density and crosswind observations in the dawn-dusk sectors throughout most of its operational lifetime (2009–2013). As a result of its Sun-synchronous orbit, GOCE's large solar panels remained at a near-perpendicular angle to the incoming solar radiation, leading to a significant radiation pressure acceleration. In this research, we focused on revisiting and reprocessing GOCE thermosphere mass density and crosswind data. We selected the coefficients describing the thermo-optical surface properties and employed a high-fidelity satellite geometry in a ray-racing simulation. Additionally, we distinguished between the solar flux in the visible and infrared bands and introduced a model for the satellite's thermal emission. The availability of the in-situ thermistor measurements allowed for the validation of the thermal model. Moreover, we replaced the Level-1b ion thruster data with raw telemetry, filling multiple data gaps. We analysed how incremental improvements in the radiation pressure modelling affected the observed crosswind speed. By replacing the panel model with the high-fidelity satellite geometry, the crosswind speed decreased up to* $5\,\mathrm{m\,s^{-1}}$. *The biggest difference reduction of* $40\,\mathrm{m\,s^{-1}}$ *resulted from introducing the*

This chapter has been published in Advances in Space Research **76**(11), 6899-6917, 2025 Hładczuk et al., 2025.

thermal model. Splitting the solar flux further decreases the observed crosswind speed by up to $8\,\mathrm{m\,s^{-1}}$*. The reduction in crosswind speed was most prominent during the first years of the mission when the solar activity was low. We compared the newly processed GOCE zonal wind data with respect to the most recent previous release. We observed a median absolute deviation decrease of* $10\,\mathrm{m\,s^{-1}}$ *around the south magnetic pole in the dawn sector. The yearly consistency of low-latitude zonal winds did not change significantly. The main obstacle in quantifying the improvement compared to the previous crosswind dataset stemmed from the fact that the previous and new datasets were generated with different crosswind estimation algorithms. The difference in thermosphere density compared to previously published datasets is minor since the effect of radiation pressure is most prominent in the cross-track direction. Finally, we verified the assumption about the energy accommodation coefficient of 0.82 and concluded that it remains valid after implementing the radiation pressure modelling improvements.*

3.1. INTRODUCTION

The Gravity Field and Steady-State Ocean Circulation Explorer (GOCE) was the first European Space Agency (ESA) Core Earth Explorer Mission, launched in March 2009 and operated until November 2013 (Floberghagen et al., 2011b). Its primary objective was to map Earth's gravity field and model the geoid height with unprecedented accuracy. The mission successfully achieved a range of multidisciplinary scientific goals, including applications in geodesy, geophysics, oceanography, glaciology, and climate research.

GOCE flew in a near-circular, Sun-synchronous dusk-dawn orbit with an inclination of 96.5°. The satellite altitude was 270 km at the beginning of the mission and was lowered to 240 km by the end of operations. This orbit was selected to provide optimal Earth coverage while minimizing the time spent in eclipses. As a result, one side of the satellite was always directed toward the Sun while the other was never directly illuminated by sunlight. The satellite's subsystems were powered by four body-mounted and two wing-mounted solar panels equipped with triple-junction gallium arsenide (GaAs) solar cells, which made GOCE the first gravimetry mission to use this technology.

GOCE was equipped with a Satellite-to-Satellite Tracking Instrument, which was used to determine the position and velocity, and star trackers that provided information on attitude (Drinkwater et al., 2007). Maintaining the satellite's low operational altitude was made possible by a drag-free control system enabled by ion propulsion (Andreis & Canuto, 2005). The core instrument onboard the spacecraft was the Electrostatic Gravity Gradiometer (EGG), measuring the gravity gradients along GOCE's orbit. The EGG consisted of three pairs of three-axis, servo-controlled accelerometers, providing independent measurements of the gravity gradient components (Drinkwater et al., 2007).

GOCE's low altitude, where aerodynamic accelerations are significant, provided unique conditions for obtaining highly accurate crosswind estimates. The availability of four years of GOCE wind data facilitated a number of studies. Because of its near-polar orbit and mostly fixed local time, GOCE winds remain uncontaminated by local solar time variations, providing an opportunity to study seasonal dependencies. GOCE data allowed the analysis of the spatial and temporal variability of thermospheric zonal winds (Molina & Scherliess, 2023)), helped to identify wind jets (Liu et al., 2016), and gave insights into intra-annual oscillations in upper thermospheric winds (M. S. Dhadly et al., 2020). Furthermore, GOCE cross-track wind data has been assimilated into wind models, effectively filling gaps in the twilight regions that are typically inaccessible through ground-based measurements such as Fabry–Perot Interferometers (Drob et al., 2015). However, studies also revealed that GOCE winds obtained from non-gravitational accelerations show substantial offsets compared to other space-based and ground-based observations (M. Dhadly et al. (2017) and M. S. Dhadly et al. (2018)). Moreover, characteristic jumps in GOCE winds have been identified at the locations where the satellite entered and exited eclipses (E. Doornbos et al., 2014).

The most recent version of GOCE data, prior to the one presented here, was version 2.0 in the ESA GOCE Data Collections Website, which is the exact same dataset as version V01, found in http://thermosphere.tudelft.nl. This dataset, consisting of both vertical and horizontal winds, was produced using an algorithm based on linear and angular accelerations as described in T. Visser et al. (2019). The algorithm relies on the measured accelerations to calculate a net force and torque acting on the satellite. Therefore, the

algorithm output is a pair of wind datasets, one force-derived and one torque-derived, which, after applying an offset correction, results in a final wind estimate.

The derivation of density and winds from the satellite's accelerometer data relies on the precise modelling of non-gravitational forces. For GOCE, the thrust exerted by the drag-free control system acts as an additional acceleration, which must first be added to the calibrated acceleration. Afterwards, the aerodynamic acceleration is obtained by subtracting the radiation pressure from the remaining signal. Likewise version V01, this study uses a high-fidelity GOCE geometry (March, Doornbos, & Visser, 2019) to model the aerodynamic drag.

This study aims to provide new insights into GOCE horizontal winds by reprocessing all data using enhanced processing standards and models. Crosswind data are particularly sensitive to acceleration modelling errors in the cross-track direction, where the main contributors are solar radiation pressure and the satellite's thermal emission. To take advantage of the high-fidelity geometry for radiation pressure modelling, we assigned appropriate thermo-optical surface properties to each geometry element. Such a model is then used in ray-tracing simulations to determine radiation pressure force coefficients. Ray-tracing is an efficient method for modelling the momentum exchange between incident radiation and the satellite surface while accounting for self-shadowing and multiple reflections. To optimize computational efficiency, the ray-tracing simulation is performed once for all directions of incidence, and the resulting coefficients are stored in a lookup table (Hładczuk et al., 2024; Siemes et al., 2023). This approach has been already adopted by various research groups (Bhattarai et al., 2022b; Li et al., 2018; Ziebart, 2004).

In the standard approach to Solar Radiation Pressure (SRP) modelling, the solar spectrum is assumed to be fully in the visible wavelength range. However, in reality, the interaction between the solar flux and the satellite surface is frequency-dependent. This aspect is often neglected or simplified due to uncertainties in the satellite surface properties. In this study, we divided the solar flux between the two main contributing wavelengths, infrared and visible, following a similar approach as Vielberg and Kusche (2020).

In addition to the SRP, the acceleration due to the satellite's thermal emission is the second largest contributor to the cross-track radiation pressure acceleration, accounting for one-fourth of the signal. Typically, the thermal effect is either neglected or modelled as simple instantaneous heat re-emission (Montenbruck et al., 2015; Vielberg & Kusche, 2020). State-of-the-art models account for transient heat conduction and characterize the heat exchange using thermal control parameters such as heat capacity, conductivity, and heat generation by the inner parts (Siemes et al., 2023; Wöske et al., 2019). Some studies additionally account for the efficiency of the solar arrays, defined as the amount of absorbed radiation converted into electricity instead of heat (Adhya, 2005; Hładczuk et al., 2024; Y. Wang et al., 2023).

In this study, we provide new insights into radiation pressure modelling by applying a ray-tracing technique and revisiting the selection of the thermo-optical properties of satellite materials. For a more realistic SRP model, we accounted for the visible and infrared contributions of the solar spectrum. We proposed a thermal model based on the transient heat conduction and accounted for the heat transfer through the satellite wing - a distinctive feature of the GOCE design. Finally, we validated the choice of model

control parameters by comparing the modelled temperatures to the readings from the GOCE thermistors.

The paper is structured as follows. First, in Section 3.2, we discuss the input data. Then, in Section 3.3, we explain the methodology of the radiation pressure modelling, including thermal emission and heat transfer through the satellite wing. Section 3.4 presents the results, including new crosswind estimates. Finally, Section 3.5 discusses the conclusions and opportunities for future work.

3.2. DATA

3.2.1. GOCE DATA

All GOCE Level-1b and Level-2 data collections, including the temperature readings, are freely available on ESA GOCE Data Collections Website. The GOCE satellite operated under drag-free control, using an ion thruster to continuously compensate for atmospheric drag in the in-flight direction. Previously published GOCE datasets were based on Level-1b ion thruster data. In this work, we used raw telemetry thruster data instead. This allowed us to fill numerous data gaps (280 gaps longer than 5 minutes). For the remaining data products, we used the most recent version of the Level-1b data. Additionally, we updated the accelerometer bias estimation (P. Visser & van den IJssel, 2016) to be consistent with that version of the accelerometer data.

To process GOCE density and crosswind data, we utilize the following models: NRLMSISE-00 model (Picone et al., 2002) to obtain the atmospheric composition and temperature and HWM07 (Drob et al., 2008) to account for in-track wind.

3.2.2. THERMISTORS DATA

Each panel of GOCE was equipped with a pair of Rosemount 0118MF temperature sensors, as shown on Figure 3.1. Unlike GRACE-FO (Hładczuk et al., 2024) and Swarm, GOCE's thermal sensors were installed on the rear side of each panel, making them unsuitable for direct use in thermal modelling. However, these thermistors can still serve as reference temperature. Being located beneath the panels and thus better insulated, their temperature readings record less extreme values than the outer temperatures we aim to model. An exception is a thermistor located on the rear side of the wing, which can be directly used to compare modelled and measured temperatures.

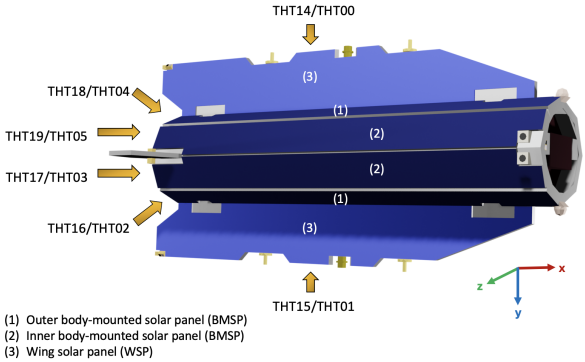

Figure 3.1: Approximate locations of the GOCE thermistor pairs on each panel. The pairs named THT17/THT03 and THT19/THT05 were mounted on the inner body-mounted solar panels (BMSP), whereas THT16/THT02 and THT18/THT04 were mounted on the outer BMSP. The sensors THT14/THT00 and THT15/THT01 were placed on the wing solar panels (WSP). Note that the thermistors are located on the rear side of the panels.

Figure 3.2 shows the temperature variation during a few orbits as well as the orbit mean temperature. We compared the temperature readings from thermistors on the same panel throughout the mission lifespan to examine thermal gradients across the surface. The difference within the thermistor measurements was at most 10 °C in the sunlight and 20 °C in the eclipse.

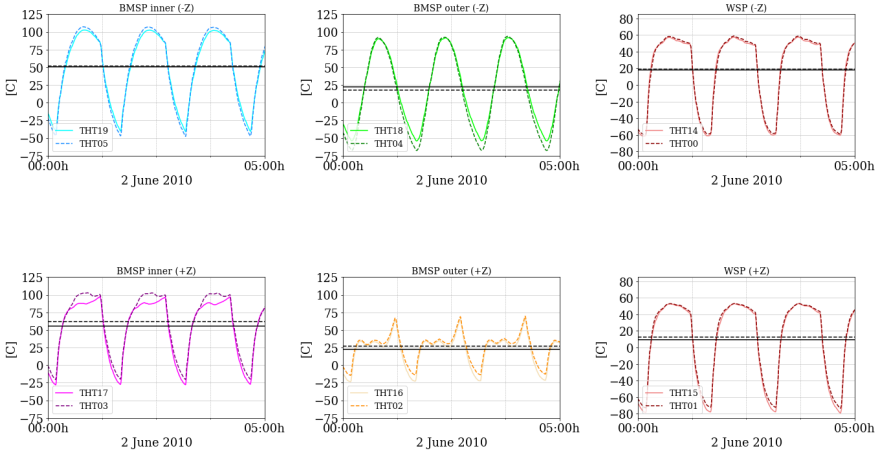

Figure 3.2: Temperature measurements of the thermistors placed on the same panel. The horizontal black lines show the orbit mean temperature of the corresponding thermistors. Acronym BMSP refers to the body-mounted solar panels, whereas WSP refers to the wing solar panels.

3.2.3. HIGH-FIDELITY GEOMETRY MODEL

For GOCE aerodynamic and radiation pressure modelling, we utilised the detailed geometry model illustrated in Fig. 3.1, similar to the ones developed for CHAMP, Swarm, and GRACE. The model, which consists of 2474 mesh triangles, was created using CAD software and constructed from technical drawings and pre-launch images (March, Doornbos, & Visser, 2019). The GOCE high-fidelity geometry model was used as input for a ray-tracing simulation to calculate radiation pressure force coefficients. To achieve this, we enhanced the model by assigning surface material properties to each mesh element. These properties were defined for both visible and infrared wavelengths. Details on the selection of surface coefficients are provided in Section 3.4.2.

3.3. METHODOLOGY

GOCE was equipped with the Electrostatic Gravity Gradiometer consisting of three orthogonal pairs of accelerometers, providing independent measurements of the gravity gradient components in the along-track, cross-track and vertical directions. Since GOCE accelerometers do not coincide with the satellite centre of mass, we are using the so-called common mode acceleration, which is obtained by averaging the accelerations measured along the corresponding axis of the gradiometer (P. Visser & van den IJssel, 2016).

To retrieve the aerodynamic signal, $\boldsymbol{a}_{\text{aero}}$, we subtract the other nongravitational accelerations from the calibrated common-mode accelerations $\boldsymbol{a}_{\text{cal}}$. These other nongravitational accelerations consist of solar radiation pressure (SRP), $\boldsymbol{a}_{\text{srp}}$, Earth albedo, $\boldsymbol{a}_{\text{alb}}$, Earth infrared radiation, $\boldsymbol{a}_{\text{ir}}$, and thermal acceleration, $\boldsymbol{a}_{\text{te}}$. The continuous thrust applied by the ion thruster as part of the drag-free control system acted as an additional acceleration, $\boldsymbol{a}_{\text{thr}}$, which cancelled the aerodynamic acceleration in the thrust direction. Therefore, we must add $\boldsymbol{a}_{\text{thr}}$ to $\boldsymbol{a}_{\text{cal}}$ to obtain the aerodynamic acceleration $\boldsymbol{a}_{\text{aero}}$

This amounts to

$$\boldsymbol{a}_{\text{aero}} = \boldsymbol{a}_{\text{cal}} - \boldsymbol{a}_{\text{srp}} - \boldsymbol{a}_{\text{ir}} - \boldsymbol{a}_{\text{alb}} - \boldsymbol{a}_{\text{te}} - \boldsymbol{a}_{\text{thr}}. \tag{3.1}$$

The neutral mass density ρ can be calculated from the acceleration along the satellite's x-axis $a_{\text{aero},x}$ by

$$\rho = \frac{2\, m\, a_{\text{aero},x}}{C_{\text{aero},x}\, V_{rel}^2}, \tag{3.2}$$

where m denotes the satellite mass, and V_{rel} is the satellite's velocity relative to the atmosphere. Since the satellite's x and y-axes are approximately aligned with the along-track and cross-track directions, respectively, we refer to the accelerations in these directions as the along-track and cross-track accelerations. The term $C_{aero,x}$ is the x-component of the aerodynamic coefficient vector (approximately aligned with the flight direction) intrinsically multiplied by the reference area. Due to the drag-free flight, information about GOCE's density primarily comes from thruster activation data.

Both neutral mass density and crosswind estimations rely on the accurate modelling of aerodynamic acceleration. Consequently, the errors in crosswind data arise from inaccuracies in the cross-track acceleration, with radiation pressure being a significant contributor. The effect of the radiation pressure mismodelling has been already studied

for higher-altitude satellites such as Swarm (van den IJssel et al., 2020), GRACE (Wöske et al., 2019), and GRACE-FO (Hładczuk et al., 2024; Siemes et al., 2023).

Figure 3.3 shows the ratio between the size of radiation pressure acceleration components with respect to the size of the aerodynamic acceleration. The magnitude of accelerations was calculated using a sliding one-month window root mean square (RMS). At GOCE altitude, during the early phase of the mission when the solar activity was low, the solar radiation pressure acceleration had magnitude up to 1% of the aerodynamic acceleration in the along-track direction (Fig. 3.3.a) and 50% in cross-track direction (Fig. 3.3.b). The reason for the small ratio of radiation pressure to aerodynamic acceleration in the along-track direction compared to the cross-track direction is twofold: drag, which acts approximately in the along-track direction, is much larger than the side forces acting in the cross-track direction. Second, the radiation pressure acceleration in the along-track direction is much smaller than that in the cross-track direction because of the dawn-dusk orbit.

The next largest contribution stems from thermal emission, with a magnitude of approximately one-fifth of the aerodynamic acceleration in the cross-track direction. The accelerations due to albedo and Earth's infrared emission have a negligible impact on the cross-track acceleration. As solar activity increases towards the end of the mission, the ratio between the radiation pressure acceleration component and the aerodynamic acceleration decreases.

Apart from the radiation pressure, additional error sources are accelerometer cross-track bias and accelerometer scale factor errors, as well as the misalignment of the thrust vector.

3.3.1. RADIATION PRESSURE MODELLING

The radiation pressure acceleration is defined as

$$\boldsymbol{a}_{\text{ext}}(\alpha,\beta) = \frac{1}{m}\int_{\lambda} P_{\text{ext}}(\alpha,\beta,\lambda)\boldsymbol{C}(\alpha,\beta,\lambda)\,d\lambda \tag{3.3}$$

where m is the satellite mass and P_{ext} is an external radiation pressure source such as the Sun (solar radiation pressure) or the Earth (infrared radiation and albedo). The coefficient $\boldsymbol{C}$ depends on the radiations's wavelength λ, and the angles α and β, which describe the orientation of the satellite to incident radiation. The angles can be derived using a unit vector fixed to the satellite reference frame, $\boldsymbol{u}_{\text{sat}}$, pointing from the radiation source towards the satellite:

$$\boldsymbol{u}_{\text{sat}} = \begin{bmatrix} u_x \\ u_y \\ u_z \end{bmatrix}, \quad \alpha = \arcsin(u_z), \quad \beta = \arctan_2(u_y, -u_x). \tag{3.4}$$

The solar radiation pressure $P_{\text{srp}}(\lambda)$ at the position of the satellite is calculated using the solar radiation pressure at one astronomical unit, $P_{1\text{AU}}$, and the distance from the Sun to the satellite $\|\boldsymbol{r}_{\text{sat}} - \boldsymbol{r}_{\text{Sun}}\|$:

$$P_{\text{srp}}(\lambda) = \left(\frac{1\text{AU}}{\|\boldsymbol{r}_{\text{sat}} - \boldsymbol{r}_{\text{Sun}}\|}\right)^2 P_{1\text{AU}}(\lambda). \tag{3.5}$$

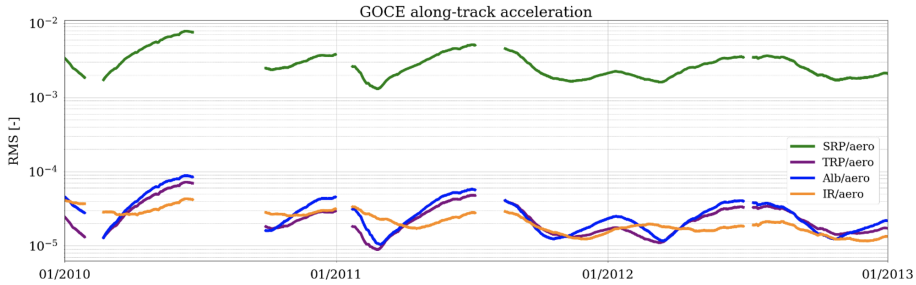

(a)

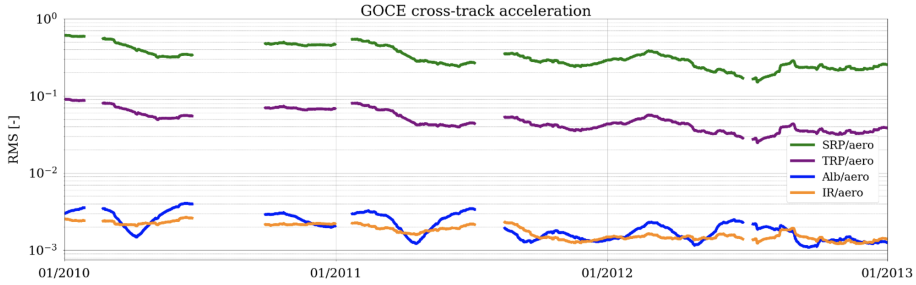

(b)

Figure 3.3: Ratio between the radiation pressure components and the aerodynamic coefficient (aero). The radiation pressure components are: solar radiation pressure (SRP), thermal radiation pressure (TRP), Earth albedo (Alb), and Earth infra-red radiation (IR). The magnitude of accelerations was calculated using a sliding one-month window root mean square (RMS).

The solar radiation pressure at 1AU is commonly approximated by the ratio of the mean solar constant $\Phi = 1361\,\mathrm{W\,m^{-2}}$ to the speed of light c, (i.e. $P_{1\mathrm{AU}} = \Phi/c = 4.53\,\mu\mathrm{N\,m^{-2}}$). The mean solar constant was estimated using CERES data from 2000 to 2024. We found the temporal variation in the solar flux to have a negligible effect on the acceleration and, therefore, did not account for it in this work.

The solar constant is an average of the Sun's energy flux integrated over all wavelengths. We accounted for dependency on both visible and infrared frequency bands of the solar spectrum, departing from the standard approach that considers only the visible range. Since the satellite material properties are typically available only for the visible and infrared wavelengths, we approximate the total flux by evenly distributing it between these bands (50% visible and 50% infrared). This method is similar to the extended SRP model proposed by Vielberg and Kusche (2020). Subsequently, we introduced the solar constant values for the visible and the infrared parts of the spectrum $\Phi_{vis} = 680.5\,\mathrm{W\,m^{-2}}$ and $\Phi_{ir} = 680.5\,\mathrm{W\,m^{-2}}$, respectively.

To model the visible and infrared radiation pressure coefficient $\boldsymbol{C}_{vis}$ and $\boldsymbol{C}_{ir}$, we augmented the GOCE aerodynamic model with thermo-optical surface properties and employed a ray-tracing technique. The advantage of this method is that it accounts for both self-shadowing and multiple reflections. The details on the ray-tracing algorithm

can be found in Siemes et al. (2023) and Hładczuk et al. (2024). The method was used to calculate the acceleration due to solar radiation pressure, Earth's infrared radiation, and albedo. For albedo and Earth's thermal emission, we use monthly averaged maps based on Earth Radiation Budget Experiment (ERBE) satellite data (E. Doornbos et al., 2014). We evaluated the impact of replacing the ERBE data with more precise Clouds and Earth's Radiant Energy System (CERES). However, the differences at the acceleration level were negligible given the size of the radiation pressure acceleration contributions, as shown in Figure 3.3.

3.3.2. THERMAL EMISSION MODELLING

The implemented thermal model is based on independent panels outlining the GOCE satellite's geometry. The net heat exchange of an individual panel j is

$$\dot{Q}_j = (1 - e_j)\,\dot{Q}_{\text{abs},j} - \dot{Q}_{\text{emit},j} - \dot{Q}_{\text{cond},j}, \tag{3.6}$$

where $\dot{Q}_{\text{abs},j}$ denotes absorbed radiation, $\dot{Q}_{\text{emit},j}$ emitted radiation, and $\dot{Q}_{\text{cond},j}$ conductive heat exchange either with the satellite body or through the satellite wing depending on the panel. The efficiency e_j represents the fraction of absorbed energy converted into electricity (Hładczuk et al., 2024; Y. Wang et al., 2023).

Since the panel model does not account for self-shadowing, using such a model to account for the satellite's thermal emission may introduce errors. Therefore, we implemented a modified version of the panel model of Dumontel (2010), estimating the illuminated area of the Sun-opposing horizontal stabiliser instead of using the total area. This was possible due to GOCE's distinctive orbit, where the orientation of the Sun-facing and Sun-opposing panels remains roughly fixed.

In the first step of numerical implementation, panels absorb the incoming radiation originating from the Sun and Earth, including albedo. Our calculations account for the dependency on both visible and infrared parts of the solar spectrum. The change in heat due to absorbed radiation is

$$\dot{Q}_{\text{abs},j} = (\Phi_{vis}\, c_{\text{vis},a,j} + \Phi_{ir}\, c_{\text{ir},a,j})\, A_j \cos\theta_j, \tag{3.7}$$

where $c_{\text{vis},a,j}$ is the absorption coefficient for visible light, $c_{\text{ir},a,j}$ is the absorption coefficient for infrared radiation, A_j is the area of the panel, and θ_j is the angle between the panel's outward normal and the vector from the satellite to the radiation source. The heat absorption is followed by heat loss toward space following the Stefan-Boltzmann law,

$$\dot{Q}_{\text{emit},j} = A_j\, c_{\text{ir},a,j}\, \sigma\, T_j^4, \tag{3.8}$$

where T_j is the absolute temperature of the satellite panels and σ is the Stefan-Boltzmann constant.

In the case of the GOCE satellite, two scenarios can be distinguished. For the panels attached directly to the satellite body, thermal conduction k_j between the satellite walls and the inner body T_{body} occurs

$$\dot{Q}_{\text{cond},j} = k_j (T_j - T_{\text{body}}). \tag{3.9}$$

The heat change of the satellite body $\dot{Q}_{\text{body}}$ is then defined as

$$\dot{Q}_{\text{body}} = \dot{Q}_{\text{gen}} + \sum_j \dot{Q}_{\text{cond},j}, \tag{3.10}$$

where $\dot{Q}_{\text{gen}}$ stands for the internal heat generated by the payload and satellite systems.

The second scenario concerns elements where the surface area connected to the satellite body is significantly smaller than the panel area, such as the satellite wings or the stabilizers. In these cases, instead of the thermal conduction towards the satellite body we consider the heat transfer through the panel

$$\dot{Q}_{\text{cond},j} = \frac{(T_{j_1} - T_{j_2})}{R_j}, \tag{3.11}$$

where T_{j_1} and T_{j_2} denote two sides of the panel, and R_j is the panel's thermal resistance, noting that $R_j = k_j^{-1}$.

The panels and body temperatures are updated by

$$T_j(t + \Delta t) = T_j(t) + \frac{\dot{Q}_j}{C_j}\Delta t, \tag{3.12}$$

and

$$T_{\text{body}}(t + \Delta t) = T_{\text{body}}(t) + \frac{\dot{Q}_{\text{body}}}{C_{\text{body}}}\Delta t, \tag{3.13}$$

where C_j and C_{body} are the thermal capacity of the panels and the satellite body, t is time, and Δt is the time difference to the next time step.

In the last step, the thermal radiation pressure acceleration

$$\boldsymbol{a}_{\text{te}} = -\frac{2}{3}\sum_j \frac{\dot{Q}_{\text{emit},j}}{m\,c}\boldsymbol{n}_j \tag{3.14}$$

is calculated, where $\boldsymbol{n}_j$ is the outer panel normal of the j-th surface element.

THERMAL MODEL CONTROL PARAMETERS

The proposed thermal model includes the following control parameters: heat capacitance of the panels (C_j) and the body (C_{body}), thermal resistance of the panels (R_j), efficiency of the solar cells (e_j), and internally generated heat ($\dot{Q}_{\text{gen}}$). Due to the characteristics of the GOCE orbit, the geometry can be divided into Sun-facing elements (solar panels) and Sun-opposing elements (insulation foil). Since the main thermal impact originates from the illuminated parts of the satellite (Eq. 3.8), we focus in this section solely on describing the thermal properties of the Sun-facing panels.

The GOCE satellite was equipped with four body-mounted solar panels, consisting of two larger inner panels and two smaller outer panels, along with two wing solar panels, as shown in Fig. 3.1. GOCE solar panels contain triple-junction Gallium Arsenide (GaAs) solar cells, similar in design to those used on the Swarm and GRACE-FO missions (Kornfeld et al., 2019).

The efficiency of the solar cells decreases with the temperature, as shown in Figure 3.4. Since the efficiency is only relevant when the solar panels are sunlit, we consider the following temperatures: For the satellite front wings, we assume a temperature of around 70 °C, for the outer body-mounted panels 100 °C, and for the inner body-mounted panels 140 °C, which translates to cell efficiencies of 23%, 21%, and 18%, respectively. These temperatures are consistent with those predicted by our thermal model. For reference efficiency, we used the values provided at the beginning-of-life. However, it should be noted that the difference in the beginning and end-of-life efficiency provided by the documentation is less than 1%.

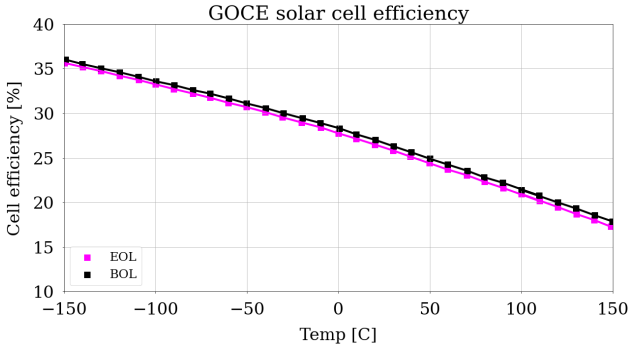

Figure 3.4: Efficiency of GOCE solar cells in the beginning-of-life (BOL) and end-of-life (EOL) provided in the technical documentation (Dutch Space, 2006).

The area of a single solar cell is 30.18 cm^2 (Dutch Space, 2005) and the number of cells per panel is 676 for each of the WSP, 338 for each of the outer BMSP and 390 for each of the inner BMSP (Dutch Space, 2005). The effective efficiency of the whole panel was estimated by calculating the packing factor, taking into account the area covered by the photovoltaic cells (Hładczuk et al., 2024). For the BMSP, this yields the effective efficiencies of 10% and 11% for the inner and outer panels, respectively (packing factors: 0.56 and 0.53), and 16% for the WSP (packing factor 0.72). It is worth pointing out that cell efficiency varies slightly throughout the mission lifespan, and manufacturers usually define them separately for the beginning and end of life (Figure 3.4). However, in this work, we consider this change negligible.

The thermal capacitance determines the ability of the panel to store heat and depends on the panel temperature. The values for the BMSP and WSP were based on the information provided in the technical documentation (Dutch Space, 2006). Figure 3.5 shows temperature-dependent thermal capacitance of the front and rear sides of the wing. The temperature of these panels remains fairly constant for GOCE, due to the Sun-synchronous orbit, with the exception of the eclipse passes. In this work, we use a fixed value selected in accordance with the temperature that the satellite reaches in sunlight. We estimate that the front of the GOCE wing heats up to 70 °C, and the rear side remains around 50 °C. Scaling through the wing area leads to approximate values of heat capacitance of 6100 JK^{-1} and 2800 JK^{-1} for front and rear, respectively.

For the body-mounted panels, we follow a similar approach, with the operational

modelled temperatures as described above. This leads to the thermal capacitances of 4300 JK^{-1} and 3800 JK^{-1} for larger and smaller panels, respectively.

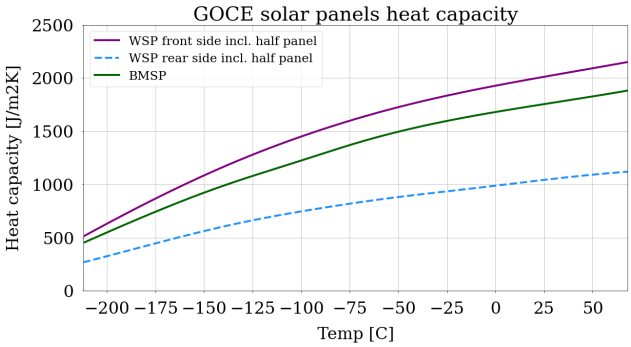

Figure 3.5: Heat capacity of GOCE solar panels body-mounted solar panels (BMSP) and wing solar panels (WSP) as provided in the technical documentation (Dutch Space, 2006). Values for higher temperatures have been linearly interpolated.

The internal heat generated by the onboard electronics was adjusted to assure realistic operational temperature (25 °C). The internal heat generation has been set to 70 W.

The details on calculating thermal resistance values for GOCE are provided in the next section.

THERMAL RESISTANCE

Thermal resistance is a function of a fabric's thickness and thermal conductivity and determines the material's insulation properties. It can be defined as the ratio of the temperature difference between the two faces of a material to the rate of heat flow per unit area (Mishra et al., 2018).

Both the satellite wings and the body-mounted solar panels were thermally decoupled from the platform by titanium brackets and thermal washers (Cataloglu et al., 2004). Moreover, the MLI blankets were placed below the body-mounted panels for additional insulation (Battaglia et al., 2008). This assures high thermal resistance towards the satellite body.

To precisely model the heat flow through the wing wall, we use the information about the material layers provided in the documentation. In a composite structure such as the satellite wing, the total thermal resistance R_{total} can be calculated as a sum of the individual resistance of each layer by

$$R_{total} = \frac{1}{A}\sum_j R_j = \frac{1}{A}\frac{l_j}{k_j}, \tag{3.15}$$

where l_j is a thickness of the layer, k_j is the conductivity and A area (Adhya, 2005).

Figure 3.6 depicts the schematic cross-section of the GOCE solar panel comprising 11 materials based on the 'GOCE Solar Array: Detailed Thermal Model Analysis' document (Dutch Space, 2006).

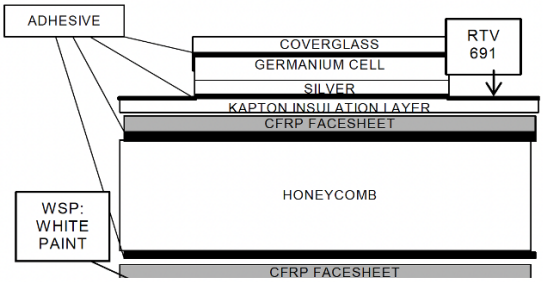

Figure 3.6: The schematic cross-section of typical GOCE solar panel (Dutch Space, 2006).

Table 3.1 summarizes each layer's properties, considering the material type, thickness, and conductivity. Part of the information stems from Adhya (2005), who carried out a similar study to identify and describe the structure of a GPS Block IIR satellite.

Table 3.1: Material properties by layer. The thickness refers to the thickness of a single layer.

Layer [-]	**Material** [-]	**Thickness** [m]	**Conductivity** [$\mathrm{W m^{-1} K^{-1}}$]	**Layers** [-]
1	Coverglass	2.54×10^{-4}	1.417[2]	1
2	Adhesive RTV	1.02×10^{-4}	0.157[2]	1
3	Germanium cell	2.30×10^{-4}	41.0[1]	1
4	Silver	1.00×10^{-4}	419[1]	1
5	Adhesive RTV	1.02×10^{-4}	0.157[2]	1
6	Kapton insulator	2.54×10^{-5}	0.157[2]	1
7	CFRP	0.001	0.35[1]	5
8	Adhesive RTV	1.02×10^{-4}	0.157[2]	1
9	Honeycomb	6.52×10^{-2}	2.03[2]	1
10	Adhesive RTV	1.02×10^{-4}	0.157[2]	1
11	CFRP	0.001	0.35[1]	5
12	White paint	1.00×10^{-4}	0.20[1]	1

[1] Material property data: https://www.matweb.com/, accessed on 20/08/2024.
[2] (Adhya, 2005).

Using the information from Table 3.1, the total resistance of the wing was calculated following Eq. 3.15 considering the panel areas. Note that the number of layers in the wing varies depending on whether the surface element is covered by solar cells or not. To distinguish between the area covered by the solar cells and that covered only by the adhesive, the thermal resistance was calculated for the whole panel surface and then scaled through the packing factor.

The total thermal resistance R of a panel is

$$R = R_{\text{cell}} + R_{\text{adhesive}} = \frac{1}{A_{\text{cell}}} \sum_{j=1}^{4} R_j + \frac{1}{A_{\text{adhesive}}} \sum_{j=5}^{12} R_j, \tag{3.16}$$

where A_{adhesive} is the area covered by adhesive (which corresponds to the total panel area of 2.828 m), and A_{cell} is the fraction of the surface covered by the solar cells (see packing factor, Sec. 3.3.2).

From Table 3.1, we deduced $R_{\text{cell}} = 0.00042\,\text{WK}^{-1}$ and $R_{\text{adhesive}} = 0.01469\,\text{WK}^{-1}$. Therefore, the total thermal resistance of a GOCE wing amounts to $R = 0.01469\,\text{WK}^{-1}$. For the wing solar panels, for which the information about the layers is available, we can calculate the thermal resistance. Moreover, we have the rear-side thermistor measurement available to verify the temperatures resulting from these resistance values. As for the body-mounted panels, they remain very well insulated from the interior, assuring the operational internal temperature of approximately 25 C. We used this criterion to calculate the thermal resistance instead of relying on layers.

3.4. RESULTS AND DISCUSSION

3.4.1. SOLAR RADIATION PRESSURE MODELLING

In this work, we distinguish between the two frequency bands of the solar spectrum: visible and infrared (see Sec. 3.3.1). Typically, the total solar flux is approximated by integrating over all wavelengths and assuming that interactions occur only at the visible wavelength (i.e., only the visible surface properties are used in combination with the total solar flux). In our approach, we select the appropriate surface coefficients based on the specific wavelength, using either visible or infrared properties. Figure 3.7 illustrates an example of two satellites, GOCE and Gravity Recovery and Climate Experiment Follow-On (GRACE-FO), showing the differences in solar radiation pressure (SRP) acceleration when the flux is split by wavelength or integrated. For both satellites, splitting the solar flux increases the radiation pressure estimate in the cross-track direction. The differences, reaching up to $4\,\text{nm}\,\text{s}^{-2}$ for GOCE and $3\,\text{nm}\,\text{s}^{-2}$ for GRACE-FO, directly impact the crosswind estimation. On the other hand, the along-track acceleration decreases by approximately $1\,\text{nm}\,\text{s}^{-2}$ for both satellites when the split flux is used. The changes are negligible in the radial direction. This pattern may vary depending on the satellite, its surface properties and orbital characteristics.

To our knowledge, no publicly available document provides official information on GOCE's thermo-optical surface properties. Therefore, the ray-tracing model was based on the information about satellite materials available in the satellite thermal control documentation (Battaglia et al., 2008; Valentini et al., 2006) and the information on the thermo-optical properties of the specific materials used for the satellite design (P. Fortescue et al., 2011b; Silverman, 1995). The satellite surface properties used in the ray-tracing simulation are summarized in Table 3.2. To model the eclipse in this work, we utilize the Solar radiation pressure with Oblateness and Lower Atmospheric Absorption, Refraction, and Scattering Curve Fit (SOLAARS-CF) model (Robertson et al., 2015).

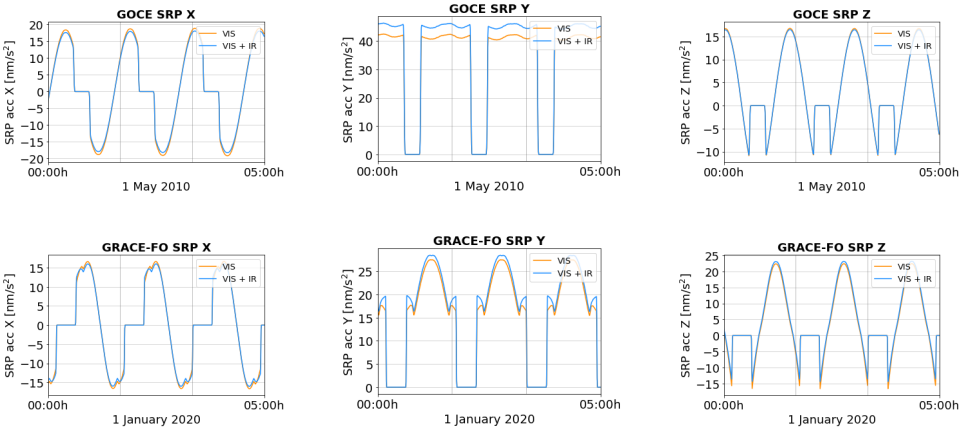

Figure 3.7: Solar radiation pressure acceleration (SRP) in along-track, cross-track and radial directions calculated using integrated (orange) and solar flux split by wavelength (blue). The top and bottom rows show examples from the GOCE and GRACE-FO satellites, respectively.

Table 3.2: GOCE thermo-optical surface coefficients for visible and infrared light. The visual representation of the Sun-facing panels is shown in Figure 3.1.

Panel	A_j (m^2)	$n_{x,j}$ (-)	$n_{y,j}$ (-)	$n_{z,j}$ (-)	$c_{\text{vis},a,j}$ (-)	$c_{\text{vis},d,j}$ (-)	$c_{\text{vis},s,j}$ (-)	$c_{\text{ir},a,j}$ (-)	$c_{\text{ir},d,j}$ (-)	$c_{\text{ir},s,j}$ (-)
Front	0.865	1.0	0.0	0.0	0.07	0.23	0.70	0.74	0.20	0.06
Rear	0.865	-1.0	0.0	0.0	0.10	0.05	0.85	0.80	0.15	0.05
Sun-facing side (solar panels)										
Body 1	2.067	0.0	-0.924	-0.383	0.95	0.05	0.00	0.60	0.29	0.11
Body 2	1.918	0.0	-0.383	-0.924	0.95	0.05	0.00	0.60	0.29	0.11
Body 3	1.918	0.0	-0.383	0.924	0.95	0.05	0.00	0.60	0.29	0.11
Body 4	2.067	0.0	-0.924	0.383	0.95	0.05	0.00	0.60	0.29	0.11
Wing 1/2	2.828	0.0	-1.0	0.0	0.95	0.05	0.00	0.60	0.29	0.11
Sun-opposite side										
Body 1	1.874	0.0	0.383	-0.924	0.15	0.35	0.50	0.05	0.25	0.70
Body 2	1.601	0.0	0.924	-0.383	0.15	0.35	0.50	0.05	0.25	0.70
Body 3	1.601	0.0	0.924	0.383	0.15	0.35	0.50	0.05	0.25	0.70
Body 4	1.874	0.0	0.383	0.924	0.15	0.35	0.50	0.05	0.25	0.70
Wing 1/2	2.828	0.0	1.0	0.0	0.35	0.55	0.10	0.75	0.20	0.05
Radiators										
Radiator Front	0.036	1.0	0.0	0.0	0.10	0.20	0.70	0.80	0.15	0.05
Radiator Rear	0.036	-1.0	0.0	0.0	0.10	0.20	0.70	0.80	0.15	0.05
Radiator 1	0.101	-0.924	0.383	0.101	0.10	0.20	0.70	0.80	0.15	0.05
Radiator 2	0.061	-0.383	-0.924	0.061	0.10	0.20	0.70	0.80	0.15	0.05

3.4.2. THERMAL EMISSION

The crosswind data are sensitive to acceleration modelling errors in the y-direction. Moreover, the thermal emission is proportional to the temperature raised to the fourth power (Eq. 3.8), meaning that the panels with higher temperatures exert greater thermal acceleration. Thus, in this work, we focus specifically on modelling the temperature of the solar arrays, which were on the Sun-facing side of the satellite and, therefore, reached much hotter temperatures than the panels on the Sun-opposing side.

Figure 3.8 gives an overview of the modelled and measured temperatures of all solar arrays during the timespan of a few orbits. The measured temperatures were calculated as the average value between two thermistors located on the same panel. It is important to note that the thermistors serve only as a rough reference for our thermal modelling, and direct comparison is not possible. Since the thermistors were mounted on the rear side of the panels, they were shielded from direct sunlight. Consequently, the measured temperatures exhibit smaller variations compared to the modelled ones, while displaying a similar pattern. The body-mounted inner panels (Fig. 3.8a, Fig. 3.8d) reach the highest temperatures because they have the smallest incidence angle to the incoming radiation from the Sun. In contrast, the temperature is lower for the upward- and downward-facing outer panels (Fig. 3.8b, Fig. 3.8e). As shown here, during the sum-

mer the Earth-opposed panels get hotter than the Earth-facing panels due to the tilt of the orbital plane with respect to the Sun. Figures 3.8c and 3.8f present the temperature model for both the front and rear sides of the wing. As anticipated, the modelled orbit mean temperatures are higher than those recorded by the thermistors, with the exception of the Earth-facing panel (Fig. 3.8e), where the modelled and measured temperatures are of similar magnitude. This could be attributed to errors in the thermistor's measurements or inaccuracies in Earth's albedo and infrared radiation modelling.

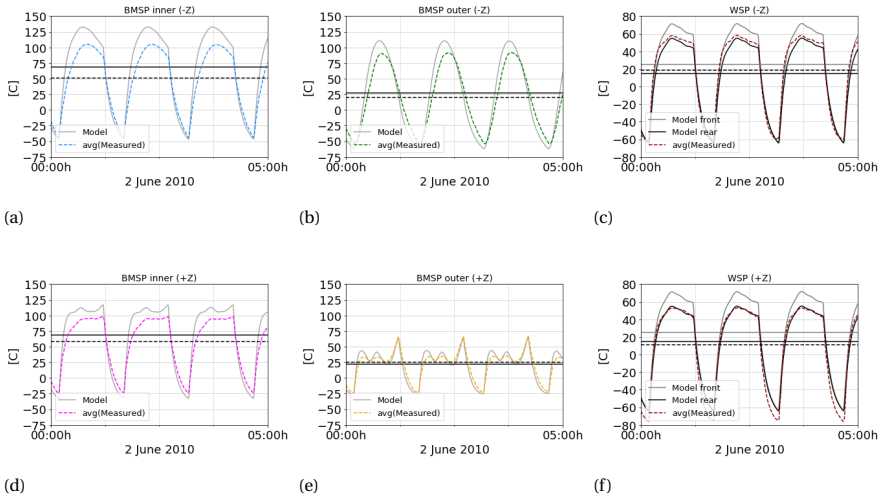

Figure 3.8: Comparison between the modelled (solid line) and measured (dashed line) temperatures per panel. The horizontal black lines show the orbit mean temperature of the model (solid) and measurements (dashed). The panels presented in the top row are Earth-opposed, while the panels in the bottom row are Earth-facing.

The results of the thermal modelling for the GOCE wing are shown in Figure 3.9. In this work, we use the argument of latitude to illustrate the position of the satellite along the orbit. The horizontal axis of the figure refers to time, and the vertical axis refers to the argument of latitude. Argument of latitudes of 0° and 180° refer to the ascending and descending equator crossings, while 90° and 270° represent the northern and southernmost points of the orbit, respectively.

As expected, the modelled temperature of the front side of the wing (Fig. 3.9a, 3.9b), which is facing the Sun, exhibits a higher value compared to the rear side (Fig. 3.9c, 3.9d). Since the panel geometry used for thermal modelling does not account for shadowing, the modelled temperature of the front and rear sides is symmetrical for both Earth-facing and Earth-opposed wings. Figure 3.9e shows the average measured temperature of two thermistors on Earth-facing wing, and Figure 3.9f shows the same for the Earth-opposed wing. Figure 3.9g and 3.9h shows the difference between the measured and modelled temperatures. For the Earth-facing wing, the temperature differences in sunlight are approximate 3 °C, and in the shadow, they remain within 15 °C. In case of the Earth-opposed wing the differences are respectively 7 °C and 20 °C. This indicates that the difference between the modelled and measured temperature has the same magnitude

as the differences between measurements of the thermistors located on the same wing (Sec. 3.2.2).

Table 3.3 summarizes the material properties used for thermal modelling. Only the geometry elements which contribute primarily to the total thermal emission were summarized in the table. The remaining elements, such as the stabilizer, contribute less than 0.5 nm/sec^2 to the total cross-track thermal acceleration and, therefore, were not listed. It should be mentioned that in our model, we assume that the panel is heated evenly.

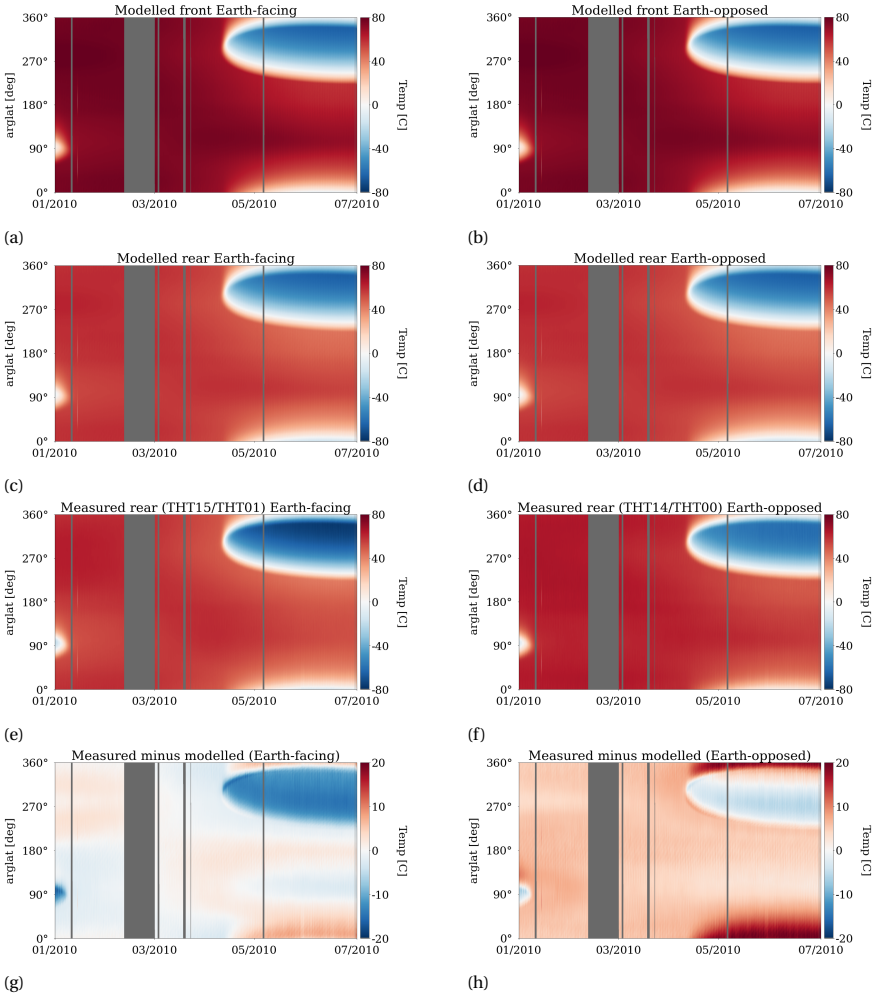

Figure 3.9: Temperature of the GOCE wing. The left column shows the temperature of the Earth-facing wing, and the right column of the Earth-opposed wing. The first and second rows depict the front and rear modelled temperatures, respectively. The third row shows the average measured temperature by the THT14/THT01 thermistors (e) and THT15/THT00 thermistors (f). The last row shows the difference between the measured temperatures and modelled ones.

Table 3.3: GOCE thermal radiation model. The internal heat generation has been set to 70 W. It should be noted that the panel thermal capacitance is inversely proportional to the resistance, $k_j = R_j^{-1}$. The values of areas and panel normals are identical to those presented in Table 3.2.

Panel	C_j [JK^{-1}]	k_j [WK^{-1}]	e_j [-]
Front	4000	0.1	-
Rear	9000	0.1	-
Sun-facing side (solar panels)			
Body 1	4300	0.1	0.10
Body 2	3800	0.1	0.11
Body 3	3800	0.1	0.11
Body 4	4300	0.1	0.10
Wing 1/2	6100	68.9	0.15
Sun-opposite side			
Body 1	2000	0.1	-
Body 2	2000	0.1	-
Body 3	2000	0.1	-
Body 4	2000	0.1	-
Wing 1/2	2800	68.9	-
Radiators			
Radiator Front	400	0.1	-
Radiator Rear	400	0.1	-
Radiator 1	400	0.1	-
Radiator 2	400	0.1	-

3.4.3. HORIZONTAL CROSSWIND AND DENSITY

The low operational altitude of GOCE, which led to high aerodynamic accelerations, provided an advantage for obtaining valuable crosswind data. The newly produced GOCE neutral thermosphere density (Fig. 3.10) and horizontal wind datasets (Fig. 3.11) labelled as Version V02 are available on the TU Delft Thermosphere FTP Server[1]. These datasets incorporate the advancements in SRP modelling, including splitting the solar flux into the visible and infrared bands, using the ray-tracing algorithm in combination with the high-fidelity satellite geometry, and updating the thermo-optical surface coefficients. It also includes the thermal satellite model to account for the acceleration due to the satellite's thermal emission.

[1] Since 2026 HTTPS Server https://thermosphere.tudelft.nl/data/

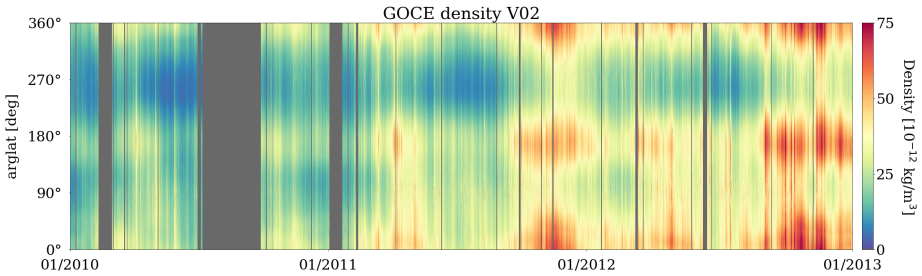

Figure 3.10: Version V02 of the GOCE neutral thermosphere mass density.

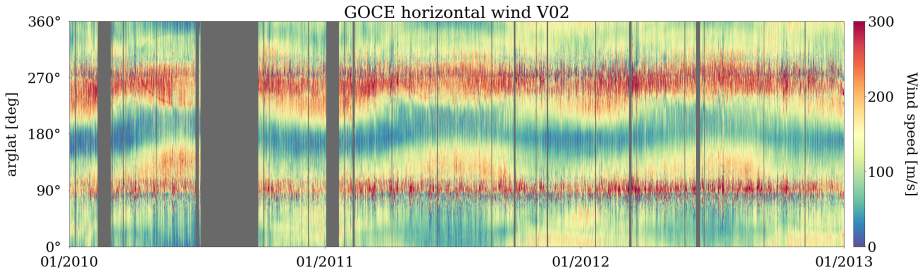

Figure 3.11: Version V02 of the GOCE horizontal windspeed.

Figure 3.12 quantifies the impact of the advances on the horizontal winds by incrementally introducing additional features in the radiation pressure model, as indicated in Table 3.4. In the simplest case (a), the satellite geometry is represented by a panel geometry, the satellite's thermal emissions are not modelled, and solar radiation pressure is obtained from the flux integrated over the whole spectrum in combination with surface coefficients for visible light. Then, we introduce the high-fidelity geometry in case (b), the thermal model in case (c), and distinguish between visible and infrared wavelengths of the solar flux in case (d). To highlight the impact of each modelling feature, we show the difference between cases (a) and (b), (b) and (c), and (c) and (d). For the comparison, we selected the time interval from 2010 to 2013, aligning with the satellite's operational phase while avoiding periods with too many manoeuvres.

Table 3.4: Summary of GOCE radiation pressure modelling approaches.

Case	Thermal model included	Geometry model	Solar flux split by wavelength
(a)	No	Panel	No
(b)	No	High-fidelity	No
(c)	Yes	High-fidelity	No
(d)	Yes	High-fidelity	Yes

For all three panels of Fig. 3.12, the biggest differences appeared in 2010, when the solar activity was lowest and, consequently, the aerodynamic acceleration making changes in the radiation pressure acceleration more noticeable. By replacing the panel model with the high-fidelity geometry (Fig. 3.12.1), the estimated horizontal wind speed decreased by approximately 5 m s^{-1}. The largest decrease of up to 40 m s^{-1} resulted from introducing the thermal model (Fig. 3.12.2). In this case, the satellite emitted infrared radiation due to its nonzero absolute temperature. As the satellite heated up in the sunlit part of the orbit due to absorbed solar radiation, the resulting thermal emission acceleration caused changes in the estimated wind. The changes in the estimated wind shortly after the satellite entered the eclipse can be explained by the fact that it took several minutes before the satellite cooled down so much that the thermal emission acceleration became insignificant (for eclipses, see Fig. 3.13). Finally, splitting the solar flux by wavelength further reduced the estimated wind by up to 8 m s^{-1} (Fig. 3.12.3).

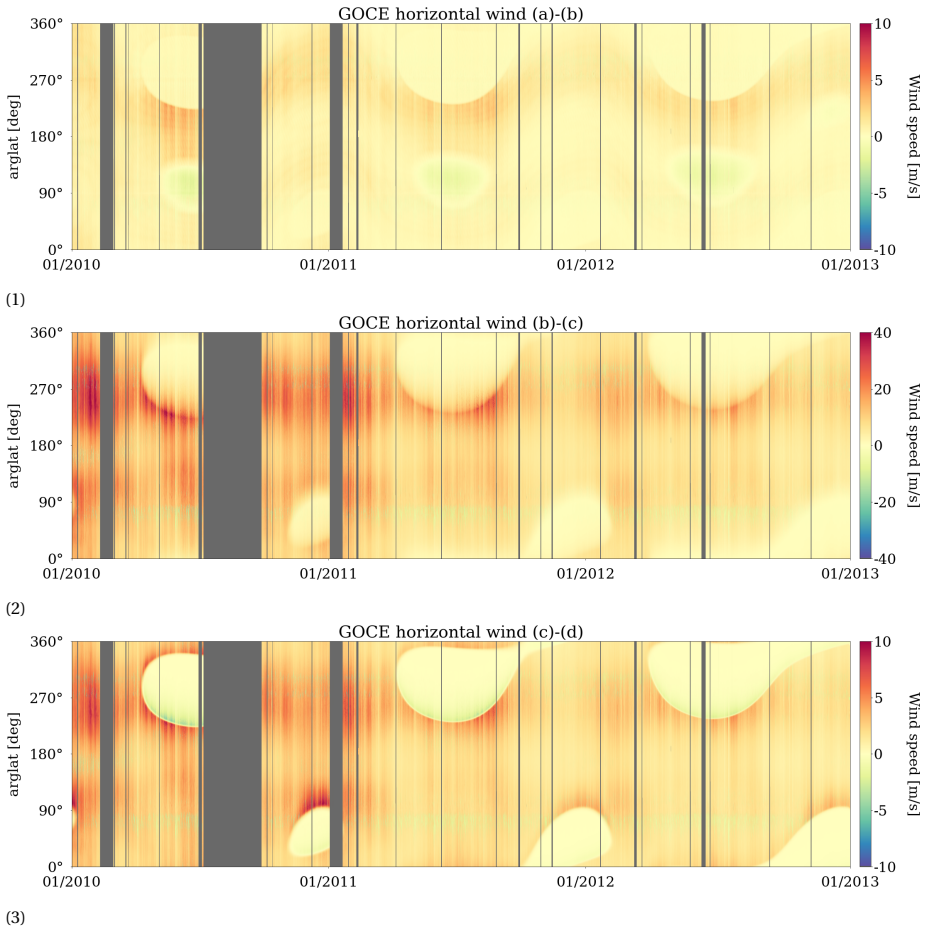

Figure 3.12: Quantification of the advancements in the radiation pressure modelling as described in Table 3.4. The difference in the scale of the colour bars should be noted.

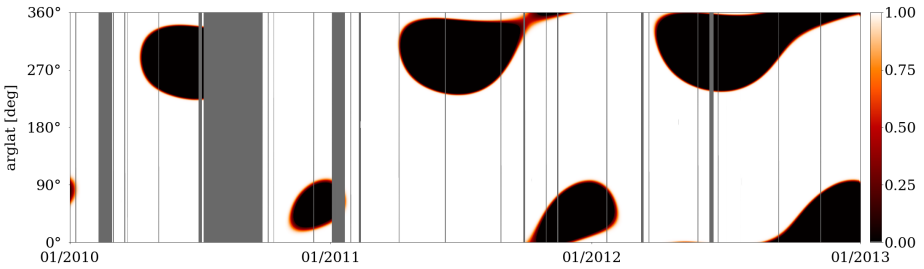

Figure 3.13: GOCE shadow function.

The previous version of the GOCE crosswind dataset is labelled version V01 in TU Delft's thermosphere database and version 2.0 in ESA's GOCE data collections website (despite the different versions, it is the same dataset). In this work, we will refer to the newly produced dataset as V02 and the previously produced dataset as V01, following the convention in the TU Delft's thermosphere database.

The version V01 dataset provides both the thermosphere neutral density and crosswind estimates. The crosswind data was generated using a method described by T. Visser et al. (2019). The method utilises the concept of simultaneous observation of linear and angular accelerations, so the derived winds rely on both forces and torque modelling. T. Visser et al. (2019) used the high-fidelity satellite geometry model (Sec. 3.2.3) for aerodynamic modelling, assuming diffuse reflections of gas particles with incomplete energy accommodation of $\alpha_E = 0.82$ (March, Doornbos, & Visser, 2019). They used a simplified solar radiation pressure model, assuming a reflectance of zero for the side covered by solar panels and 0.8 for the other side. For modelling of albedo and Earth's infrared radiation, they utilized the monthly mean top-of-atmosphere albedo and infrared flux maps obtained from the CERES SYN1deg product[2]. The eclipse was defined by the physics-based SOLAARS-CF model (Robertson et al., 2015).

To produce version V02, we retrieved the crosswind estimates with the iterative algorithm proposed by E. Doornbos et al. (2010), which relies solely on the satellite linear accelerations. The intrinsic differences between the methods of E. Doornbos et al. (2010) and T. Visser et al. (2019) may lead to discrepancies in crosswind estimates, making the interpretation of the differences challenging. Nevertheless, version V01 can still serve as a valuable reference for comparison between the two datasets.

Since interpreting the crosswind comparison between versions V01 and V02 directly can be challenging, we first compare only the results of the solar radiation pressure modelling. Figure 3.14 shows the SRP acceleration used in V01 and V02. There is a good agreement between both versions, regardless of V01 using the simple panel model and limited knowledge of the thermo-optical properties of materials. The difference between V01 and V02 is $3\,\mathrm{nm\,s^{-2}}$ in the cross-track direction and smaller than $1\,\mathrm{nm\,s^{-2}}$ in the along-track and radial directions.

[2] https://ceres.larc.nasa.gov/data/#synoptic-toa-and-surface-fluxes-and-clouds-syn, accessed on 20/05/2025.

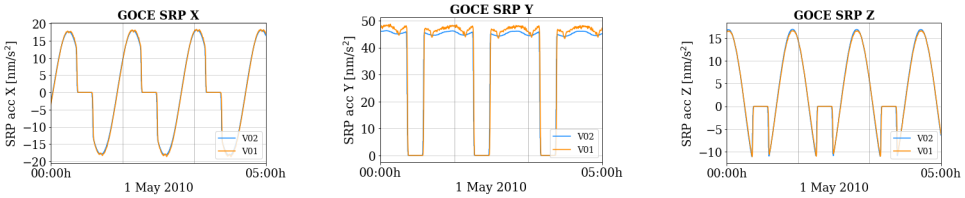

Figure 3.14: The comparison between the SRP acceleration used in Version V01 and V02. It should be noted that the V01 wind dataset also relies on the SRP torques in addition to the linear accelerations.

3

Figure 3.15.a shows the difference in the crosswinds between the newly produced version V02 and the version V01. At the beginning of the mission, version V02 winds have a lower magnitude in comparison to V01, evident from negative differences. Considering the difference in the SRP magnitude between both versions (Fig. 3.14), the decrease of the wind in the first year is likely due to the introduction of the thermal emission acceleration. We interpret this as an improvement, assuming that smaller crosswinds are likely more accurate. As the density increases over time (Fig. 3.15.c), the wind difference changes sign, meaning that V01 crosswinds have a smaller magnitude than V02. This could be attributed to errors in the aerodynamic modelling (manifesting at higher densities) as well as differences between the algorithms used to produce both versions. Therefore, the wind retrieval algorithm used to generate V01 (T. Visser et al., 2019) should be revised and updated to incorporate recent improvements.

While the wind retrieval algorithm relies on the cross-track acceleration, the thermosphere density is derived from the along-track aerodynamic acceleration (Eq. 3.2). The ratio of radiative forces to the aerodynamic force in the along-track direction is much smaller than in the cross-track direction (see Fig. 3.3). Therefore, the improvement in the radiation pressure modelling is best reflected in the crosswind rather than in the density. Figure 3.15.b shows the relative density difference towards V01. The overall differences are very small, with the biggest impact (up to 7%) visible around the eclipse regions during 2010/2011 when the solar activity was low. The features highlighted by dashed lines are caused by high-frequency thrust noise, a real acceleration signal. Since the L1b thruster data has a lower sampling rate than the raw telemetry, the feature is either smoothed out or aliased in the former (the details of the L1b thruster data processing are unknown to us). Hence, it appears as high-frequency noise in the density difference. The new GOCE dataset includes a flag indicating when density data is affected by thruster noise.

Finally, since a comparison of the GOCE densities to other datasets is out of the scope of this paper, we refer to Bruinsma (2014) for such a comparison.

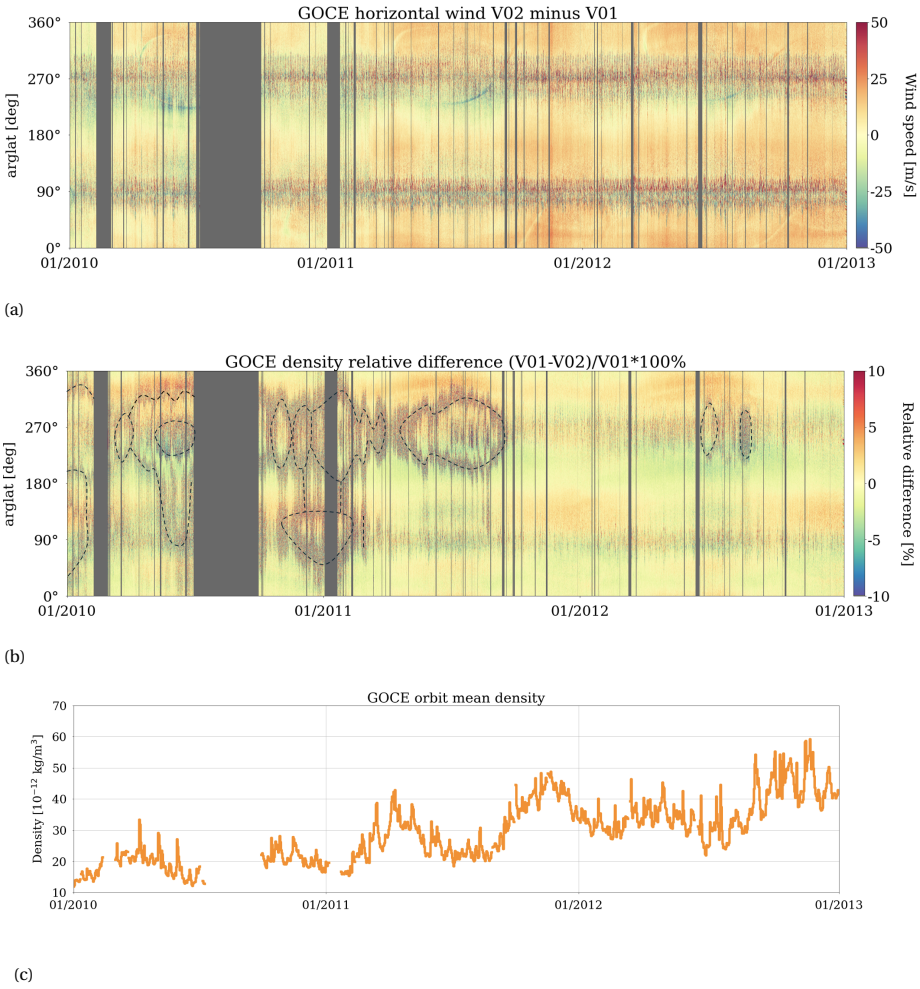

Figure 3.15: Evolution of the GOCE orbit mean density and the differences between versions V01 and V02 of the neutral thermosphere density and horizontal wind.

The thermospheric wind pattern depends, among others, on the season of the year, local solar time, and geomagnetic conditions (W. Wang et al., 2021). Due to a very small orbital precession, GOCE's local time remained roughly fixed throughout the mission. The ascending equatorial crossing of the satellite drifted from 18:00 local time at the beginning of the mission to 19:30 local time at the end (Bock et al., 2014). This orbital characteristic provided a perfect opportunity to study seasonal and annual variations in the wind data. As a result of its near-polar orbit, the winds are closely aligned with the zonal direction at low and mid-latitudes and with the meridional direction at the poles, which is illustrated in Figure 3.16. The seasonal dependency is clearly visible in the zonal winds, with a cyclical pattern that repeats throughout the mission.

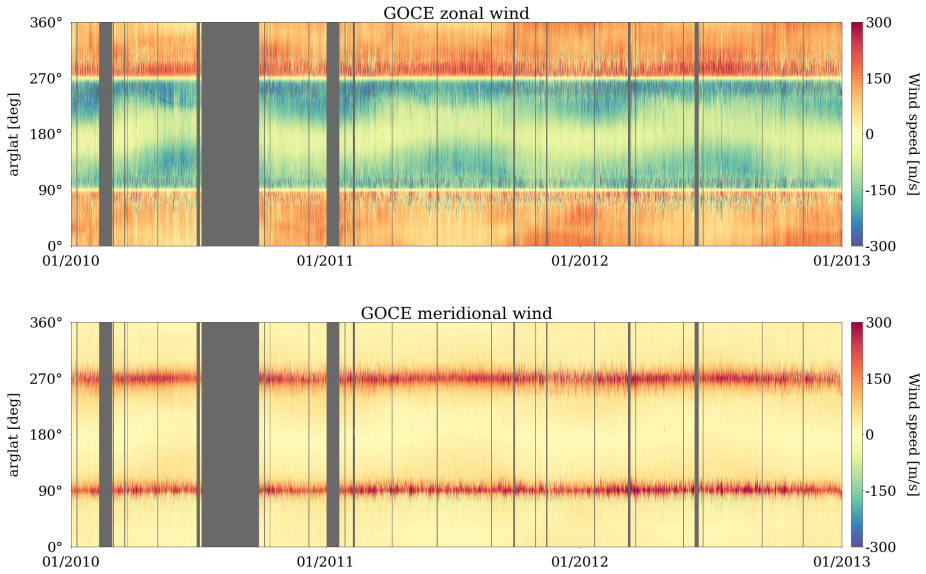

Figure 3.16: Distinction between GOCE zonal and meridional winds V02. The seasonal wind pattern repeating through the year is clearly visible in the zonal winds.

The study performed by M. Dhadly et al. (2017) and M. S. Dhadly et al. (2018) showed that there is an offset between the accelerometer-derived GOCE zonal wind data and the models. The study compared the GOCE data with various ground-based and space-based datasets, including Fabry-Perot interferometers, Scanning Doppler imaging Fabry-Perot interferometers, as well as space-based instruments flying on the Upper Atmosphere Research Satellite and Dynamic Explorer 2. The study concluded that amongst all these datasets, the GOCE in-situ crosswind data have been overestimated, with the differences. This offset increases with latitude and is particularly noticeable on the duskside. It should be noted that the authors' comparison did not yet include Version V01 but relied on an even older version of the dataset. Nevertheless, we can use this information to quantify the improvement in the new wind data.

To verify this assumption, we divided the zonal wind data in the dusk and dawn sectors and binned with a resolution of 1° magnetic latitude (MLAT). Then we calculated the median absolute deviation (MAD) of each bin. Figure 3.17 shows the comparison between the V01 and V02 data. At low latitudes, the wind distribution is similar for both versions in both the dusk and dawn sectors. In the South Pole region (approximately $-80°$ to $-70°$ MLAT), there is a decrease of wind MAD of approximately $10\,\mathrm{m\,s^{-1}}$ for the dawn sector. Around the North Pole (70°–80° MLAT), the MAD decreases on the dusk side, but it slightly increases on the dawn side. These variations in MAD may be linked to eclipse transitions occurring at these latitudes, which are affected by the updated thermal emission modeling.

We can also assess the data quality by checking the consistency of zonal wind data. To do so, first, we divided the dataset into three yearly bins: 2010, 2011 and 2012. In the next

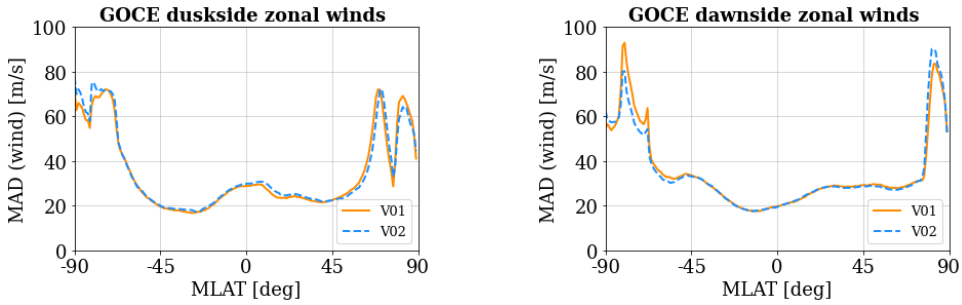

Figure 3.17: Median absolute deviation (MAD) of GOCE zonal winds with 1° MLAT binning.

step, we split the data into the dusk and dawn sectors and limited it to the low latitudes (argument of latitudes $0° \pm 45°$ and $180° \pm 45°$) to prevent the complex wind dynamics at the poles from affecting the statistics. To calculate data consistency, we subtracted the wind from the consecutive years and calculated the MAD. Table 3.5 shows the MAD comparison between Version V01 and V02. The wind consistency is similar between both versions, with a slight enhancement of V02 in the dawn sector, especially for the 2010-2011 bin. This indicates that even though the magnitude of the total wind speed differs between both versions (Fig. 3.15.a), the consistency between the zonal component of the low-latitude winds is similar.

Table 3.5: Comparison between Version v01 and v02 wind consistency.

Years	**Time**	**V01 MAD [m/s]**	**V02 MAD [m/s]**
2010–2011	Dawn	25.20	24.72
	Dusk	24.02	23.92
2011–2012	Dawn	20.51	20.25
	Dusk	20.67	20.66

To produce the Version V02 dataset, we used the energy accommodation coefficient of 0.82. This is in line with the study by March, Visser, et al. (2019), who optimised the gas-surface interaction DRIA (Diffuse Reflection Incomplete Accommodation) model by investigating the consistency of the GOCE winds. After implementing the radiation pressure improvements, we verified whether this assumption was still valid.

Figure 3.18 shows the zonal component of GOCE wind data produced for the energy accommodation coefficients ranging between 0.5 and 1.0. We followed a similar approach as explained in the previous analysis, starting by arranging the dataset into three yearly bins. By dividing the data into years instead of seasons (as proposed by March, Visser, et al. (2019)), we captured the seasonal wind variations while mitigating the effect of prolonged data gaps (such as the one occurring in July 2010). Likewise, in the previous analysis, we restricted the data selection to low-latitude and divided it

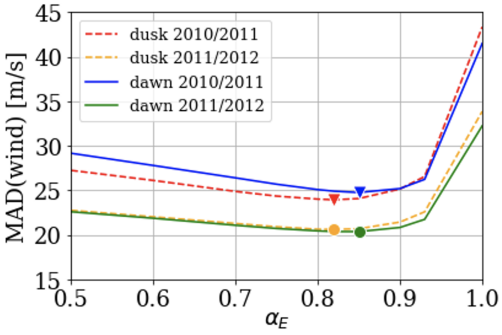

Figure 3.18: Median absolute deviation of the Version v02 GOCE zonal wind, restricted to the argument of latitude $0° \pm 45°$ and $180° \pm 45°$, as a function of energy accommodation coefficient.

into dawn and dusk sectors. To calculate the data consistency, we subtracted the wind from the consecutive years and calculated MAD. The markers pinpoint the minimum MAD for each curve. The optimum energy accommodation coefficients are $\alpha_E = 0.82$ and $\alpha_E = 0.85$ for the dusk and dawn sectors, respectively, with the best estimate for the energy accommodation coefficient lying between these values. Therefore, we conclude that introducing the new radiation pressure model did not notably change the assumptions on the energy accommodation coefficient.

3.5. SUMMARY AND OUTLOOK

The aim of this study was to revisit and reprocess the GOCE horizontal wind data using enhanced force modelling standards. The key improvement was the introduction of the thermal emission acceleration, which has never been accounted for in the previous GOCE datasets. Moreover, this study has advanced the solar radiation pressure modelling, including updating the thermo-optical surface coefficients and using a ray-tracing method. We collected and presented information on the GOCE surface materials relevant for radiation pressure modelling, including the GOCE panel model, from multiple sources. The information on the surface materials can be readily reused in the context of other missions. For a more realistic model, the solar flux was split between two wavelengths: visible and infrared. The ion thruster Level-1b data were replaced by raw telemetry filling multiple data gaps. Furthermore, this research served as an opportunity to compare the new dataset with the previously published one, evaluating wind consistency and magnitude, as well as verifying the assumptions about the energy accommodation coefficient.

We took advantage of thermistor data located on the Sun-opposed side of the satellite wing to realistically model the heat transfer and the wing surface temperature. However, since the other thermistors were placed on the rear side of the panels, a direct evaluation of surface temperature was not possible. Similar limitation was encountered for the GRACE mission (Hładczuk et al., 2024). Therefore, it would be beneficial from the per-

spective of thermal modelling to equip future missions with thermistors placed on the top of the panels and distributed externally in multiple places.

Modelling the wavelength-dependent solar flux interaction with the satellite requires detailed knowledge of the material properties. Due to GOCE's low orbit, the degradation caused by the atomic oxygen results in erosion of the coating materials (Battaglia et al., 2008). Moreover, the surface properties of the satellites are affected by factors such as UV radiation exposure (Silverman, 1995). Addressing these factors would require an extensive study with a focus on laboratory testing. Therefore, some assumptions had to be made to ensure a compromise between model accuracy and simplicity. While accounting for the infrared part of the solar spectrum is crucial for applications which require precise force modelling, other missions with limited knowledge of surface properties may not significantly benefit from this distinction.

The solar flux varies not only in wavelength but also in magnitude. However, these variations are relatively minor. In this study, we did not account for the temporal variations in solar flux, which could be a point for future analysis. Future studies would also benefit from introducing Clouds and Earth's Radiant Energy System (CERES) data to improve vertical wind estimate as well as wind uncertainty quantification, similar to the one available for the density data (Siemes et al., 2024). Both of these aspects will be addressed in our future work.

ACKNOWLEDGMENTS

The authors would like to thank AIRBUS GmbH, and specifically Hauke Thamm, for kindly sharing the 'GOCE Solar Array: Detailed Thermal Model Analysis' document. We also extend our thanks to Tim Visser for sharing data and offering valuable insights on GOCE wind version V01.

4

THERMOSPHERE DENSITY AND CROSSWIND UNCERTAINTY PROPAGATION - SENSITIVITY ANALYSIS

N.A. Hładczuk, C. Siemes, P.N.A.M. Visser

Accurate knowledge of the neutral thermosphere mass density and crosswind is essential for constructing empirical models used in space operations. A well-established technique to model thermosphere density and crosswind is to use in-situ measurements from accelerometers onboard Low Earth Orbit (LEO) satellites, combined with precise GNSS positioning. Assimilating in-situ data into the empirical models can be challenging, due to potential error sources arising from different ground- and space-based measurement techniques, which vary in coverage and resolution. Moreover, it has been proven that the thermosphere density datasets may differ by up to 30%, even when derived from the same instrument at the same altitude. Therefore, quantifying uncertainty in wind and density datasets is invaluable for addressing these challenges. Recently, a method was developed to propagate various error sources and quantify their impact on thermosphere density derived from the accelerometer and GNSS tracking data. In this chapter, we extend the existing method by introducing the error propagation into the crosswind data besides the thermosphere density. Moreover, we performed a sensitivity analysis using the example of GRACE-B wind and density data to identify which input parameters have a significant impact on the output uncertainty. We found that the density uncertainty during high solar activity, which ranged between 4 % *to* 4.5 % *of the density signal, was mainly caused by*

parameters related to aerodynamic modelling, in particular uncertainties in the thermosphere temperature and the energy accommodation coefficient. During low solar activity, the density errors were between 5 % *to* 18 %*, with the dominant contribution arising from the radiation pressure modelling. For the crosswind during high solar activity, the uncertainty ranged from* $30\,\mathrm{m\,s^{-1}}$ *to* $110\,\mathrm{m\,s^{-1}}$*, and mainly originated from the radiation pressure modelling. The analysis was particularly useful for assessing the crosswind uncertainty during the low solar activity, when the weak aerodynamic signal leads to large wind errors, ranging from* $200\,\mathrm{m\,s^{-1}}$ *to* $550\,\mathrm{m\,s^{-1}}$*. Among the parameters related to radiation pressure modelling, the biggest impact on the uncertainty stemmed from the heat capacity of the satellite panels and the reflection coefficients for visible and infrared light.*

4.1. INTRODUCTION

The characteristics of neutral thermospheric wind and density play an important role in understanding the coupling between Earth's thermosphere and ionosphere, and in improving models used in space operations. These models are crucial for a variety of applications, including determining a mission's lifespan, estimating fuel requirements, and assessing collision risk, among others. Moreover, high-resolution wind and density data can also be used to validate other datasets, study thermospheric dynamics, and investigate the response of the upper atmosphere to geomagnetic activity.

Current capabilities to model thermosphere density and winds can be broadly divided into two classes of models: physics-based and empirical. Physics-based models, such as TIE-GCM (Peymirat, 1998) or WACCM (Liu et al., 2010), rely on first-principle physics equations to describe the thermosphere dynamics. Empirical models, on the other hand, are based on ground- and space-based observations fitted to mathematical equations. For thermosphere density, the most commonly used empirical models include NRLMSISE-00 (Picone et al., 2002), together with its reformulated versions: NRLMSIS 2.0 (Emmert et al., 2021), and NRLMSIS 2.1, which additionally introduces nitric oxide (NO) number density (Emmert et al., 2022); Jacchia-Bowman (Bowman et al., 2008); as well as DTM-2020 (Bruinsma, 2014). In the case of the thermosphere wind, the most common model is the Horizontal Wind Model (HWM) (Drob et al., 2008; Drob et al., 2015)), which is based on incoherent scatter radar, Fabry–Perot interferometer, as well as rocket and satellite measurements. Thermosphere density and wind can also be derived from in situ data of Low Earth Orbit (LEO) satellites carrying accelerometers, such as CHAMP, GOCE, GRACE, GRACE-FO, and Swarm (Bruinsma & Biancale, 2003; Hładczuk et al., 2025; Siemes et al., 2023). Moreover, the potential of using GNSS tracking data to derive in situ thermospheric density has been investigated by van den IJssel et al. (2020).

Considering the multitude of existing wind and density models, challenges may arise when assimilating ground- and space-based data into the existing datasets. For example, while assimilating data into the High-Latitude Thermospheric Wind Model (HL-TWiM), biases in the GOCE cross-track wind measurements were identified and corrected (M. S. Dhadly et al., 2019). Similarly, the comparison between various datasets can be challenging. The study by Bruinsma et al. (2022) revealed that the thermospheric density products may differ by up to 30%, even when derived from the same instrument at the same altitude. In another study by Mehta et al. (2023), the authors reported that depending on the method used for the drag coefficient modelling, the density estimates may differ by tens of percent in some cases.

Such challenges in the context of data assimilation and model comparison could be tackled by augmenting existing wind and density datasets with information regarding the dataset uncertainty.

It is observed that the differences in the modeled drag coefficients and hence the derived density estimates are tens of percent in some cases. Thus, data users (e.g. modelers) should be careful when using datasets for scientific investigations, particularly when combining data sets from different sources or spanning a wide range of altitudes and solar activity levels.

Quantifying observational uncertainty is a complex task due to the number and diversity of error sources, starting from uncertainties in the satellite specification, such

as geometry and thermo-optical properties, as well as errors in the accelerometer and GNSS measurements. Wind and density retrieval rely on the aerodynamic force, which depends on many parameters, including, e.g. atmospheric composition and temperature. Unfortunately, there is currently no mission capable of providing in-situ measurements of these variables; therefore, we rely on modelled values of limited accuracy.

Recently published density and wind datasets derived from in situ satellite observations do not include uncertainty information. The only exception known to us is the GOCE dataset. The authors of the dataset identified six categories of errors that contribute to the overall wind and density uncertainty: the along-track, cross-track, and radial components of acceleration, thruster actuation errors, radiation pressure modelling errors, and uncertainty in the wind model (E. Doornbos et al., 2014). However, in this case, the contribution of individual parameters (e.g. in radiation pressure modelling) has not been thoroughly scrutinised. The study by Bruinsma and Biancale (2003) focused on quantifying the uncertainty in CHAMP data, considering factors such as accelerometer calibration parameters, aerodynamic coefficient modelling, and geomagnetic activity as potential error sources. However, in this analysis, uncertainties related to the e.g. reflection coefficient were not explicitly included in the error budget.

Recently, a method was developed to propagate various error sources and quantify their impact on thermosphere density derived from the accelerometer and GNSS tracking data (Siemes et al., 2024). The method considered the uncertainty in all input parameters in the derivation of the density and propagated that uncertainty to the density observations. The method has been demonstrated based on a few datasets from the GRACE-B satellite.

The uncertainty of in situ vertical wind data was investigated in an early study using the Neutral Atmosphere Temperature Experiment (NATE) onboard the Atmosphere Explorer-C satellite (Spencer et al., 1976). That work identified and analysed five main sources of error affecting the vertical wind measurements obtained by the NATE instrument. In a related study, T. Visser et al. (2019) proposed an algorithm that combines linear and angular acceleration measurements to derive thermospheric winds. By comparing two independently derived wind data sets, the study quantified the uncertainty in accelerometer-derived wind observations. The accompanying sensitivity analysis demonstrated that continuous thrusting and the magnetic properties of the satellite are major contributors to the uncertainty in torque-derived wind estimates. The study underlines the need for rigorous uncertainty quantification for a better understanding of the quality of derived wind.

In this chapter, we extend the previously mentioned density uncertainty quantification method proposed by Siemes et al. (2024) to also quantify the uncertainty of crosswind observations. We also introduce a new source of uncertainty: the efficiency of the satellite solar arrays, alongside the existing ones (Siemes et al., 2024). We focus on accelerometer-derived wind and density from the GRACE-B satellite to perform a sensitivity analysis. Our goal is to identify which input parameters have a significant impact on the uncertainty of density and crosswind. Knowing the driving error sources is crucial for selecting appropriate input uncertainty values and, finally, for supplementing wind and density data with error information.

The structure of this chapter is organised as follows: Section 4.2 briefly introduces

the wind and density derivation algorithms, and explains the methodology behind the radiation pressure modelling, aerodynamic modelling, and the uncertainty propagation. In Section 4.3, we discuss the input data. Section 4.4 elaborates on the results of the sensitivity analysis. Last but not least, Section 4.5 provides conclusions and an outlook on future work.

4.2. METHODOLOGY

4.2.1. DENSITY DERIVATION ALGORITHM

In this analysis, we focused on the thermosphere density and wind data derived from the accelerometer measurements. This choice is motivated by the fact that the thermosphere wind can only be obtained using the accelerometer data. Nevertheless, for the thermosphere density, it is also possible to retrieve it using the GNSS tracking. This technique, however, results in a much lower temporal resolution. More information on the density uncertainty propagation from tracking data can be found in Siemes et al. (2024).

For satellites where the centre of mass coincides with the accelerometer location, the density can be derived from the aerodynamic acceleration (E. Doornbos, 2011). To achieve this, the first step is to calibrate the acceleration measured by the accelerometer, $\boldsymbol{a}_{\text{meas}}$, by applying the scale factor matrix $\boldsymbol{S}$ and the bias vector $\boldsymbol{b}$ to arrive at the calibrated acceleration $\boldsymbol{a}_{\text{cal}}$:

$$\boldsymbol{a}_{\text{cal}} = \boldsymbol{S}\,\boldsymbol{a}_{\text{meas}} + \boldsymbol{b} \tag{4.1}$$

In the next step, the radiation pressure forces, $\boldsymbol{a}_{\text{rp}}$, are being modelled. These consist of solar radiation pressure $\boldsymbol{a}_{\text{srp}}$, Earth albedo, $\boldsymbol{a}_{\text{alb}}$, Earth infrared radiation, $\boldsymbol{a}_{\text{ir}}$, and thermal emission, $\boldsymbol{a}_{\text{rp}}$.

The total radiation pressure acceleration is the sum

$$\boldsymbol{a}_{\text{rp}} = \boldsymbol{a}_{\text{srp}} + \boldsymbol{a}_{\text{ir}} + \boldsymbol{a}_{\text{alb}} + \boldsymbol{a}_{\text{the}}. \tag{4.2}$$

Finally, the observed aerodynamic acceleration can be obtained by subtracting the radiation forces from the calibrated acceleration calculated in the previous step

$$\boldsymbol{a}_{\text{aero,obs}} = \boldsymbol{a}_{\text{cal}} - \boldsymbol{a}_{\text{rp}}. \tag{4.3}$$

The thermosphere density is then derived from the aerodynamic acceleration as

$$\rho = \frac{2\,m\,\boldsymbol{a}_{\text{aero,obs}} \cdot \hat{\boldsymbol{e}}}{|\boldsymbol{v}_{\text{r}}|^2\,\boldsymbol{C}_{\text{aero}} \cdot \hat{\boldsymbol{e}}}, \tag{4.4}$$

where m denotes the satellite mass, $\boldsymbol{C}_{\text{aero}}$ is the aerodynamic coefficient vector, inherently multiplied by the cross-section area, and $\boldsymbol{v}_{\text{r}}$ is the satellite velocity relative to the atmosphere. The details on modelling the aerodynamic coefficient are described in Section 4.2.4. Note that the density is obtained by projecting the aerodynamic acceleration as well as the aerodynamic coefficient vector onto the direction specified by the unit vector $\hat{\boldsymbol{e}}$. For this study, we select $\hat{\boldsymbol{e}}$ to be aligned with the accelerometer x-axis, which, in our case, is closely aligned with the flight direction, in which the drag acceleration is most prominent.

The relative velocity vector $\boldsymbol{v}_r$ is composed of several contributions:

$$\boldsymbol{v}_r = \boldsymbol{v}_{sat} + \boldsymbol{\omega}_\oplus \times \boldsymbol{r}_{sat} + (\boldsymbol{v}_{wind} \cdot \hat{\boldsymbol{e}})\,\hat{\boldsymbol{e}}, \tag{4.5}$$

where $\boldsymbol{r}_{sat}$ and $\boldsymbol{v}_{sat}$ are the satellite's position and velocity, respectively. The terms $\boldsymbol{\omega}_\oplus \times \boldsymbol{r}_{sat}$ and $(\boldsymbol{v}_{wind} \cdot \hat{\boldsymbol{e}})\,\hat{\boldsymbol{e}}$ represent the velocity of Earth's corotating atmosphere and the wind in the direction of vector $\hat{\boldsymbol{e}}$, respectively, where $\boldsymbol{\omega}_\oplus$ is Earth's angular velocity vector. Since vector $\hat{\boldsymbol{e}}$ is approximately aligned with the flight direction, the second term reflects the in-track wind.

4.2.2. WIND DERIVATION ALGORITHM

4

To derive the wind uncertainty, we rely on the direct, dual-axis algorithm proposed by Sutton et al. (2007), which we implemented as described by E. Doornbos et al. (2010). In the first step of the direct algorithm, the modelled aerodynamic acceleration $\boldsymbol{a}_{aero,mod}$ is obtained from

$$\boldsymbol{a}_{aero,mod} = \frac{\rho\,|\boldsymbol{v}_r|^2}{2\,m}\boldsymbol{C}_{aero}, \tag{4.6}$$

where input density ρ is calculated on the basis of the NRLMSISE-00 model. The choice of using a model rather than observations for density is motivated by the fact that it avoids any issues due to accelerometer noise combined with a low signal-to-noise ratio.

The modelled acceleration can then be split according to

$$\boldsymbol{a}_{aero,mod} = \boldsymbol{a}_{aero,mod,drag} + \boldsymbol{a}_{aero,mod,lift}, \tag{4.7}$$

where $\boldsymbol{a}_{aero,mod,drag}$ is the drag component and $\boldsymbol{a}_{aero,mod,lift}$ combines the remaining lift and side force. The two components are defined by

$$\boldsymbol{a}_{aero,mod,drag} = \left(\boldsymbol{a}_{aero,mod} \cdot \hat{\boldsymbol{v}}_r\right)\hat{\boldsymbol{v}}_r, \tag{4.8}$$

and

$$\boldsymbol{a}_{aero,mod,lift} = \boldsymbol{a}_{aero,mod} - \boldsymbol{a}_{aero,mod,drag}, \tag{4.9}$$

with unit vector

$$\hat{\boldsymbol{v}}_r = \frac{\boldsymbol{v}_r}{|\boldsymbol{v}_r|} \tag{4.10}$$

pointing in the direction of the relative velocity vector.

Next, we can remove the combined lift and side force effects from the observed acceleration $\boldsymbol{a}_{aero,obs}$ to arrive at the observed drag acceleration

$$\boldsymbol{a}_{aero,obs,drag} = \boldsymbol{a}_{aero,obs} - \boldsymbol{a}_{aero,mod,lift}. \tag{4.11}$$

In the direct wind estimation algorithm, the crosswind is obtained from the geometrical consideration presented in Figure 4.1. In the absence of crosswind, the observed drag acceleration $\boldsymbol{a}_{aero,obs,drag}$ should perfectly align with the relative velocity vector $\boldsymbol{v}_r$. However, in the presence of crosswind, it slightly deviates from that direction.

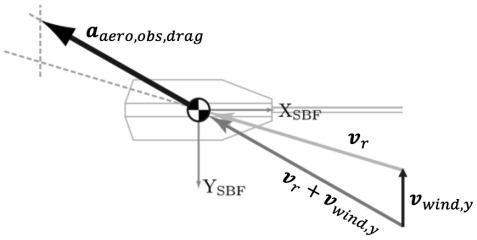

Figure 4.1: Schematic top view of the satellite illustrating the observed drag acceleration, $\boldsymbol{a}_{\text{aero,obs,drag}}$. Vector $\boldsymbol{v}_{\text{r}}$ refers to the relative velocity, which does not account for crosswind. In the presence of crosswind $\boldsymbol{v}_{\text{wind},y}$, the observed acceleration is not aligned with the relative velocity (dashed line). Credits: E. Doornbos et al. (2010).

Since the drag acceleration is by definition in the direction of the relative velocity, we obtain the crosswind $v_{\text{wind,y}}$ by adjusting the relative velocity vector such that it aligns with the observed drag acceleration. Thus, from geometrical interpretation of Figure 4.1 we obtain

$$v_{\text{wind,y}} = \frac{a_{\text{aero,obs,drag,y}}}{a_{\text{aero,obs,drag,x}}} v_{\text{r,x}} - v_{\text{r,y}}. \tag{4.12}$$

4.2.3. RADIATION PRESSURE MODELLING

In the context of uncertainty quantification, we represent the satellite geometry by a panel model to limit the computational effort to reasonable levels. The radiation pressure modelling consists of multiple components as described by Equation (4.2), of which the direct solar radiation, albedo, and Earth infrared radiation components are external to the satellite. To calculate the radiation pressure of such external radiation sources, we use the formula

$$\boldsymbol{a}_{\text{ext},u} = \begin{cases} -\frac{P_{\text{ext},u}}{m} A_n \cos\theta \left((c_{\text{a},u,j} + c_{\text{d},u,j}) \boldsymbol{e}_{\text{ext}} + \left(\frac{2}{3} c_{\text{d},u,j} + 2 c_{\text{s},u,j} \cos\theta \right) \boldsymbol{e}_n \right), & \cos\theta > 0 \\ \mathbf{0}, & \cos\theta <= 0 \end{cases} \tag{4.13}$$

where the unit vectors $\mathbf{e}_n$ and $\mathbf{e}_{\text{ext}}$ denote the outward normal of the n-th panel and the direction from the satellite to the external source, respectively, A_n is the panel area, $P_{\text{ext},u}$ is the radiation pressure associated with wavelength u (infrared or visible), and m is the satellite mass (E. Doornbos, 2011). The angle θ can be inferred from

$$\cos\theta = \boldsymbol{e}_{\text{ext}} \cdot \boldsymbol{e}_n. \tag{4.14}$$

Within the uncertainty propagator, the panels of the satellite geometry are augmented with material properties, where several panels may have the same material. Hence, we use index n for the panels, index j for the materials, and a lookup table to relate the materials to the panels. Each material is characterised by its thermo-optical surface parameters, including the absorption coefficient ($c_{\text{a},u,j}$) and the reflection coefficients, which are divided into specular ($c_{\text{s},u,j}$) and diffuse ($c_{\text{d},u,j}$) components. As before, the subscript u indicates either visible or infrared wavelength.

Further, P_{ext} is an external radiation pressure source such as the Sun (solar radiation pressure) or the Earth (infrared radiation and albedo). For the direct radiation pressure

from the Sun, it encloses

$$P_{\text{srp}}(\lambda) = \left(\frac{1\text{AU}}{|\boldsymbol{r}_{\text{sat}} - \boldsymbol{r}_{\text{Sun}}|}\right)^2 P_{1\text{AU}}(\lambda), \tag{4.15}$$

where $|\boldsymbol{r}_{\text{sat}} - \boldsymbol{r}_{\text{Sun}}|$ is the distance from the Sun to the satellite and $P_{1\text{AU}}$ is the solar radiation pressure at one astronomical unit (AU), calculated as the ratio of the solar constant $\Phi = 1367\,\text{W}\,\text{m}^{-2}$ and the speed of light c, i.e. $P_{1\text{AU}} = \Phi/c = 4.56\,\mu\text{N}\,\text{m}^{-2}$.

In this work, we distinguish between visible and infrared radiation from the Sun and assume that the total flux is evenly distributed between the visible and infrared bands (Hładczuk et al., 2025). The details on calculating albedo and infrared radiation fluxes are provided in Siemes et al. (2024).

As for the radiation pressure from external sources, we use the satellite panel geometry to model the heat exchange between the satellite and its environment. The details of the thermal emission modelling method are elaborated in Siemes et al. (2023) and Hładczuk et al. (2024). In brief, in the proposed model each panel n heats up at a rate of $\dot{Q}_{\text{abs},n}$ by absorbing radiation, cools down at a rate of $\dot{Q}_{\text{emit},n}$ by emitting radiation, and exchanges heat with the satellite body at a rate of $\dot{Q}_{\text{cond},n}$.

Thus, the rate at which the heat of a panel changes is

$$\dot{Q}_n = (1 - e_n)\,\dot{Q}_{\text{abs},n} - \dot{Q}_{\text{emit},n} - \dot{Q}_{\text{cond},n}, \tag{4.16}$$

where e_n represents the efficiency of the solar array (Hładczuk et al., 2024; Y. Wang et al., 2023). If the panel is not a solar array, e_n is zero.

The rate of the heat change of the satellite body, $\dot{Q}_{\text{body}}$, is defined as

$$\dot{Q}_{\text{body}} = \dot{Q}_{\text{gen}} + \sum_n \dot{Q}_{\text{cond},n}, \tag{4.17}$$

where $\dot{Q}_{\text{gen}}$ denotes the heat generated internally by the satellite components.

After computing the heat change rates, we update the temperatures of the panels by

$$T_n(t + \Delta t) = T_n(t) + \frac{\dot{Q}_n}{C_n}\Delta t \tag{4.18}$$

and the satellite body by

$$T_{\text{body}}(t + \Delta t) = T_{\text{body}}(t) + \frac{\dot{Q}_{\text{body}}}{C_{\text{body}}}\Delta t, \tag{4.19}$$

where C_n and C_{body} are the thermal capacities of the panels and the satellite body, respectively, t is time, and Δt is the time step.

The thermal radiation pressure acceleration is then expressed as

$$\boldsymbol{a}_{\text{the}} = -\frac{2}{3}\sum_n \frac{\dot{Q}_{\text{emit},n}}{m\,c}\,\boldsymbol{e}_n, \tag{4.20}$$

where $\dot{Q}_{\text{emit},n}$ follows from the Stefan Boltzmann law

$$\dot{Q}_{\text{emit},n} = A_n c_{\text{a,ir},n} \sigma T_n^4. \tag{4.21}$$

Here, σ is the Stefan-Boltzmann constant, $c_{\text{a,ir},n}$ is the emissivity, and $\boldsymbol{e}_n$ denotes the outward normal vector of the panel.

4.2.4. AERODYNAMIC MODELLING

For the aerodynamic modelling, we followed the approach presented by Siemes et al. (2024), who employed the Diffuse Reflections with Incomplete Accommodation (DRIA) gas-surface interaction model, based on Sentman's equations for flat panels, in combination with a satellite panel model. The aerodynamic coefficient $\boldsymbol{C}_{\text{aero}}$ is a nonlinear function of multiple input parameters, i.e.

$$\boldsymbol{C}_{\text{aero}} = \boldsymbol{C}_{\text{aero}}\left(A_n, \boldsymbol{e}_n, T_n, \boldsymbol{v}_{\text{r}}, T_{\text{atm}}, \rho_c, \alpha_E\right), \tag{4.22}$$

where A_n denotes the area of the panel n with the normal $\boldsymbol{e}_n$, and the temperature T_n, $\boldsymbol{v}_{\text{r}}$ is the relative velocity vector, T_{atm} stands for the atmospheric temperature, the atmospheric composition is given by the mass density ρ_c per atmospheric constituent c, and the energy accommodation coefficient α_E. The equations for calculating the aerodynamic coefficient vector are provided in the PhD dissertation by E. Doornbos (2011)(Chapter 3.2).

4.2.5. UNCERTAINTY PROPAGATION

To give context to the uncertainty propagation, we must first define the GRACE satellites model (Table 4.1). For the satellite geometry, we utilised the panel model as defined by S. Bettadpur (2012), whereas for the thermal and optical surface properties, we use values provided by Siemes et al. (2023).

Table 4.1: GRACE panel model. A_n and $\boldsymbol{e}_n$ denote the area and normal vector of panel n, respectively. C_n is the heat capacity, and k_n is the thermal conductivity. The last six columns describe the infrared (subscript 'ir') and optical (subscript 'vis') surface coefficients of the specular (c_{s}), diffuse (c_{d}), and absorption (c_{a}) components. The heat capacity of the satellite body was set to $C_{\text{body}} = 1 \times 10^5\,\text{JK}^{-1}$, and the satellite's internal heat generation to $\dot{Q}_{\text{int}} = 70\,\text{W}$. The temperature used to initialise the thermal model is the same for all panels, and was set to $T_{n,0} = 300\,\text{K}$.

Panel	j (-)	A_n (m^2)	$e_{x,n}$ (-)	$e_{y,n}$ (-)	$e_{z,n}$ (-)	C_n (JK^{-1})	k_n (WK^{-1})	$c_{\text{s,ir},n}$ (-)	$c_{\text{d,ir},n}$ (-)	$c_{\text{a,ir},n}$ (-)	$c_{\text{s,vis},n}$ (-)	$c_{\text{d,vis},n}$ (-)	$c_{\text{a,vis},n}$ (-)
Front	1	0.955	1.0	0.0	0.0	1000.0	0.1	0.15	0.23	0.62	0.26	0.40	0.34
Rear	1	0.955	-1.0	0.0	0.0	1000.0	0.1	0.15	0.23	0.62	0.26	0.40	0.34
Starboard	2	3.155	0.0	0.766	-0.643	5000.0	0.1	0.16	0.03	0.81	0.30	0.05	0.65
Port	2	3.155	0.0	-0.766	-0.643	5000.0	0.1	0.16	0.03	0.81	0.30	0.05	0.65
Zenith	2	2.167	0.0	0.0	-1.0	5000.0	0.1	0.16	0.03	0.81	0.30	0.05	0.65
Nadir	3	6.071	0.0	0.0	1.0	10000.0	0.5	0.06	0.19	0.75	0.20	0.68	0.12

In the first step of the uncertainty propagation, we define the standard deviations of the model input parameters. Table 4.2 lists the values used in this study. The parameters were classified into the following groups:

- Aerodynamic modelling
- Relative velocity
- Satellite properties
- Radiation pressure modelling

- Thermal emission modelling
- Measurement noise

The following paragraph briefly summarises the selection of the uncertainty parameters. For a detailed explanation and the rationale behind defining these values, we refer the reader to Siemes et al. (2024). The definition of parameters related to the radiation pressure model and the spacecraft thermal model has been explained in 4.2.3. The group of parameters related to the aerodynamic model has been summarised in 4.2.4. The accelerometer measurement noise is set to the value of $1\,\mathrm{nm\,s^{-2}}$ (Flury et al., 2008), and the accuracy of the GNSS orbit tracking is assumed to be 1.2 cm in each direction. We also assumed that the position error in the cross-track direction is not correlated with the errors in the along-track and radial directions (where the along-track, cross-track, and radial directions are approximately aligned with the x, y, and z axes, respectively). However, the position errors in the along-tack and radial directions are highly correlated ($\rho_{\mathrm{diff},xz} = 0.9$) (van Helleputte et al., 2009). The temporal correlation of position, α, is accounted for by setting $\alpha = -0.4$. The period used for averaging the accelerometer bias has been set to $T_\mathrm{b} = 1$ day, and the sampling frequency of GNSS to $f_\mathrm{s} = 0.1\,\mathrm{Hz}$.

It is important to note that parameters from a specific group may overlap. For example, satellite mass or panel area may be used in both radiation pressure and aerodynamic modelling. Similarly, the panels' emissivity is used in both the radiation pressure and thermal emission models. For these parameters, the standard deviation remains the same regardless of the context. The standard deviations are defined as absolute values (e.g., satellite mass, initial body temperature) or as a fraction of the respective value (e.g., radiation fluxes). Additional information can be found in the manual accompanying the published propagation tool in the 4TU.ResearchData repository (Siemes, 2024).

Table 4.2: Uncertainty specification for the input parameters. Subscript k is the index of the epoch.

Parameter name	Standard deviation
Aerodynamic model	
Atmospheric temperature	$\sigma_{T_{\text{atm},k}} = 0.2 T_{\text{atm},k}$
Atmospheric mass density	$\sigma_{\rho_{c,k}} = 0.2 \rho_{c,k}$
Energy accommodation coefficient	$\sigma_{\alpha_E} = 0.05$
Relative velocity	$\sigma_{v_{\text{r},x}} = 50\,\text{m s}^{-1}$, $\sigma_{v_{\text{r},y}} = 50\,\text{m s}^{-1}$, $\sigma_{v_{\text{r},z}} = 10\,\text{m s}^{-1}$
Satellite	
Satellite mass	$\sigma_m = 2\,\text{kg}$
Panel area	$\sigma_{A_n} = 0.02 A_n$
Radiation pressure model	
Infrared surface coefficients	$\sigma_{c_{\text{s,ir},j}} = 0.1$, $\sigma_{c_{\text{d,ir},j}} = 0.1$, $\sigma_{c_{\text{a,ir},j}} = 0.1$
Visible surface coefficients	$\sigma_{c_{\text{s,vis},j}} = 0.1$, $\sigma_{c_{\text{d,vis},j}} = 0.1$, $\sigma_{c_{\text{a,vis},j}} = 0.1$
Earth albedo	$\sigma_{P_{\text{alb}}} = 0.1 P_{\text{alb},k}$
Earth infrared radiation	$\sigma_{P_{\text{ir}}} = 0.1 P_{\text{ir},k}$
Solar radiation	$\sigma_{P_{\text{srp}}} = 0.001 P_{\text{srp}}$
Thermal model	
Heat capacitance of panels	$\sigma_{C_n} = 0.2 C_n$
Heat capacitance of satellite body	$\sigma_{C_{\text{body}}} = 0.2 C_{\text{body}}$
Heat conductivity of panels	$\sigma_{k_n} = 0.2 k_n$
Internal heat generation	$\sigma_{\dot{Q}_{\text{int}}} = 0.2 \dot{Q}_{\text{int}}$
Solar panels efficiency	$\sigma_e = 0.1$
Initial panels' temperature	$\sigma_{T_{n,0}} = 10\,\text{K}$
Initial body temperature	$\sigma_{T_{\text{body},0}} = 20\,\text{K}$
Measurement noise	
Accelerometer measurement precision	$\sigma_{\text{acc,x}} = 1\,\text{nm s}^{-2}$, $\sigma_{\text{acc},y} = 1\,\text{nm s}^{-2}$, $\sigma_{\text{acc},z} = 1\,\text{nm s}^{-2}$
GNSS-tracking	$\sigma_{\text{pos},x} = 1.2\,\text{cm}$, $\sigma_{\text{pos},y} = 1.2\,\text{cm}$, $\sigma_{\text{pos},z} = 1.2\,\text{cm}$ $\rho_{\text{diff},xy} = 0$, $\rho_{\text{diff},xz} = 0.9$, $\rho_{\text{diff},yz} = 0$, $\alpha = -0.4$
Averaging for accelerometer bias	$T_{\text{b}} = 1$
Sampling frequency of GNSS tracking	$f_{\text{s}} = 0.1\,\text{Hz}$

After defining the standard deviations of the input parameters, we construct the input covariance matrix $\boldsymbol{\Sigma}_{\text{input}}$, which is constructed from the standard deviations and correlations of the previously defined parameters. Since the covariance matrix remains the same regardless of whether the method is applied to wind or density uncertainty, we may refer to Siemes et al. (2024) for more details. It should be noted that the input parameters remain uncorrelated, except for the GNSS-tracking noise.

In the second step, the density (cf. Eq. (4.4)) and crosswind (cf. Eq. (4.12)) are defined as non-linear functions

$$\rho(T_a, m_{sat}, \alpha_E, A_p, \ldots) \quad \text{and} \quad v_{\text{wind},y}(T_a, m_{sat}, \alpha_E, A_p, \ldots), \tag{4.23}$$

respectively, of the input parameters listed in Table 4.2.

Since the uncertainty propagation method treats the output uncertainty in density and wind, combined in vector $\boldsymbol{y} = \begin{bmatrix} \rho & v_{\text{wind},y} \end{bmatrix}^T$, as a linear relationship, i.e $\boldsymbol{y} = \boldsymbol{f}(\boldsymbol{x})$, where $\boldsymbol{x}$ is the input parameter vector, it must first be linearised. Therefore, the non-linear functions in Eq. (4.23) are expanded into a Taylor series

$$\boldsymbol{f}(\boldsymbol{x}) = \boldsymbol{f}(\boldsymbol{x}_0) + \boldsymbol{H}\Delta\boldsymbol{x} + \mathcal{O}(\Delta\boldsymbol{x}^2) \approx \boldsymbol{f}(\boldsymbol{x}_0) + \boldsymbol{H}\Delta\boldsymbol{x}, \tag{4.24}$$

where $\boldsymbol{x}_0$ is the Taylor point and $\Delta\boldsymbol{x} = \boldsymbol{x} - \boldsymbol{x}_0$. When the equation is evaluated close to the Taylor point, the higher order terms $\mathcal{O}(\Delta\boldsymbol{x}^2)$ of the Taylor series have a very small magnitude and can be truncated. Matrix

$$\boldsymbol{H} = \frac{\partial \boldsymbol{f}}{\partial \boldsymbol{x}}\bigg|_{\boldsymbol{x}=\boldsymbol{x}_0} = \begin{bmatrix} \frac{\partial \rho}{\partial \boldsymbol{x}} \\ \frac{\partial v_{\text{wind},y}}{\partial \boldsymbol{x}} \end{bmatrix} = \begin{bmatrix} \boldsymbol{H}_{\text{dens}} \\ \boldsymbol{H}_{\text{wind}} \end{bmatrix} \tag{4.25}$$

is the Jacobian matrix evaluated at the Taylor point.

Finally, we propagate the input covariance matrix $\boldsymbol{\Sigma}_{\text{input}}$ to the respective output covariance matrices.

$$\boldsymbol{\Sigma}_{\text{dens}} = \boldsymbol{H}_{\text{dens}}\, \boldsymbol{\Sigma}_{\text{input}}\, \boldsymbol{H}_{\text{dens}}^T, \tag{4.26}$$

$$\boldsymbol{\Sigma}_{\text{wind}} = \boldsymbol{H}_{\text{wind}}\, \boldsymbol{\Sigma}_{\text{input}}\, \boldsymbol{H}_{\text{wind}}^T. \tag{4.27}$$

As mentioned before, the input covariance matrix remains the same for both the thermosphere density and wind, and only the Jacobian matrices differ.

4.3. DATA SELECTION

For the following sensitivity analysis, we selected the Gravity Recovery and Climate Experiment (GRACE) mission. This choice is motivated by the fact that the GRACE satellite experienced a range of different environmental conditions, as explained in the following section, making it a perfect candidate for the uncertainty analysis. Moreover, the GRACE satellite has been selected as a use case by Siemes et al. (2024), which allowed us to rely on the uncertainty parameters proposed by them. The GRACE mission consists of twin satellites which operated in a near-circular and near-polar orbit at an altitude of approximately 480 km during the selected period from 2003 to 2012. In this study, we focused on one of the satellites, GRACE-B, which was arbitrarily chosen.

Figure 4.2 shows the crosswind data as a function of the argument of latitude (vertical axis) and time (horizontal axis). Each column depicts one orbital revolution, where 0° and 180° mark the ascending and descending equator crossings, respectively, 90° indicates the northernmost point of the orbit, 270° the southernmost point, and 360° marks the start of the next revolution. Figure 4.3 shows the orbit mean density as a time series, as well as 10.7 cm solar radio flux ($F_{10.7}$) during the operations of GRACE-B.

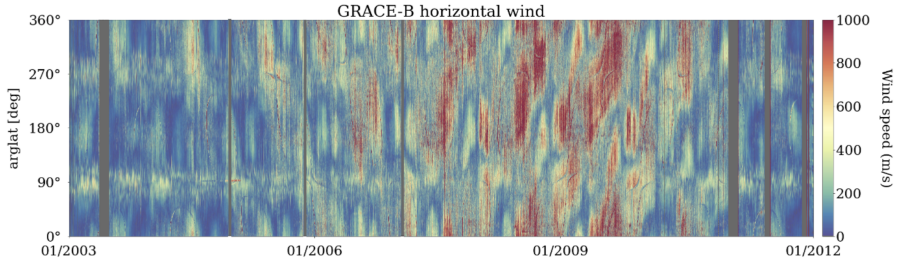

Figure 4.2: GRACE-B satellite windspeed.

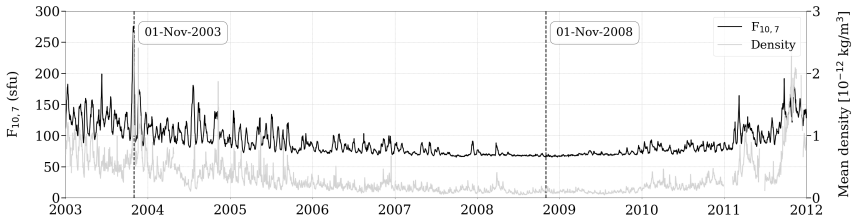

Figure 4.3: GRACE-B orbit mean density (grey) and solar radio flux at a wavelength of 10.7 cm ($F_{10.7}$) in solar flux units (sfu), where 1 sfu = 10^{-22} $Wm^{-2}Hz^{-1}$ (black). The vertical lines mark two periods selected for the analysis: 1st of Novemeber 2003 (high solar activity) and 1st of Novemebr 2008 (low solar activity).

For the sensitivity analysis, we selected two days (marked by the vertical dashed lines) corresponding to high solar activity (1-Nov-2003) and low solar activity (1-Nov-2008). These days represent two distinctly different environmental conditions, with a relatively small change in mission altitude (from ~500 km in November 2003 to ~470 km in November 2008). Figure 4.4 shows non-gravitational signals acting on the GRACE-B satellite. During the high solar activity, when the thermosphere density increases, the aerodynamic signal plays the most significant role. On the day selected within this study, the aerodynamic signal in the along-track direction was particularly strong (Fig. 4.4a) due to the high magnitude of the solar flux (Fig. 4.3). On the other hand, during the low solar activity, when the magnitude of the thermosphere density is smaller, aerodynamic acceleration was only approximately twice as large as the radiation pressure signal combined in the along-track direction and three times as large in the cross-track direction. Therefore, selecting these extreme cases for analysis allows us to cover the full range of signal ratios between aerodynamics and radiation pressure. Moreover, the Sun angle was 5° on November 1, 2008, which represents the most favourable case for the cross-wind retrieval since the radiation pressure and, thus, also the radiation pressure errors, are smallest. On 1 November 2003, the Sun angle was 55° degrees, enabling us to assess the effects of radiation pressure errors in the cross-track direction and their impact on the crosswind observations.

4.4. SENSITIVITY ANALYSIS: RESULTS

This section presents the results of the sensitivity analysis. First, we introduce the high-level parameters group consisting of uncertainties in the aerodynamic and radiation pressure modelling, measurement noise and relative velocity. Afterwards, we analyse each of the groups in more detail, focusing on the specific parameters driving the uncertainty.

4.4.1. HIGH-LEVEL PARAMETER GROUPS

The objectives of the uncertainty propagator are twofold: 1) to provide the uncertainty estimate for the neutral thermosphere density and wind data, and incorporate them into the disseminated version of the dataset available at TU Delft Thermosphere HTTPS Server[1] and 2) to provide the software tool for the scientific community. In this analysis,

[1] https://thermosphere.tudelft.nl/data/

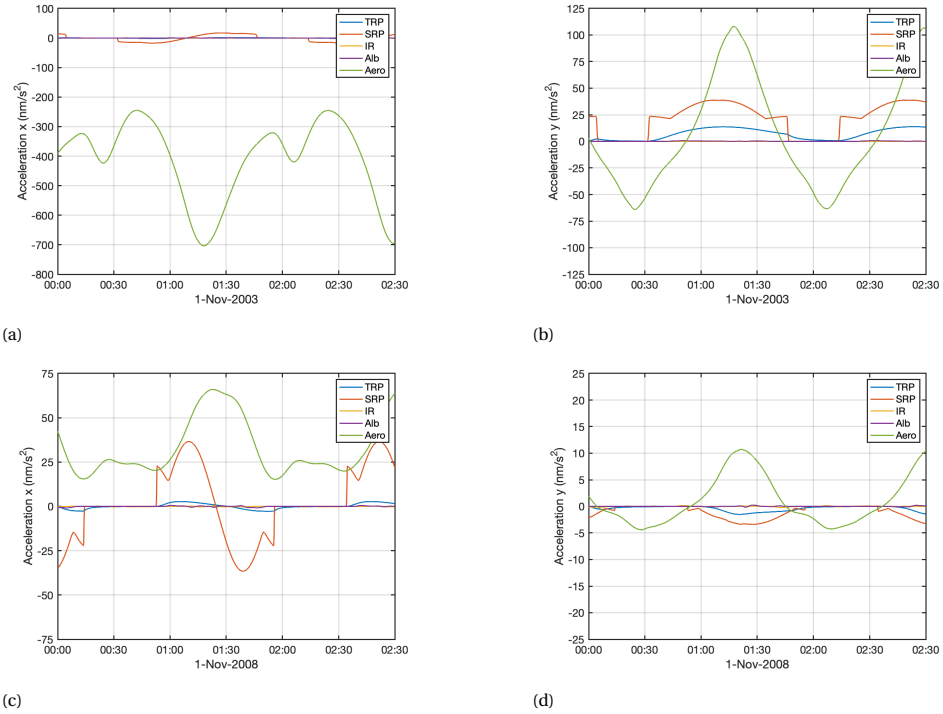

(a) (b)

(c) (d)

Figure 4.4: Non-gravitational forces acting on the GRACE-B satellite for 1-November-2003 (top) and 1-November-2008 (bottom). The left column shows the along-track component, and the right column shows the cross-track component. The acronyms stand for: Thermal Radiation Pressure (TRP), Solar Radiation Pressure (SRP), Earth's Albedo (Alb), Earth's Infrared radiation (IR), and aerodynamic acceleration (Aero).

we focused on the first objective. In order to quantify the uncertainties in the wind and density datasets, we must first set the input uncertainties to realistic values. Since the output uncertainty is a function of multiple inputs, it is crucial to first determine which parameters are driving the output uncertainty.

In the first step of the sensitivity analysis, four main groups of uncertainties were examined.

1. Parameters related to the aerodynamic model (aero),
2. Parameters related to the radiation pressure model (RP),
3. Parameters related to the measurement noise (measurement),
4. Uncertainty in the relative velocity ($\boldsymbol{v}_r$).

The initial values of the uncertainties (standard deviations) were set according to our current best knowledge, as described in Table 4.2. To perform the sensitivity analysis, i.e., to investigate how the input parameters from a particular group affect the output

uncertainty, it is necessary first to exclude the influence of other uncertainties. For example, to investigate the uncertainties in the aerodynamic parameters, the uncertainties associated with measurement noise and radiation pressure must be set to zero.

Since the uncertainties are assumed to be not correlated, with the exception of the position noise, the total uncertainty resulting from the sensitivity analysis is the sum of variances for independent quantities. Therefore, if the initial standard deviations change, it is possible to scale the resulting uncertainty accordingly.

The uncertainty in the density data has been thoroughly studied in Siemes et al. (2024). In this work, we extend the authors' analysis by providing a sensitivity study per parameter. Moreover, we also investigate the impact of the relative velocity uncertainty separately.

It should be noted that since the satellite velocity is much higher than the in-track wind, we do not account for the latter while calculating the thermosphere density (Eq. 4.5). This has no significant effect on defining the Taylor point during linearization. We do, however, account for the in-track wind uncertainty in the error propagation. Figure 4.5 shows the thermosphere density uncertainty as a percentage of the density signal, where the total error has been subdivided into the individual contributions. During the high solar activity period (1-Nov-2003), the total uncertainty of the density was between 4 % to 4.5 %, whereas during the low solar activity (1-Nov-2008) the uncertainty varied between 5 % to 18 %.The thermosphere density is proportional to the aerodynamic drag (Eq. 4.4), which is reflected in the uncertainty distribution. For high solar activity (Fig. 4.5a), aerodynamic forces in along-track direction dominate over the radiation pressure forces, making the former the main contributor to total error (Fig. 4.4a).

In contrast, during low solar activity (Fig. 4.5b), the aerodynamic signal in the along-track direction is relatively weak with respect to the radiation pressure (Fig. 4.4c), resulting in a much smaller contribution to the total error. Due to the low drag signal, the main uncertainty arises from the radiation pressure. The cyclic pattern in the radiation pressure uncertainty visible in the Figure 4.5b corresponds to the Sun–shadow transitions along the orbit, indicated by a grey background. Additionally, the measurement noise, combining the accelerometer noise and the position noise, also plays a role during the eclipse passes. This can be explained by the lower signal-to-noise ratio in this part of the orbit.

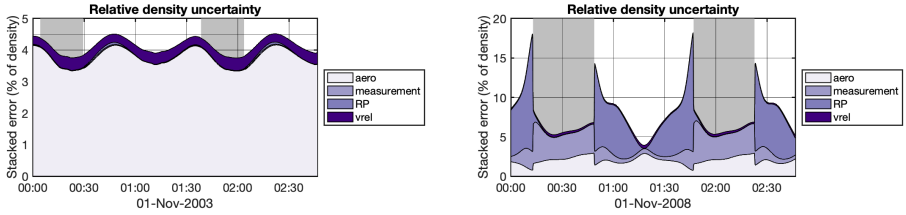

(a) High solar activity.

(b) Low solar activity.

Figure 4.5: Thermosphere density uncertainty as a percent of the density signal. The colours show stacked contributions from parameters related to the radiation pressure (RP), aerodynamic force (aero), accelerometry and GNSS tracking (measurement), and uncertainty in the relative velocity (vrel) for high solar activity (a) and low solar activity (b).

Figure 4.6 shows the magnitude of the thermosphere density together with the total uncertainty (shaded area around the central curve). It can be seen that even though the magnitude of the density signal is higher on 1-Nov-2003, the relative uncertainty is lower in comparison to 1-Nov-2008.

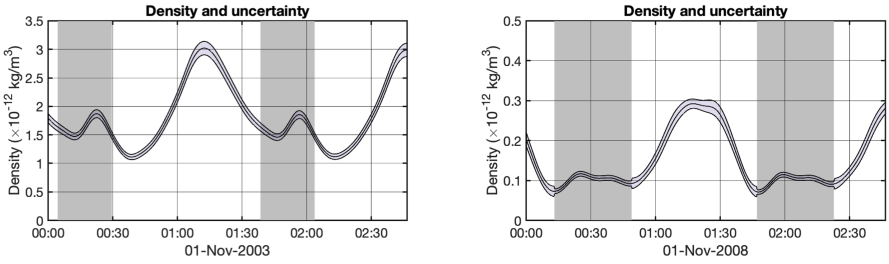

(a) High solar activity.

(b) Low solar activity.

Figure 4.6: GRACE-B thermosphere density and its uncertainty. The black solid line depicts the thermosphere density, while the shaded area around the curve represents the uncertainty (one standard deviation).

Figure 4.7 depicts the uncertainty in the thermospheric wind for GRACE-B. Since the wind is derived based on the dual-axis, direct algorithm, which relies on both along-track and cross-track acceleration as well as the relative velocity, the uncertainty is not proportional to the magnitude of the signal, as it was for the density (Fig. 4.5). During the period of high solar activity (Fig. 4.7a), both along-track and cross-track signals obtained from accelerometer measurements are strong, allowing the wind retrieval algorithm to derive meaningful wind data. The wind uncertainty for this period ranges from 30 m s^{-1} to 110 m s^{-1}, while the wind signal oscillates between 100 m s^{-1} close to the equator and up to 600 m s^{-1} around the poles. This indicates a high level of confidence in the wind data. In this case, the main contributor is the radiation pressure uncertainty, which varies depending on whether the satellite is in sunlight or in the eclipse. The pattern observed in the measurement error originates from variations in the signal-to-noise ratio between the dayside and nightside.

For the low solar activity period (Fig. 4.7b), the aerodynamic signal is very weak, making the wind retrieval algorithm susceptible to small errors in the sideways accelerations (E. Doornbos et al., 2010). This results in an overestimation of the wind signal (visible as red patches in Figure 4.2), which is reflected in the error bars ranging from 200 m s^{-1} to 550 m s^{-1}. This case highlights the importance of error quantification to identify periods when the wind dataset may be unreliable and, therefore, should be flagged as such.

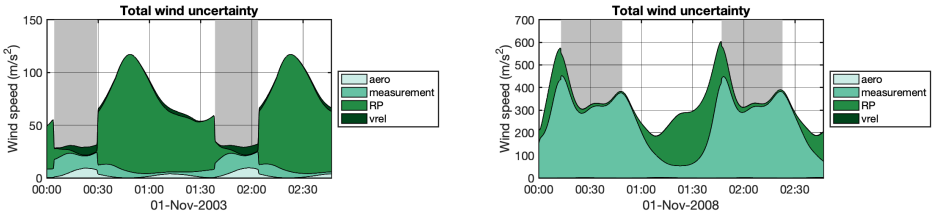

(a) High solar activity

(b) Low solar activity

Figure 4.7: Wind uncertainty for the stacked contributions from parameters related to the radiation pressure (RP), aerodynamic force (aero), accelerometry and GNSS tracking (measurement) and uncertainty in the relative velocity (vrel) for high solar activity (a) and low solar activity (b).

4

4.4.2. RELATIVE VELOCITY AND PARAMETERS RELATED TO THE AERODYNAMIC FORCE

The uncertainty quantification can be further expanded by examining the contributions of specific parameters from the groups described above. In this section, we performed the sensitivity analysis of the parameters related to aerodynamic forces and relative velocity. Figure 4.8 illustrates the impact of the uncertainty of these parameters on density uncertainty. In November 2003, the total uncertainty arose almost entirely from errors in aerodynamic modelling and relative velocity, so Figure 4.8a resembles the shape of the previously shown Figure 4.5a. However, it now provides a clear insight into the origins of the uncertainties. Among the aerodynamic parameters, the largest contributor is the standard deviation in atmospheric temperature (T_{atm}), followed by the uncertainty in the energy accommodation coefficient (α_E), relative velocity (v_{r}), and panel area (A_n). Parameters such as satellite mass and the uncertainty in the atmospheric mass density of constituents (grouped as "other") contribute less than 5%.

Figure 4.8b shows the parameter contribution for November 2008 (low solar activity). Because the main source of error for this period is radiation pressure uncertainty (now set to zero), Figure 4.8b differs in shape from the previously shown Figure 4.5b. The magnitude of error contributions resembles the pattern from 2003, with atmospheric temperature being the most important parameter, although the uncertainty in the atmospheric mass density of constituents now has a noticeable impact. Overall, the total density uncertainty arising from the aerodynamic and relative velocity is approximately 10 times larger during the high solar activity than during the low solar activity. This change is proportional to the magnitude of the density itself, which is approximately 10 times larger during the high solar activity in comparison to the low solar activity (Fig. 4.6)

In summary, the sensitivity analysis for the GRACE-B satellite revealed that errors in atmospheric temperature and the energy accommodation coefficient have the largest impact on density among the aerodynamic parameters during both high and low solar activity. Therefore, special attention should be given when setting the standard deviations of these parameters to ensure realistic error bars for the density dataset.

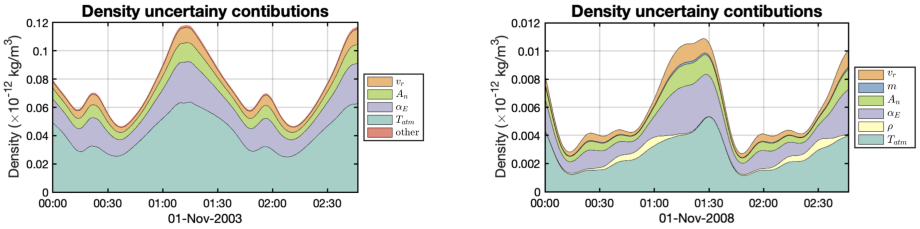

(a) High solar activity.

(b) Low solar activity.

Figure 4.8: Sensitivity analysis of thermospheric density uncertainty for relative velocity and aerodynamic parameters. The acronyms correspond to the following parameters: v_r (relative velocity), m (satellite mass), A_n (panel area), α_E (energy accommodation coefficient), ρ (atmospheric mass density of constituents), and T_{atm} (atmospheric temperature). Parameters contributing less than 5% are grouped under the term "other". Note: for better visibility, the y-axis has been scaled (10x) and differs between the left and the right plot.

4

The same analysis was performed for the GRACE-B wind dataset. Similar to the density, we conducted a sensitivity analysis of the uncertainty in relative velocity and parameters related to aerodynamics. The sinusoidal pattern visible in Figures 4.5a and 4.5b is associated with an increase in wind signal over the southern and northern hemispheres and a decrease in wind speed near the equator. This pattern corresponds to the variations in wind magnitude shown in Figure 4.2. The uncertainty contributions show little difference between high and low solar activity. The magnitude of errors is also similar (up to 22 $\mathrm{m\,s^{-1}}$ during 2003 in comparison to 27 $\mathrm{m\,s^{-1}}$ during 2008).

The parameters that play a major role are the relative velocity (v_r), energy accommodation coefficient (α_E), and panel area (A_n). However, it should be noted that the uncertainties originating from aerodynamics and relative velocity are globally less significant for winds compared to the errors from radiation pressure and measurement noise (Fig. 4.7).

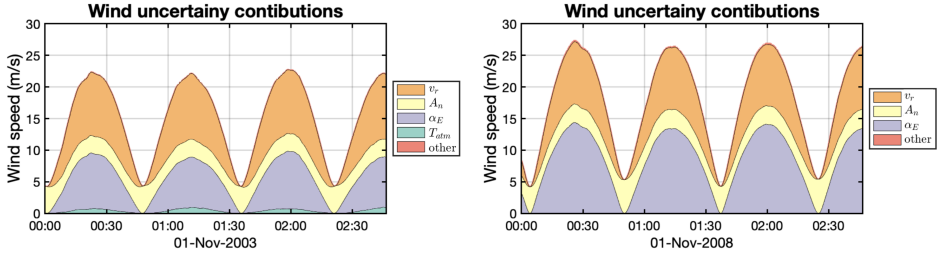

(a) High solar activity.

(b) Low solar activity.

Figure 4.9: Sensitivity analysis of thermospheric wind uncertainty for relative velocity and aerodynamic parameters. The acronyms correspond to the following parameters: v_r (relative velocity), A_n (panel area), α_E (energy accommodation coefficient), and T_{atm} (atmospheric temperature). Parameters contributing less than 5% are grouped under the term "other".

4.4.3. PARAMETERS RELATED TO THE RADIATION PRESSURE

The second group represents the parameters related to the uncertainty in radiation pressure modelling. These can be subdivided into satellite properties, radiation fluxes, radiation pressure model parameters, and thermal model parameters. A visual representation of the grouping of these parameters is provided in Figure 4.10. In this analysis, the remaining parameters, i.e., related to the aerodynamic modelling, measurement noise, as well as the relative velocity, were set to zero.

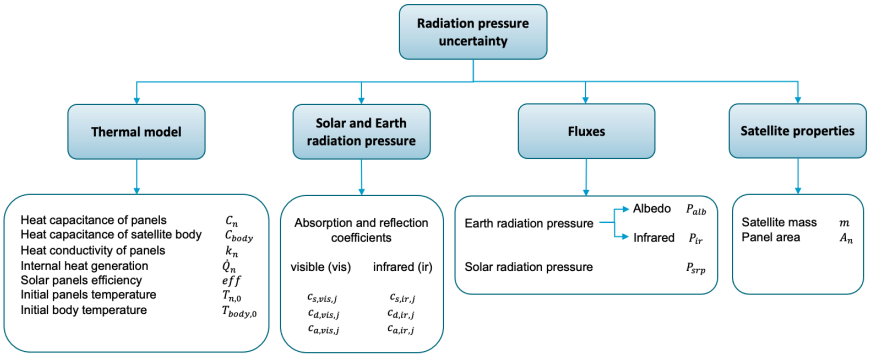

Figure 4.10: Parameters used in the modelling of the radiation pressure uncertainty.

It should be noted that the parameters related to the aerodynamic force affect both the aerodynamic acceleration and the aerodynamic coefficient (C_a). In addition, the relative velocity is directly reflected in the equations used to derive wind and density. Therefore, to assess the influence of the aerodynamic parameters and relative velocity uncertainty, their effect must be evaluated through the density and wind data. In contrast, the radiation pressure parameters influence only the radiation pressure modelling itself; hence, we can analyse their impact directly on the radiation pressure signal rather than on the derived density and wind.

Figure 4.11 illustrates the sensitivity analysis of the radiation pressure uncertainty, taking into account the parameters described previously (Fig. 4.10). Since the radiation pressure acceleration is essentially independent of solar activity, which primarily affects the ultraviolet part of the solar spectrum, the differences observed between 2003 and 2008 are not caused by solar activity but by the satellite illumination, influenced by the angle between the satellite's orbital plane and the direction toward the sun (β'), illustrated in Figure 4.12. On 1 November 2008, the angle was close to 5°, meaning that the Sun vector was nearly aligned with the orbital plane, resulting in a negligible radiation pressure acceleration in the cross-track direction (Fig. 4.11d). In such a scenario, the main uncertainty arises from parameters related to the thermal modelling of the spacecraft. In this case, the heat capacitance of the panels (C_p) generates an uncertainty of up to 2 nm s^{-2}.

In contrast, on 1 November 2003, the angle was approximately 55°, implying that the spacecraft side was illuminated (Fig. 4.11c). Here, the distribution of uncertainty components is more uniform and reaches 6 nm s^{-2}. The impact of the uncertainty in

the absorption and reflection coefficients is almost identical. This can be explained by the fact that the solar flux was split half-and-half into visible and infrared bands while modelling the solar radiation pressure (Hładczuk et al., 2025).

A similar pattern is visible in the along-track direction (Fig. 4.11a and Fig. 4.11b). Here, the uncertainty ranges between 0.1 nm s^{-2} and 1.6 nm s^{-2} on 1 November 2003 ($\beta' \approx 55°$), and reaches 3.2 nm s^{-2} on 1 November 2008 ($\beta' \approx 5°$).

In the radial direction (Fig. 4.11e and Fig. 4.11f), the sensitivity analysis reveals uncertainties up to 6 nm s^{-2} on 1 November 2003 ($\beta' \approx 55°$) and 10.5 nm s^{-2} on 1 November 2008 ($\beta' \approx 5°$), clearly related to the satellite being on Earth's dayside or nightside. In this case, there is a noticeable contribution to the uncertainty in the eclipse from the infrared coefficients (~2 nm s^{-2}). This is caused by uncertainties in the infrared absorption and reflection coefficients used to model the Earth's infrared radiation.

In conclusion, among the parameters related to the radiation pressure uncertainty modelling for GRACE-B, the most impactful group consists of the absorption and reflection coefficients for infrared and visible light. From the thermal modelling perspective, the main contributor is the uncertainty in the heat capacitance. The effects of mismodelling the satellite mass, panel area, and radiation fluxes were negligible. However, the latter may have a slightly higher impact toward the end of the mission, when the satellite's altitude decreases.

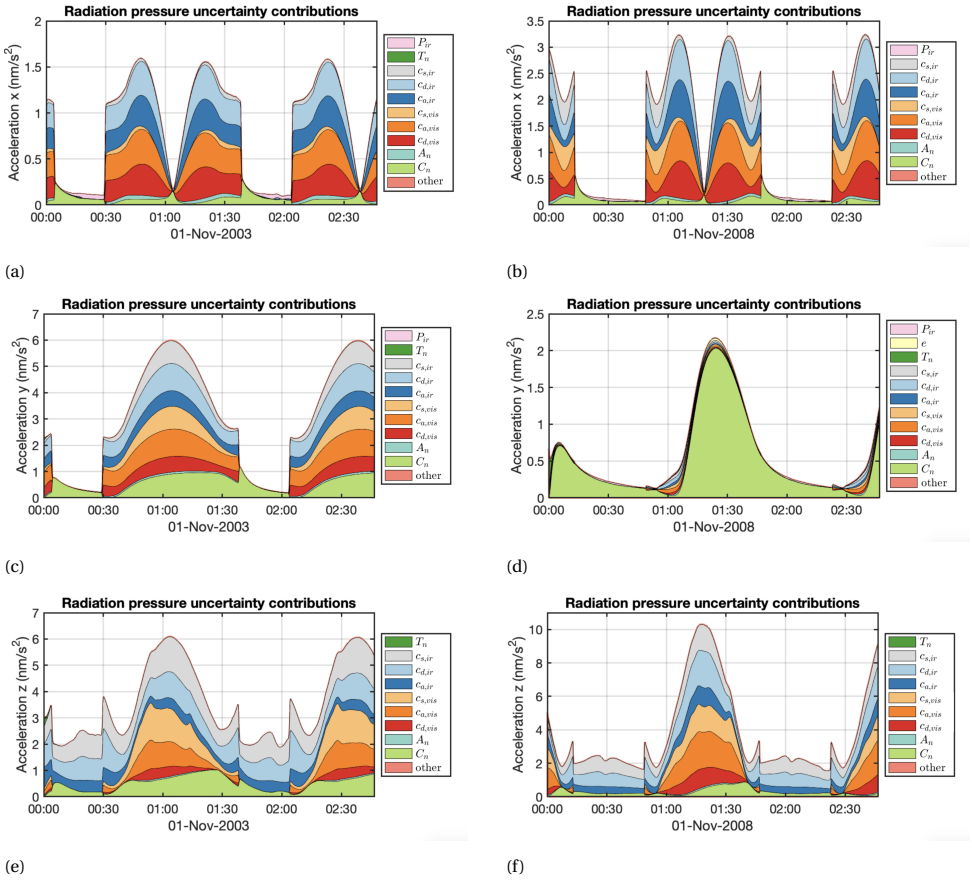

Figure 4.11: Radiation pressure uncertainty contributions. The first row corresponds to the along-track direction (x-axis), the second row to the cross-track direction (y-axis), and the third to the radial direction (z-axis). The first and second columns illustrate two different illumination cases (beta angles): ~55° and ~5°, respectively.

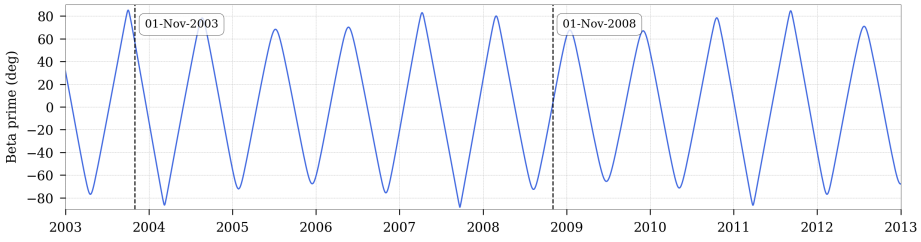

Figure 4.12: Angle between the satellite's orbital plane and the direction toward the sun (β') of the GRACE-B satellite. The vertical lines mark two periods selected for the analysis: 1st of November 2003 (high solar activity; $\beta' \approx 55°$) and 1st of November 2008 (low solar activity; $\beta' \approx 5°$).

To properly interpret the impact of the uncertainty of the radiation pressure parameters, it should be evaluated with respect to the total signal. Figure 4.13 presents the radiation pressure acceleration signal together with its uncertainty (shaded area). The most prominent effect is visible in the cross-track direction. On 1 November 2003, the radiation pressure magnitude reached up to 52 nm s^{-2}, with an uncertainty of 6 nm s^{-2}, which corresponds to roughly 11% of the signal (in sunlight). On the other hand, on 1 November 2008, the radiation pressure acceleration was much smaller, up to 4.3 nm s^{-2}, with an uncertainty of 2 nm s^{-2}, which is almost half of the signal. Previously presented high-level uncertainty analysis of density and wind (Fig 4.5 and Fig. 4.7) showed that during the low solar activity, the radiation pressure contributed significantly to the total uncertainty. Therefore, even though in absolute terms the uncertainty or radiation pressure during the low solar activity is smaller, in relative terms it is much more significant.

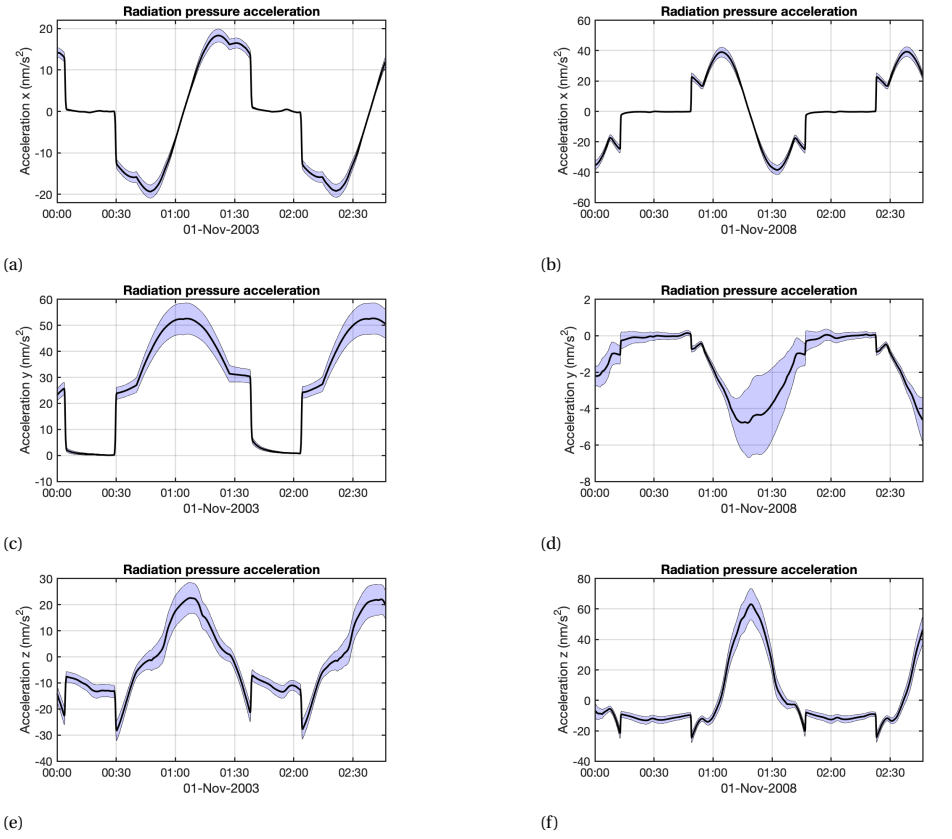

Figure 4.13: Radiation pressure acceleration signal and its uncertainty. The first row corresponds to the along-track direction (x-axis), the second row to the cross-track direction (y-axis), and the third row to the radial direction (z-axis). The black solid line depicts the modelled radiation pressure acceleration, while the shaded area around the curve represents the uncertainty in the modelled signal.

4.5. SUMMARY AND OUTLOOK

In this research, we extended the existing thermospheric density uncertainty to the estimation of the uncertainties in the wind data. The objective of this study was to explore the potential of the propagator to supplement existing datasets with uncertainty information. For this purpose, we performed a sensitivity analysis based on the example of the GRACE-B satellite to assess how changes in the input parameters affect the output wind and density data. These included parameters related to radiation pressure modelling, aerodynamic modelling, measurement noise, and relative velocity. To evaluate the effect of each of these categories individually, we isolated the group by setting the other uncertainties to zero. The initial standard deviations were assigned according to our current best knowledge; however, the output uncertainties can be easily scaled if the input standard deviations change, which makes the sensitivity analysis flexible. Furthermore, we introduced uncertainty in the solar panels' efficiency and implemented the option to divide the solar flux into visible and infrared bands, which was not done in the previous study by Siemes (2024). Splitting the solar flux resulted in almost identical uncertainty contributions from the visible and infrared coefficients. This result can be easily interpreted even if the solar flux is assumed to be fully in the visible range. In such a case, the contribution from the infrared surface coefficients would be approximately replaced by the contribution from the visible coefficients. This is only valid for along-track and cross-track directions, where the Earth's albedo and infrared radiation have negligible effects.

Our analysis shows that the relative uncertainty in the thermospheric density is lower during high solar activity, when the density signal is higher. On the contrary, during low solar activity, when the density is lower, the relative errors are higher.

During periods of high solar activity, the density uncertainty arises mainly from aerodynamic modelling, in particular from the uncertainty in the aerodynamic coefficient, atmospheric temperature, and relative velocity. Under low solar activity conditions, the errors are dominated by radiation pressure. The sensitivity analysis was found to be particularly useful for assessing the errors in the wind datasets. During the period of low solar activity, limitations in the wind derivation algorithm lead to incorrect wind values, which are highly overestimated. This behaviour was well captured by the sensitivity analysis. This will allow us to provide appropriate error bars in future dataset releases and to flag periods of low data fidelity.

Currently, the input uncertainties are treated in a simplistic way, meaning that they are defined as fixed values, whereas in reality, they are more likely to behave as functions. For example, the uncertainty in atmospheric temperature or in the density of the atmospheric constituents would be better represented as a function of solar and geomagnetic activity, magnetic latitude, and local solar time. Similarly, the uncertainty in the solar array efficiency could be expressed as a function of temperature. Another simplification is that, at present, the parameters are assumed to be uncorrelated. Further work could also include replacing the direct wind retrieval algorithm currently used in the propagator with an iterative algorithm (E. Doornbos et al., 2010).

Addressing these challenges will enable the use of the uncertainty propagation tool to augment the existing density and crosswind datasets available on TU Delft Thermo-

sphere HTTPS Server[2] with valuable error information.

[2]https://thermosphere.tudelft.nl/data/

5

CONCLUSION

5.1. GOAL AND RESEARCH QUESTIONS

Each of the individual Chapters 2, 3, and 4 includes conclusions corresponding to its specific content. The objective of this Chapter is to synthesise the answers to the four main research questions and reflect on the research goal, previously defined in Section 1.5. Moreover, Section 5.2 of this Chapter includes recommendations and elaborates on possible future research.

The research questions formulated in this dissertation are answered below:

1. How do various radiation pressure modelling approaches affect the satellite radiation pressure acceleration estimate?

This question was addressed in Chapter 2 based on the example of GRACE-FO. The accuracy of the various radiation pressure models was assessed by comparing the observed and modelled cross-track accelerations, where the observed values were derived from the along-track acceleration and an aerodynamic model. Using this approach was possible due to GRACE-FO's high operational altitude during a period of very low solar activity. Under such conditions, the ratio of radiation pressure to aerodynamic acceleration is high, providing a perfect opportunity to study the effects of radiation pressure modelling since errors from other sources are comparably small.

The radiation pressure model, which performed best, accounted for all advancements, including high fidelity satellite geometry, the surface thermo-optical properties based on the numerical fine-tuning (instead of the mission's handbook), and the satellite thermal inertia. This model resulted in the RMS residual of $0.55\,\mathrm{nm\,s^{-2}}$. Subsequently, the model, which accounted for the thermal inertia but used simplified panel geometry and thermo-optical coefficients from the mission's handbook, resulted in an RMS residual of $1.7\,\mathrm{nm\,s^{-2}}$. Finally, if the satellite thermal emission was ignored, it led to the largest residual between observed and modelled cross-track accelerations (RMS of $4.22\,\mathrm{nm\,s^{-2}}$). Ultimately, the selection of an appropriate radiation pressure model de-

pends on the required level of accuracy. Achieving the accuracy below 1 nm s^{-2} requires sophisticated radiation pressure modelling techniques, such as detailed satellite geometry, good knowledge of the thermo-optical surface properties and thermal emission based on the thermal inertia. For applications where such accuracy is not necessary, a simple panel model with instantaneous heat re-radiation may be sufficient.

Another analysis performed for the GRACE-FO and GOCE satellites (Chapter 3) investigated a modelling approach, which assumed the solar flux is split equally between the visible and infrared bands. For both satellites, splitting the solar flux increased the modelled radiation pressure acceleration in the cross-track direction by 4 nm s^{-2} for GOCE, and 3 nm s^{-2} for GRACE-FO. The along-track acceleration slightly decreased for both satellites, and the radial component remained unaffected.

2. What thermal emission modelling accuracy can be achieved using the data from the satellite on-board thermistors, and what are the associated limitations?

The accuracy of the thermal emission modelling using the data from on-board thermistors was investigated separately for GRACE-FO (Chapter 2) and GOCE (Chapter 3).

To reproduce the outer panels' temperatures, the model based on thermal inertia was developed. Afterwards, the in-situ measurements from the onboard thermistors were used to verify the modelling accuracy. For both satellites, a uniform panel temperature was assumed.

For the GRACE-FO satellite, the thermistors were placed in several external locations (on the solar panels) and inner locations (below the insulation foils). In this analysis, only the sensors located externally were used because the external surface temperatures are relevant for the acceleration due to the satellite's thermal emission. Each solar panel was equipped with two thermistors, with a measured temperature difference of 10 K (which translates to 0.6 nm s^{-2} in the acceleration domain). Since the thermal emission is proportional to the fourth power of the absolute temperature, the satellite panels generate most thermal emission while being the hottest. The difference between modelled and measured thermal emission acceleration generated by the solar panels was the smallest when the satellite was in the sunlight (0.1 nm s^{-2}), and the largest in the penumbra region (0.3 nm s^{-2}).

The largest temperature differences in the penumbra region were measured between the portside and the starboard side, likely caused by asymmetrical heating and cooling of these panels, which in this research were assumed to have the same thermal properties.

The majority of the GOCE thermistors were installed on the inner side of the panels, making them unsuitable for direct comparison to the modeled outside temperature. The wings at the top and bottom of the GOCE satellite were the exception, where the pair of thermistors was placed on each wing on the side facing cold space (away from the Sun). The difference between the measurements of the pair of thermistors located on the same panel was negligible. The difference between measured Earth-facing and Earth-opposed temperatures was around 10 K. The thermal emission modelling accounted for the heat transfer through the satellite wing, replicating the thermistor measurements with an accuracy of approximately 3 K in the sunlight and 15 K in the shadow.

For GRACE-FO, the difference between the modelled and measured temperatures had roughly the same magnitude as the differences between measurements of the ther-

mistors located on the same panel. For GOCE, the difference between the modelled and measured temperatures was of a similar order of magnitude to the differences between measurements from the Earth-facing and Earth-opposed wings (both facing the cold space). This indicates that the maximum achievable modelling accuracy was reached, given the assumptions of a uniform panel temperature and identical thermal properties for both solar arrays.

The main limitation associated with using the onboard thermistors was their placement. The sensors located on the inner side of the panel or below the insulation foil did not reflect the outer temperature, which is a prerequisite for thermal emission modelling. This limitation was encountered in the case of GRACE-FO, GOCE, as well as for other missions such as GRACE. Another limitation came from the limited number of sensors on a single panel. In case only a pair of thermistors is accessible, it is unclear whether the difference between their readings is a measurement error, an actual temperature gradient, or originates from an external heat source such as a radiator.

3. What is the impact of enhanced radiation pressure and thermal emission modelling on the thermosphere mass density and wind?

The effect of enhanced radiation pressure and thermal emission modelling on the thermosphere density and wind can be best assessed when the radiation pressure acceleration is large compared to the aerodynamic acceleration. This occurs during periods of low solar activity and becomes more pronounced at higher altitudes.

Chapter 3 quantifies the impact of the radiation pressure and thermal emission on GOCE wind observations. Replacing the panel model with the high-fidelity geometry resulted in up to $5\,\mathrm{m\,s^{-1}}$ decrease in the wind speed. The largest local decrease of up to $40\,\mathrm{m\,s^{-1}}$ resulted from introducing the thermal model. Finally, splitting the solar flux into the visible and infrared bands further reduced the estimated wind by up to $8\,\mathrm{m\,s^{-1}}$ on the dayside. According to the literature, GOCE observations overestimate the wind speed in comparison to other measurement techniques, so their reduction is considered an improvement.

The effects of the radiation pressure modelling and thermal emission modelling on the GRACE-FO cross-track acceleration have been addressed in Question 1. These are directly reflected in the wind datasets, for which improvement in the cross-track acceleration enhanced the quality of wind data, and enabled the release of datasets that were previously unreleased due to poor quality.

The comparison between the newly and previously published versions of GRACE-FO thermosphere density data, performed using the mean density ratio, did not show significant scale differences (Chapter 2). This is expected since both datasets share the same aerodynamic model and differ only in the radiation pressure and thermal emission, which tend to average to zero in the yearly mean. The agreement between the observed density variability and the NRLMSIS 2.0 and DTM20202 models was assessed using the annual standard deviation. However, this comparison was inconclusive due to the limited accuracy of the models with respect to the changes in the radiation pressure. The effect of the radiation pressure and thermal emission modelling on GOCE density was negligible due to the strong aerodynamic acceleration at the low mission altitude (Chapter 3).

However, it was also shown in the example of GRACE-B, that the effect of the radiation pressure mismodelling on density can be significant (up to 10% of the standard deviation) for certain illumination conditions and while using the satellite panel model (Chapter 4).

4. Which parameters are the most impactful drivers on the thermosphere mass density and winds uncertainty?

The impact of various modelling parameters on thermosphere mass density and wind uncertainty was investigated in Chapter 4. The sensitivity analysis was performed based on the GRACE-B satellite and, thus, the answer to this question may differ for satellites with other orbital characteristics. For both density and wind data, two cases were analysed: low and high solar activity. These two cases also differed in the Sun-satellite geometry. For the low solar activity, the Sun vector was nearly aligned with the orbital plane, whereas for the high solar activity, the spacecraft's side was illuminated. These facts must be considered when drawing conclusions.

For the thermosphere density, the total relative uncertainty was higher during the low solar activity (up to 18%) in comparison to the period of high solar activity (up to 4.5%). For high solar activity, the majority of the uncertainty came from the aerodynamic parameters, where the largest contributor was the uncertainty in the atmospheric temperature, followed by the uncertainty in the energy accommodation coefficient. Unsurprisingly, in the analysed case of low solar activity, radiation pressure errors dominated during sunlight phases, while measurement noise became more significant during eclipse passes. It should be noted that the solar radiation pressure contribution to the uncertainty depends mainly on the orientation of the satellite with respect to the Sun. In the cross-track direction, the solar radiation pressure contribution to the uncertainty was the largest when the satellite was illuminated from the side. On the other hand, when the Sun vector was aligned with the orbital plane, the along-track uncertainty was the largest, and the cross-track negligible. This effect was more prominent in the cross-track direction due to the larger side area in comparison to the front/rear area.

For the thermosphere wind, during high solar activity, the uncertainty ranged from $30\,\mathrm{m\,s^{-1}}$ to $110\,\mathrm{m\,s^{-1}}$, arising mainly from mismodelling of the radiation pressure. During the low solar activity, the low aerodynamic signal prevents the derivation of meaningful wind data, resulting in large uncertainty between $200\,\mathrm{m\,s^{-1}}$ to $550\,\mathrm{m\,s^{-1}}$, with the largest contributor being the aerodynamic parameters, in particular the relative velocity and energy accommodation coefficient.

The parameters related to the radiation pressure were investigated separately. The research showed that the majority of errors originated from the uncertainty in the thermo-optical coefficients of surface materials, followed by the heat capacitance of the solar panels. Ultimately, the relative importance of the parameters related to the radiation pressure and aerodynamic accelerations depends on the ratio between these two signals, which will vary depending on the satellite altitude and solar activity.

Following the research questions answered above, the overarching research goal was achieved:

The goal of this dissertation is to improve the accelerometer-derived thermosphere mass density and wind datasets of the GRACE-FO and GOCE satellites by advancing the modelling of radiation pressure and satellite thermal emission.

This dissertation addressed several knowledge gaps in the field of radiation pressure modelling, including optimising and updating the thermo-optical coefficients describing the satellite surface materials and thermal properties, the usage of thermistor data to validate the thermal models, and the sensitivity analyses for quantifying the sources of uncertainty in thermospheric density and wind datasets.

Following these advancements, the thermospheric density and wind datasets from the GRACE-FO and GOCE satellites were reprocessed and made freely available to the scientific community (TU Delft Thermosphere HTTPS Server[1]). The published data also include the radiation pressure and high-fidelity geometry models of these satellites.

5.2. OUTLOOK FOR FUTURE RESEARCH

This section outlines the possible directions for future research, based on the conclusions of this dissertation. The key recommendations and open issues are listed below:

- **Select realistic standard deviations for the uncertainty propagation.**

  At the current stage of development of the uncertainty propagation tool, the standard deviations describing the uncertainties of the parameters are handled in a simplistic manner. Future investigation is needed to establish the realistic values for these parameters. This includes accounting for correlations and dependencies between the parameters describing atmospheric conditions and gas-surface interaction, as well as variables such as solar and geomagnetic activity, magnetic latitude, and local solar time. Moreover, uncertainties in satellite properties, such as panel area, thermal properties, and reflection and absorption coefficients, are currently treated in a generic manner. In future work, these values should be adjusted to match the characteristics of a specific mission.

- **Supplement the in-situ thermosphere mass density and wind observations with the uncertainty information.**

  At present, accelerometer-derived in-situ thermosphere mass density and wind observations are provided without comprehensive uncertainty information. After selecting realistic standard deviations for the specific satellite, the next step would be to supplement the observations of Swarm, GRACE, GRACE-FO, GOCE, and CHAMP with uncertainty information. This will allow us to identify periods of low data quality, flagging issues such as overestimated wind data during the low solar activity. Additionally, it will enable better comparisons between observations and models and facilitate easier data assimilation. The uncertainty propagation tool could also be used to evaluate the quality of thermosphere density and wind data for currently operating and future missions.

[1] https://thermosphere.tudelft.nl/data/

- **Equipping future Earth-observing missions with thermistors for scientific use.**

  Access to measurements of the satellite's thermistors on its outer surfaces, providing information on the panels' exact temperature, is a prerequisite for accurate thermal emission modelling. Existing missions are equipped with housekeeping thermistors used for the spacecraft thermal monitoring and control. These sensors are mounted at various locations on the outer and inner panels, as well as within the satellite body, to monitor and maintain the instruments' appropriate temperature. Equipping future Earth-observing missions with thermistors intended for scientific use would enable more accurate and robust thermal emission modelling. Such sensors should be redundant, located at multiple places on the outer surfaces of the satellite panels.

  Besides the temperature sensors, the radiation pressure model would benefit from more extensive information on the satellite thermo-optical surface properties. It is, thus, recommended that the manufacturers provide a comprehensive list of the satellite materials and their properties in the satellite's handbooks, as well as the technical drawings or CAD models of the satellite's outer geometry for scientific use.

- **Expand from panel model to finite element model to overcome the limitation of uniform panel temperature.**

  The most accurate way to model satellite thermal emission is to use a finite element model. In this technique, the panels are discretised into small volumes, and an energy balance is solved for each element, accounting for heat transfer to neighbouring volumes and heat exchange through the panel surfaces. Provided the thermistors' measurements were available, the material properties could be tuned, and the outer panels' temperature across the whole surface will be known. This would overcome the current limitation of assuming a uniform panel temperature and instead account for thermal gradients across the surface. Incorporating such a model, however, would significantly increase computational effort. The trade-off between computational complexity and the potential gain in thermal emission modelling accuracy could be a path for future research.

- **Modelling the impact of surface degradation on radiation pressure acceleration estimate**

  During its operational lifetime, the satellite's surface is exposed to different environmental effects, resulting in surface degradation and thinning of the material coatings. Atomic oxygen causes erosion and surface roughness, resulting in irreversible changes in thermo-optical surface properties. Exposure to the UV radiation causes optical changes and material opacity. The solar arrays are particularly sensitive to UV degradation, which darkens the cell's cover glass, increasing solar array temperature and reducing cell performance. In mission handbooks, environmental effects are usually accounted for by providing the absorption and reflection coefficients of materials at the beginning and end of the satellite's life, separately. Modelling the impact of the environmental factors on the thermo-optical

surface properties is expected to increase the accuracy of the radiation pressure acceleration estimate.

- **Use the Clouds and the Earth's Radiant Energy System (CERES) for the Earth's outgoing radiation modelling.**

  In our current processing pipeline for in-situ thermosphere mass density and wind, Earth's outgoing fluxes are modelled using monthly-averaged maps from the Earth Radiation Budget Experiment (ERBE). On the other hand, the uncertainty propagation tool uses the CERES project's Energy Balanced and Filled (EBAF) Top-Of-Atmosphere (TOA) all-sky fluxes. However, instead of the available monthly maps, the tool utilises averaged maps. The advantage of using such averaged maps is that one is independent of the latency of the CERES data. In future work, more climatologically accurate approximations of CERES data or even the CERES data themselves could be incorporated. The CERES data account for land, ocean, clouds, aerosols, snow, ice, and surface type. This could lead to improved accuracy in radiation pressure modelling, particularly for satellites at lower altitudes, potentially improving vertical wind estimates and enabling better numerical optimisation of the surface thermo-optical coefficients of nadir-facing panels.

BIBLIOGRAPHY

Adhya, S. (2005). *Thermal Re-Radiation Modelling for the Precise Prediction and Determination of Spacecraft Orbits* [PhD Thesis.]. Department of Geomatic Engineering, University College London.

Andreis, D., & Canuto, E. S. (2005). Drag-Free and Attitude Control for the GOCE Satellite. *Proceedings of the 44th IEEE Conference on Decision and Control*, 3851–3856. https://doi.org/10.1109/CDC.2005.1582794

Aruliah, A. L., Farmer, A. D., Rees, D., & Brandstrøm, U. (1996). The seasonal behaviour of high-latitude thermospheric winds and ion velocities observed over one solar cycle. *Journal of Geophysical Research*, *101*(A10), 15701–15711. https://doi.org/10.1029/96JA00538

Barreto-Schuler, C. W., Shepherd, G. G., Chen, Y., & Shepherd, M. G. (2021). Observations and modeling of strong thermospheric winds at high latitudes and their impact on the lower thermosphere. *Journal of Geophysical Research: Space Physics*, *126*(11). https://doi.org/10.1029/2021ja029658

Battaglia, D., Cataloglu, A., & Dolce, S. (2008). *GOCE thermal balance / vacuum test* (tech. rep. No. 2008-01-2034). SAE International. https://doi.org/10.4271/2008-01-2034

Bettadpur, S. (2012). *Gravity recovery and climate experiment: Product specification document* (Technical report No. GRACE 327-720). Center for Space Research, The University of Texas at Austin.

Bettadpur, S. V. (2007). *Gravity Recovery and Climate Experiment Product Specification Document (Rev. 4.5 – February 20, 2007)* (tech. rep. No. GRACE 327-720/CSR-GR-03-02). Center for Space Research, The University of Texas at Austin.

Bhattarai, S., Ziebart, M., Springer, T., Gonzalez, F., & Tobias, G. (2022a). High-precision physics-based radiation force models for the Galileo spacecraft. *Advances in Space Research*, *69*, 4141–4154. https://doi.org/10.1016/j.asr.2022.04.003

Bhattarai, S., Ziebart, M., Springer, T., Gonzalez, F., & Tobias, G. (2022b). High-precision physics-based radiation force models for the Galileo spacecraft. *Advances in Space Research*, *69*(12), 4141–4154. https://doi.org/10.1016/j.asr.2022.04.003

Bock, H., Jäggi, A., Beutler, G., & Meyer, U. (2014). GOCE: precise orbit determination for the entire mission. *Journal of Geodesy*, *88*(11), 1047–1060. https://doi.org/10.1007/s00190-014-0742-8

Bowman, B. R., Tobiska, W. K., Marcos, F. A., & Valladares, C. (2008). The JB2006 empirical thermospheric density model. *Journal of Atmospheric and Solar-Terrestrial Physics*, *70*, 774–793. https://doi.org/10.1016/j.asr.2023.12.059

Bruinsma, S. (2014). The DTM-2013 thermosphere model. *Journal of Space Weather and Space Climate*, *5*. https://doi.org/10.1051/swsc/2015001

Bruinsma, S., & Biancale, R. (2003). Total densities derived from accelerometer data. *Journal of Spacecraft and Rockets*, *40*(2), 230–236. https://doi.org/10.2514/2.3937

Bruinsma, S., & Boniface, C. (2021). The operational and research DTM-2020 thermosphere models. *Journal of Space Weather and Space Climate*, *11*(3). https://doi.org/10.1051/swsc/2021032

Bruinsma, S., Siemes, C., Emmert, J. T., & Mlynczak, M. G. (2022). Description and comparison of 21st century thermosphere data. *Advances in Space Research*. https://doi.org/10.1016/j.asr.2022.09.038

Cataloglu, A., Weimer, L., Eckert, K., Pieper, B., & Battaglia, D. (2004). *Micro-vibration verification of GOCE thermal hardware* (tech. rep. No. 2004-01-2390). SAE International. https://doi.org/10.4271/2004-01-2390

Christophe, B., Boulanger, D., Foulon, B., Huynh, P. A., Lebat, V., Liorzou, F., & Perrot, E. (2015). A new generation of ultra-sensitive electrostatic accelerometers for GRACE Follow-On and towards the next generation gravity missions. *Acta Astronautica*, *117*, 1–7. https://doi.org/10.1016/j.actaastro.2015.06.021

Dhadly, M., Emmert, J., Drob, D., Conde, M., Doornbos, E., Shepherd, G., Makela, J., Wu, Q., Niciejewski, R., & Ridley, A. (2017). Seasonal dependence of northern high-latitude upper thermospheric winds: A quiet time climatological study based on ground-based and space-based measurements. *Journal of Geophysical Research: Space Physics*, *122*(2), 2619–2644. https://doi.org/10.1002/2016JA023688

Dhadly, M. S., Emmert, J. T., Drob, D. P., Conde, M. G., Aruliah, A., Doornbos, E., Shepherd, G. G., Wu, Q., Makela, J. J., Niciejewski, R. J., Lee, C., Jee, G., & Ridley, A. J. (2019). HL-TWiM Empirical Model of High-Latitude Upper Thermospheric Winds. *Journal of Geophysical Research: Space Physics*, *124*(12), 10592–10618. https://doi.org/10.1029/2019JA027188

Dhadly, M. S., Emmert, J. T., Drob, D. P., Conde, M. G., Doornbos, E., Shepherd, G. G., Makela, J. J., Wu, Q., Nieciejewski, R. J., & Ridley, A. J. (2018). Seasonal Dependence of Geomagnetic Active-Time Northern High-Latitude Upper Thermospheric Winds. *Journal of Geophysical Research: Space Physics*, *123*(1), 739–754. https://doi.org/10.1002/2017JA024715

Dhadly, M. S., Emmert, J. T., Jones, M., Doornbos, E., Zawdie, K. A., Drob, D. P., & Conde, M. G. (2020). Oscillations in Neutral Winds Observed by GOCE. *Geophysical Research Letters*, *47*(17). https://doi.org/10.1029/2020GL089339

Doornbos, E. (2011). *Thermospheric Density and Wind Determination From Satellite Dynamics* [PhD Thesis.]. Department of Astrodynamics and Satellite Missions, Delft University of Technology.

Doornbos, E., Bruinsma, S., Fritsche, B., Koppenwallner, G., Visser, P., van den IJssel, J., & de Teixeira de Encarnação, J. (2014). *ESA contract 4000102847/nl/el, GOCE+ theme 3: Air density and wind retrieval using GOCE data – final report* (tech. rep.). TU Delft. https://earth.esa.int/eogateway/documents/20142/1181177/GOCE-theme-3-final-report.pdf

Doornbos, E., Scharroo, R., Klinkrad, H., Zandbergen, R., & Fritsche, M. (2002). *Improved modelling of surface forces in the orbit determination of ERS and ENVISAT* (tech. rep.).

Doornbos, E., Van Den IJssel, J., Lühr, H., Förster, M., & Koppenwallner, G. (2010). Neutral density and crosswind determination from arbitrarily oriented multiaxis accelerometers on satellites. *Journal of Spacecraft and Rockets*, *47*(4), 580–589. https://doi.org/10.2514/1.48114

Drinkwater, M., Haagmans, R., Muzzi, D., Popescu, A., Floberghagen, R., Kern, M., & Fehringer, M. (2007). The GOCE gravity mission: ESA's first core explorer. *3rd GOCE User Workshop, 6–8 November 2006, Frascati, Italy*, 1–7.

Drob, D. P., Emmert, J. T., Crowley, G., Picone, J. M., Shepherd, G. G., Skinner, W., Hays, P., Niciejewski, R. J., Larsen, M., She, C. Y., Meriwether, J. W., Hernandez, G., Jarvis, M. J., Sipler, D. P., Tepley, C. A., O'Brien, M. S., Bowman, J. R., Wu, Q., Murayama, Y., … Vincent, R. A. (2008). An empirical model of the Earth's horizontal wind fields: HWM07. *Journal of Geophysical Research: Space Physics*, *113*(12). https://doi.org/10.1029/2008JA013668

Drob, D. P., Emmert, J. T., Meriwether, J. W., Makela, J. J., Doornbos, E., Conde, M., Hernandez, G., Noto, J., Zawdie, K. A., McDonald, S. E., Huba, J. D., & Klenzing, J. H. (2015). An update to the Horizontal Wind Model (HWM): The quiet time thermosphere. *Earth and Space Science*, *2*(7), 301–319. https://doi.org/10.1002/2014EA000089

Duan, B., & Hugentobler, U. (2022). Estimating surface optical properties and thermal thrust for Galileo satellite body and solar panels. *GPS Solutions*, *26*(4). https://doi.org/10.1007/s10291-022-01324-1

Dumontel, M. (2010). *GOCE stand-alone aerodynamic model how-to* (tech. rep. No. GOTN AI-0179) (Issue 1). Thales Alenia Space.

Dutch Space. (2005). *GOCE Design Definition Document* (tech. rep. No. GO-RP-DUS-0002) (Issue 4). Dutch Space. Leiden, The Netherlands.

Dutch Space. (2006). *GOCE solar array: Detailed thermal model analysis* (tech. rep. No. GO-RP-DUS-0004) (Issue 4). Dutch Space. Leiden, The Netherlands.

Emmert, J. T. (2015). Thermospheric mass density: A review. *Advances in Space Research*, *56*(5), 773–824. https://doi.org/10.1016/j.asr.2015.05.038

Emmert, J. T., Dhadly, M. S., Mlynczak, M. G., et al. (2021). NRLMSIS 2.0: A Whole-Atmosphere Empirical Model of Temperature and Neutral Species Densities. *Earth and Space Science*, *8*(3). https://doi.org/10.1029/2020EA001321

Emmert, J. T., Fejer, B. G., Shepherd, G. G., & Solheim, B. H. (2001). Climatology of middle- and low-latitude daytime F region disturbance neutral winds measured by WINDII. *Journal of Geophysical Research: Space Physics*, *106*(A11), 24701–24712. https://doi.org/10.1029/2000JA000372

Emmert, J. T., Jones, M. J., Siskind, D. E., Drob, D. P., Picone, J. M., Stevens, M. H., Bailey, S. M., Bender, S., Bernath, P. F., Funke, B., Hervig, M. E., & Pérot, K. (2022). NRLMSIS 2.1: An empirical model of nitric oxide incorporated into MSIS. *Journal of Geophysical Research: Space Physics*, *127*(10). https://doi.org/10.1029/2022JA030896

Fang, T.-W., Kubaryk, A., Goldstein, D., Li, Z., Fuller-Rowell, T., Millward, G., Singer, H. J., Steenburgh, R., Westerman, S., & Babcock, E. (2022). Space Weather Environment During the SpaceX Starlink Satellite Loss in February 2022. *Space Weather*, *20*(11). https://doi.org/10.1029/2022SW003193

Farrés, A., Blaes, B., Vigneron, J., & Verma, A. K. (2023). Solar Radiation Pressure. In R. Hevner et al. (Eds.), *Next generation cubesats and smallsats* (pp. 329–345). Elsevier. https://doi.org/10.1016/B978-0-12-824541-5.00019-4

Fehringer, M., André, G., Lamarre, D., & Maeusli, D. (2008). A Jewel in ESA's Crown – GOCE and its Gravity Measurement Systems. *ESA Bulletin*, (133), 14–23.

Fitzpatrick, D. J., Sutton, E. K., Pilinski, M. D., & Palo, S. E. (2025). Harnessing Satellite Constellations as Signals of Opportunity for an Enhanced Specification of the Satellite Drag Environment in the Critical LEO Regime. *Authorea Preprint*. https://doi.org/10.22541/au.176244733.31846582/v1

Floberghagen, R., Fehringer, M., Lamarre, D., Muzi, D., Frommknecht, B., Steiger, C., Piñeiro, J., & da Costa, A. (2011a). Mission design, operation and exploitation of the Gravity Field and Steady-State Ocean Circulation Explorer mission. *Journal of Geodesy*, *85*, 749–758. https://doi.org/10.1007/s00190-011-0498-3

Floberghagen, R., Fehringer, M., Lamarre, D., Muzi, D., Frommknecht, B., Steiger, C., Piñeiro, J., & da Costa, A. (2011b). Mission design, operation and exploitation of the gravity field and steady-state ocean circulation explorer mission. *Journal of Geodesy*, *85*(11), 749–758. https://doi.org/10.1007/s00190-011-0498-3

Flury, J., Bettadpur, S., & Tapley, B. D. (2008). Precise accelerometry onboard the grace gravity field satellite mission. *Advances in Space Research*, *42*(8), 1414–1423. https://doi.org/10.1016/j.asr.2008.05.004

Förster, M., Haaland, S. E., & Doornbos, E. (2011). Thermospheric vorticity at high geomagnetic latitudes from CHAMP data and its IMF dependence. *Annales Geophysicae*, *29*(1), 181–186. https://doi.org/10.5194/angeo-29-181-2011

Förster, M., Rentz, S., Köhler, W., Liu, H., & Haaland, S. E. (2008). Imf dependence of high-latitude thermospheric wind pattern derived from champ cross-track measurements. *Annales Geophysicae*, *26*(6), 1581–1595. https://doi.org/10.5194/angeo-26-1581-2008

Fortescue, P., Swinerd, G., & Stark, J. (2011a). *Spacecraft systems engineering, 4th edition*. Wiley.

Fortescue, P., Swinerd, G., & Stark, J. (2011b). *Spacecraft Systems Engineering* (4th). John Wiley & Sons. https://doi.org/10.1002/9781119971009

Fortescue, P. W., Swinerd, G. G., & Stark, J. P. W. (Eds.). (2011). *Spacecraft Systems Engineering* (4th ed.). John Wiley & Sons. https://onlinelibrary.wiley.com/doi/book/10.1002/9781119971009

Gath, P. (2016). *Entwicklung, Integration und Test der GRACE Follow-On Satelliten* (tech. rep.). Airbus Defence and Space GmbH. Friedrichshafen, Germany.

Gold, R. E., Bushman, S. S., McAdams, J. V., Williams, K. E., et al. (2017). Maximizing *MESSENGER*'s Science Return with Technologies and Innovation [Johns Hopkins University Applied Physics Laboratory]. *JHU/APL Technical Digest*, *34*(1), 34-01-34–12. https://www.jhuapl.edu/sites/default/files/2024-09/34-01-Gold.pdf

Harvey, N., McCullough, C. M., & Save, H. (2022). Modeling GRACE-FO accelerometer data for the version 04 release. *Advances in Space Research*, *69*(3), 1393–1407. https://doi.org/10.1016/j.asr.2021.10.056

He, J., Astafyeva, E., Yue, X., Pedatella, N. M., Lin, D., Fuller-Rowell, T. J., Fedrizzi, M., Codrescu, M., Doornbos, E., Siemes, C., Bruinsma, S., Pitout, F., & Kubaryk, A. (2023). Comparison of Empirical and Theoretical Models of the Thermospheric Density Enhancement During the 3–4 February 2022 Geomagnetic Storm. *Space Weather*, *21*(9). https://doi.org/10.1029/2023SW003521

Hładczuk, N. A., van den IJssel, J., Jacobs, F., Siemes, C., & Visser, P. (2025). Solar and thermal radiation pressure modelling for improving the GOCE horizontal wind dataset.

Advances in Space Research, *76*(11), 6899–6917. https://doi.org/10.1016/j.asr.2025.09.043

Hładczuk, N. A., van den IJssel, J., Kodikara, T., Siemes, C., & Visser, P. (2024). GRACE-FO radiation pressure modelling for accurate density and crosswind retrieval. *Advances in Space Research*, *73*(5), 2355–2373. https://doi.org/10.1016/j.asr.2023.12.059

Innis, J. L., & Conde, M. (2002). High-latitude thermospheric vertical wind activity from Dynamics Explorer 2 Wind and Temperature Spectrometer observations: Indications of a source region for polar cap gravity waves. *Journal of Geophysical Research*, *107*(A8), 1172. https://doi.org/10.1029/2001JA009130

Kenneally, P. W., & Schaub, H. (2020). Fast spacecraft solar radiation pressure modeling by ray tracing on graphics processing unit. *Advances in Space Research*, *65*, 1951–1964. https://doi.org/10.1016/j.asr.2019.12.028

Kessler, D. J., & Cour-Palais, B. G. (1978). Collision Frequency of Artificial Satellites: The Creation of a Debris Belt. *Journal of Geophysical Research*, *83*(A6), 2637–2646. https://doi.org/10.1029/JA083iA06p02637

Killeen, T., & Roble, R. G. (1992). Neutral winds in the lower thermosphere from Dynamics Explorer 2. *Geophysical Research Letters*, *19*(11), 1093–1096. https://doi.org/10.1029/92GL01023

Killeen, T., Roble, R. G., Smith, R. W., Spencer, N. W., Meriwether, J. W., Rees, D., Hernandez, G., Hays, P. B., Cogger, L. L., Sipler, D. P., Biondi, M. A., & Tepley, C. A. (1986). Mean neutral circulation in the winter polar F-region. *Journal of Geophysical Research*, *91*, 1633–1649. https://doi.org/10.1029/JA091iA02p01633

Killeen, T., Wu, Q., Solomon, S. C., Ortland, D. A., Skinner, W. R., Niciejewski, R. J., & Gell, D. A. (2006). TIMED Doppler Interferometer: Overview and recent results. *Journal of Geophysical Research: Space Physics*, *111*(A10S01). https://doi.org/10.1029/2005JA011484

Killeen, T. L., & Roble, R. G. (1984). An analysis of the high-latitude thermospheric wind pattern calculated by a thermospheric general circulation model: 1. Momentum forcing. *Journal of Geophysical Research: Space Physics*, *89*(A9), 7509–7522. https://doi.org/10.1029/ja089ia09p07509

Klinkrad, H., Koeck, C., & Renard, P. (1991). Key features of a satellite skin force modelling technique by means of monte-carlo ray tracing. *Advances in Space Research*, *11*(6), 147–150. https://doi.org/10.1016/0273-1177(91)90244-E

Knipp, D. J., Tobiska, W. K., & Emery, B. A. (2004). Direct and indirect thermosphere heating sources for solar cycle 21–23. *Solar Physics*, *224*, 495–505. https://doi.org/10.1007/s11207-005-5008-0

Kodikara, T. (2023). The open time-series of the high-resolution ionosphere-thermosphere aeronomic climate simulation (OTHITACS). https://doi.org/10.26050/WDCC/OTHITACS_TIEGCM

Kornfeld, R. P., Arnold, B. W., Gross, M. A., Dahya, N. T., Klipstein, W. M., Gath, P. F., & Bettadpur, S. (2019). GRACE-FO: The gravity recovery and climate experiment follow-on mission. *Journal of Spacecraft and Rockets*, *56*, 931–951. https://doi.org/10.2514/1.A34326

Kraft. (1988). A software package for sequential quadratic programming. Tech. Rep. DFVLR-FB 88-28, DLR German Aerospace Center — Institute for Flight Mechanics,

Koln, Germany. *Wiss. Berichtswesen d. DFVLR, 1988*. https://books.google.nl/books?id=4rKaGwAACAAJ

Landerer, F. W., Flechtner, F. M., Save, H., Webb, F. H., Bandikova, T., Bertiger, W. I., Bettadpur, S. V., Byun, S. H., Dahle, C., Dobslaw, H., Fahnestock, E., Harvey, N., Kang, Z., Kruizinga, G. L., Loomis, B. D., McCullough, C., Murböck, M., Nagel, P., Paik, M., … Yuan, D. N. (2020). Extending the Global Mass Change Data Record: GRACE Follow-On Instrument and Science Data Performance. *Geophysical Research Letters*, *47*(12). https://doi.org/10.1029/2020GL088306

Larsen, M., & Meriwether, J. (2012). Vertical winds in the thermosphere. *Journal of Geophysical Research: Space Physics*, *117*(A9). https://doi.org/10.1029/2012JA017843

Li, Z., Ziebart, M., Bhattarai, S., Harrison, D., & Grey, S. (2018). Fast solar radiation pressure modelling with ray tracing and multiple reflections. *Advances in Space Research*, *61*(9), 2352–2365. https://doi.org/10.1016/J.ASR.2018.02.019

Liu, H., Foster, B. T., Hagan, M. E., McInerney, J. M., Maute, A., Qian, L., Richmond, A. D., Roble, R. G., Solomon, S. C., Garcia, R. R., Kinnison, D., Marsh, D. R., Smith, A. K., Richter, J., Sassi, F., & Oberheide, J. (2010). Thermosphere extension of the Whole Atmosphere Community Climate Model. *Journal of Geophysical Research: Space Physics*, *115*(12). https://doi.org/10.1029/2010JA015586

Liu, H., Doornbos, E., & Nakashima, J. (2016). Thermospheric wind observed by GOCE: Wind jets and seasonal variations. *Journal of Geophysical Research: Space Physics*, *121*(7), 6901–6913. https://doi.org/10.1002/2016JA022938

Lühr, H., Ritter, P., Liu, H., & Häusler, K. (2007). Average thermospheric wind patterns over the polar regions, as observed by CHAMP. *Annales Geophysicae*, *25*, 1093–1101. https://doi.org/10.5194/angeo-25-1093-2007

Lühr, H., Park, J., Ritter, P., & Liu, H. (2011). In-situ CHAMP observation of ionosphere-thermosphere coupling. *Space Science Reviews*, *168*(1-4), 237–260. https://doi.org/10.1007/s11214-011-9798-4

March, G., Doornbos, E. N., & Visser, P. (2019). High-fidelity geometry models for improving the consistency of CHAMP, GRACE, GOCE and Swarm thermospheric density data sets. *Advances in Space Research*, *63*(1), 213–238. https://doi.org/10.1016/j.asr.2018.07.009

March, G., Visser, T., Visser, P., & Doornbos, E. N. (2019). CHAMP and GOCE thermospheric wind characterization with improved gas-surface interactions modelling. *Advances in Space Research*, *64*(6), 1225–1242. https://doi.org/10.1016/j.asr.2019.06.023

Mehta, P. M., Linares, R., & Sutton, E. K. (2019). Data-Driven Inference of Thermosphere Composition During Solar Minimum Conditions. *Space Weather*, *17*(9), 1364–1379. https://doi.org/10.1029/2019SW002264

Mehta, P. M., Linares, R., & Sutton, E. K. (2018). A Quasi-Physical Dynamic Reduced Order Model for Thermospheric Mass Density via Hermitian Space-Dynamic Mode Decomposition. *Space Weather*, *16*(5), 569–588. https://doi.org/10.1029/2018SW001840

Mehta, P. M., Paul, S. N., Crisp, N. H., Sheridan, P. L., Siemes, C., March, G., & Bruinsma, S. (2023). Satellite drag coefficient modeling for thermosphere science and mission operations. *Advances in Space Research*, *72*(12), 5443–5459. https://doi.org/10.1016/j.asr.2022.05.064

Mishra, R., Militky, J., & Venkataraman, M. (2018, January). Nanoporous materials. In *Nanotechnology in textiles: Theory and application* (pp. 311–353). Elsevier. https://doi.org/10.1016/B978-0-08-102609-0.00007-9

Molina, I., & Scherliess, L. (2023). Spatial and temporal correlations of thermospheric zonal winds from GOCE satellite observations. *Frontiers in Astronomy and Space Sciences*, *10*. https://doi.org/10.3389/fspas.2023.1214591

Montenbruck, O., Steigenberger, P., & Hugentobler, U. (2015). Enhanced solar radiation pressure modeling for Galileo satellites. *Journal of Geodesy*, *89*(3), 283–297. https://doi.org/10.1007/s00190-014-0774-0

Mutschler, S., Tobiska, W. K., Pilinski, M., Bruinsma, S. L., Sutton, E., Knipp, D., Mallik, V., Jagatia, B., Siegers, M., Fang, T.-W., Fuller-Rowell, T., diLorenzo, B., Casali, S., Siemes, C., & Wahl, K. (2023). A Survey of Current Operations-Ready Thermospheric Density Models for Drag Modeling in LEO Operations. *Proceedings of the Advanced Maui Optical and Space Surveillance Technologies Conference (AMOS)*. https://amostech.com/TechnicalPapers/2023/Atmospherics_Space-Weather/Mutschler.pdf

NASA GRACE Fact Sheet (tech. rep.). (2004) (Accessed: 2026-02-07). https://science.nasa.gov/earth/earth-observatory/grace-fact-sheet/

Niciejewski, R. J., Wu, Q., Skinner, W. R., Gell, D. A., Cooper, M., Marshall, A., Killeen, T. L., Solomon, S. C., & Ortland, D. A. (2006). TIMED Doppler Interferometer on the Thermosphere–Ionosphere–Mesosphere Energetics and Dynamics satellite: data product overview. *Journal of Geophysical Research: Space Physics*, *111*(A11S90). https://doi.org/10.1029/2005JA011513

Olsen, N., Friis-Christensen, E., Floberghagen, R., Alken, P., Beggan, C. D., et al. (2013). The Swarm Satellite Constellation Application and Research Facility (SCARF) and Swarm data products. *Earth, Planets and Space*, *65*(11), 1189–1200. https://doi.org/10.5047/eps.2013.07.001

O'Shaughnessy, D. J., McAdams, J. V., Williams, K. E., & Page, B. R. (2009). Fire Sail: MESSENGER's Use of Solar Radiation Pressure for Accurate Mercury Flybys. *Proceedings of the 32nd American Astronautical Society/AIAA Guidance, Navigation, and Control Conference*, *134*, 1527–1539. https://messenger.jhuapl.edu/Resources/Publications/AAS09-014.pdf

Paetzold, H. K., & Zschörner, H. (1961). An Annual and a Semiannual Variation of the Upper Air Density. *Pure and Applied Geophysics*, *48*, 85–92. https://doi.org/10.1007/BF01993333

Parker, W. E., & Linares, R. (2024). Satellite Drag Analysis During the May 2024 Gannon Geomagnetic Storm. *61*(5), 1412–1416. https://doi.org/10.2514/1.A36164

Peymirat, C. (1998). A magnetosphere-thermosphere-ionosphere electrodynamics general circulation model. *Journal of Geophysical Research: Space Physics*, *103*(A8), 17467–17477. https://doi.org/10.1029/98ja01235

Picone, J. M., Hedin, A. E., Drob, D. P., & Aikin, A. C. (2002). NRLMSISE-00 empirical model of the atmosphere: Statistical comparisons and scientific issues. *Journal of Geophysical Research: Space Physics*, *107*(A12). https://doi.org/10.1029/2002JA009430

Qian, L., Solomon, S. C., & Kane, T. J. (2009). Seasonal variation of thermospheric density and composition. *Journal of Geophysical Research: Space Physics*, *114*. https://doi.org/10.1029/2008JA013643

Rees, D., Fuller-Rowell, T., & Smith, R. W. (1980). Measurements of high latitude thermospheric winds by rocket and ground-based techniques and their interpretation using a three-dimensional time-dependent dynamical model. *Planetary and Space Science*, *28*, 919–932.

Reigber, C., Lühr, H., & Schwintzer, P. (2002). CHAMP mission status. *Advances in Space Research*, *30*(2), 129–134. https://doi.org/10.1016/S0273-1177(02)00276-4

Richmond, A. D., Lathuillere, C., & Vennerstroem, S. (2003). Winds in the high-latitude lower thermosphere: Dependence on the interplanetary magnetic field. *Journal of Geophysical Research: Space Physics*, *108*(A2). https://doi.org/10.1029/2002ja009493

Richmond, A. D., Ridley, E. C., & Roble, R. G. (1992). A thermosphere/ionosphere general circulation model with coupled electrodynamics. *Geophysical Research Letters*, *19*(6), 601–604. https://doi.org/10.1029/92GL00401

Robertson, R. V., Earle, G. D., Bailey, S. M., Shinpaugh, K. A., Scales, W. A., Shoemaker, M. A., & Black, J. T. (2015). *Highly Physical Solar Radiation Pressure Modeling During Penumbra Transitions* [Doctoral dissertation, Virginia Polytechnic Institute and State University].

Siemes, C. (2024). *Uncertainty specification and analysis for thermosphere observations (usato)*. 4TU.ResearchData. https://doi.org/10.4121/08c86d28-e44e-496d-a3b3-185ec43475d4

Siemes, C. (2019). *ESA UNCLASSIFIED-Releasable to the Public Title Swarm satellite thermo-optical properties and external geometry Issue Number 2 Revision Number 0* (tech. rep.). Delft University of Technology. Delft, Netherlands.

Siemes, C., Borries, C., Bruinsma, S., Fernandez-Gomez, I., Hładczuk, N., den IJssel, J., Kodikara, T., Vielberg, K., & Visser, P. (2023). New thermosphere neutral mass density and crosswind datasets from CHAMP, GRACE, and GRACE-FO. *Journal of Space Weather and Space Climate*, *13*, 16. https://doi.org/10.1051/swsc/2023014

Siemes, C., van den IJssel, J., & Visser, P. (2024). Uncertainty of thermosphere mass density observations derived from accelerometer and GNSS tracking data. *Advances in Space Research*. https://doi.org/10.1016/j.asr.2024.02.057

Silverman, E. M. (1995). *Space Environmental Effects on Spacecraft: LEO Materials Selection Guide, Part 1* (tech. rep. No. NASA CR-4661, Part 1). TRW Space & Electronics. One Space Park, Redondo Beach, CA.

Spencer, N. W., Theis, R. F., Wharton, L. E., & Carignan, G. R. (1976). Local vertical motions and kinetic temperature from AE-C as evidence for aurora-induced gravity waves. *Geophysical Research Letters*, *3*(6), 313–316. https://doi.org/10.1029/GL003i006p00313

Storz, M. F. (2005). High Accuracy Satellite Drag Model (HASDM). *Advances in Space Research*, *36*(12), 2499–2506. https://doi.org/10.1016/j.asr.2004.02.020

Sutton, E. K. (2018). A new method of physics-based data assimilation for the quiet and disturbed thermosphere. *Space Weather*, *16*, 736–753. https://doi.org/10.1002/2017SW001785

Sutton, E. K., S., N. R., & Forbes, J. M. (2007). Density and Winds in the Thermosphere Deduced from Accelerometer Data. *Journal of Spacecraft and Rockets*, *44*, 1210–1219. https://doi.org/10.2514/1.28641

Swartz, W. E., Rohrbaugh, J. L., & Nisbet, J. S. (1972). A thermospheric model from satellite orbital decay densities and incoherent-scatter temperatures. *Planetary and Space Science*, *20*(10), 1685–1697. https://doi.org/10.1016/0021-9169(72)90036-0

Tapley, B. D., Bettadpur, S., Watkins, M., & Reigber, C. (2004). The gravity recovery and climate experiment: Mission overview and early results. *Geophysical Research Letters*, *31*(9). https://doi.org/10.1029/2004GL019920

Touboul, P., Rodrigues, M. S., Foulon, B., Reynaud, S., de la Torre, A., & Sandford, M. C. (1999). Electrostatic space accelerometers for present and future applications. *Acta Astronautica*, *45*(1-9), 741–748. https://doi.org/10.1016/S0094-5765(99)00132-0

Valentini, D., Vacance, M., Battaglia, D., Pieper, B., & Niot, J.-M. (2006). *GOCE instrument thermal control* (tech. rep. No. 2006-01-2044). SAE International. https://doi.org/10.4271/2006-01-2044

van Helleputte, T., Doornbos, E., & Visser, P. (2009). Champ and grace accelerometer calibration by gps-based orbit determination. *Advances in Space Research*, *43*(11), 1890–1896. https://doi.org/10.1016/j.asr.2009.02.017

van den IJssel, J., Doornbos, E., Iorfida, E., March, G., Siemes, C., & Montenbruck, O. (2020). Thermosphere densities derived from Swarm GPS observations. *Advances in Space Research*, *65*(7), 1758–1771. https://doi.org/10.1016/j.asr.2020.01.004

Vielberg, K., & Kusche, J. (2020). Extended forward and inverse modeling of radiation pressure accelerations for LEO satellites. *Journal of Geodesy*, *94*(4). https://doi.org/10.1007/s00190-020-01368-6

Vielberg, K., Peter, H., Kusche, J., & Löcher, A. (2025). Updated radiation pressure force modeling and validation: case studies for GRACE and Sentinel-6 MF. *Journal of Geodesy*, *99*(10). https://doi.org/10.1007/s00190-025-02000-1

Vigue, Y., Schutz, B. E., & Abusali, P. A. M. (1994). Thermal Force Modelling for Global Positioning System Satellites Using the Finite Element Method. *Journal of Spacecraft and Rockets*, *31*(5), 855–859. https://doi.org/10.2514/3.26503

Visser, P., & van den IJssel, J. A. (2016). Calibration and validation of individual GOCE accelerometers by precise orbit determination. *Journal of Geodesy*, *90*(1), 1–13. https://doi.org/10.1007/s00190-015-0850-0

Visser, T., March, G., Doornbos, E., de Visser, C., & Visser, P. (2019). Horizontal and vertical thermospheric cross-wind from GOCE linear and angular accelerations. *Advances in Space Research*, *63*(10), 3139–3153. https://doi.org/10.1016/j.asr.2019.01.030

Wang, W., Burns, A., & Liu, J. (2021, January). Upper Thermospheric Winds: Forcing, Variability, and Effects. In *Space physics and aeronomy, upper atmosphere dynamics and energetics* (pp. 41–63). wiley. https://doi.org/10.1002/9781119815631.ch3

Wang, Y., Li, M., Jiang, K., Li, W., Zhao, Q., Fang, R., Wei, N., & Mu, R. (2023). Improving Precise Orbit Determination of LEO Satellites Using Enhanced Solar Radiation Pressure Modeling. *Space Weather*, *21*(1). https://doi.org/10.1029/2022SW003292

Witasse, O., Lilensten, J., Lathuillere, C., & Pibraret, B. (1998). Meridional thermospheric neutral wind at high latitude over a full solar cycle. *Annales Geophysicae*, *16*, 1400–1409. https://doi.org/10.1007/s00585-998-1400-9

Wolff, M. (1969). Direct Measurement of the Earth's Gravitational Potential Using a Satellite Pair. *Journal of Geophysical Research*, *74*(22), 5295–5300.

Wöske, F., Kato, T., Rievers, B., & List, M. (2019). GRACE accelerometer calibration by high precision non-gravitational force modeling. *Advances in Space Research*, *63*(3), 1318–1335. https://doi.org/10.1016/j.asr.2018.10.025

Ying, H., Kruizinga, W. G., Paik, M., Landerer, F., Bertiger, W., Sakumura, C., Bandikova, T., & Mccullough, C. (2019). *Gravity Recovery and Climate Experiment Follow-On (GRACE-FO) Level-1 Data Product User Handbook Revision History* (tech. rep.). NASA Jet Propulsion Laboratory, California Institute of Technology.

Ziebart, M. (2004). Generalized analytical solar radiation pressure modeling algorithm for spacecraft of complex shape. *Journal of Spacecraft and Rockets*, *41*(5), 840–848. https://doi.org/10.2514/1.13097

CURRICULUM VITÆ

Natalia Anna HŁADCZUK

30-06-1993 Born in Katowice, Poland

EDUCATION

2021–2026 **PhD in Aerospace Engineering**
Delft University of Technology, The Netherlands
Department of Astrodynamics & Space Missions
Thesis: *Advanced radiation pressure modelling for improving the satellite thermosphere density and wind observations*

2016–2017 **Master of Science in Automatic Control and Robotics**
Silesian University of Technology, Gliwice, Poland
Thesis: *Automatic identification of celestial object's spectral lines from line feature catalogue acquired by Herschel Space Observatory*

2012–2016 **Bachelor of Science in Automatic Control and Robotics**
Silesian University of Technology, Gliwice, Poland
Thesis: *Interactive application based on augmented reality technology*

2009–2012 **Liceum Ogólnokształcące**
III Liceum Ogólnokształcące im. Adama Mickiewicza, Katowice, Poland

WORK EXPERIENCE

2018–2020 **Software Developer (Mechanisms)**
Gran Telescopio de Canarias, S.A.
Tenerife, Spain

2017–2018 **Young Graduate Trainee**
European Space Agency, European Space Astronomy Centre
Madrid, Spain

2016 **Trainee**
European Space Agency, European Space Astronomy Centre
Madrid, Spain

2015 **Trainee**
Septentrio Satellite Navigation N.V.
Leuven, Belgium

AWARDS

2025 **Outstanding Paper Award for Young Scientists**
(for the work of Chapter 1)
Committee On Space Research (COSPAR)

List of Publications

Journal Publications

6. **N. A. Hładczuk**, J. van den IJssel, F. Jacobs, C. Siemes, P. Visser, *Solar and thermal radiation pressure modelling for improving the GOCE horizontal wind dataset*, Advances in Space Research (2025).

5. **N. A. Hładczuk**, J. van den IJssel, T. Kodikara, C. Siemes, P. Visser, *GRACE-FO radiation pressure modelling for accurate density and crosswind retrieval*, Advances in Space Research **73**(5), 2355–2373 (2024).

4. C. Siemes, C. Borries, S. Bruinsma, I. Fernandez-Gomez, **N. Hładczuk**, J. van den IJssel, T. Kodikara, K. Vielberg, P. Visser, *New thermosphere neutral mass density and crosswind datasets from CHAMP, GRACE, and GRACE-FO*, Journal of Space Weather and Space Climate **13**, 16 (2023).

3. C. S. Benson, **N. Hładczuk**, L. D. Spencer, A. Robb, J. P. Scott, I. Valtchanov, R. Hopwood, D. A. Naylor, *The Herschel SPIRE Fourier Transform Spectrometer Spectral Feature Finder III. Line Identification and Off-Axis Spectra*, Monthly Notices of the Royal Astronomical Society **496**, 4906 (2020).

2. J. P. Scott, **N. Hładczuk**, L. D. Spencer, I. Valtchanov, C. S. Benson, R. Hopwood, *The Herschel SPIRE Fourier Transform Spectrometer Spectral Feature Finder II. Estimating Radial Velocity of SPIRE Spectral Observation Sources*, Monthly Notices of the Royal Astronomical Society **496**, 4891 (2020).

1. R. Hopwood, I. Valtchanov, L. D. Spencer, J. P. Scott, C. S. Benson, N. Marchili, **N. Hładczuk**, E. T. Polehampton, N. Lu, G. Makiwa, D. A. Naylor, B. G. Gom, G. Noble, M. J. Griffin, *The Herschel SPIRE Fourier Transform Spectrometer Spectral Feature Finder I. The Spectral Feature Finder and Catalogue*, Monthly Notices of the Royal Astronomical Society **496**, 4874 (2020).

Selected conference presentations

7. **N. A. Hładczuk**, Oral presentation: *Augmenting thermosphere mass density and crosswind observations derived from accelerometer and GNSS tracking data with uncertainty information*, ESA Living Planet Symposium 2025, 23/06/2025 – 27/06/2025, Vienna, Austria.

6. **N. A. Hładczuk**, J. van den IJssel, C. Siemes, P. Visser, Poster: *Improving GOCE wind datasets by advancing solar radiation pressure and thermal emission modelling*, European Space Weather Week 2024, 04/11/2024 – 08/11/2024, Coimbra, Portugal.

5. **N. A. Hładczuk**, Sabin Anton, J. van den IJssel, C. Siemes, P. Visser, Oral presentation: *Lessons learned from Swarm radiation pressure modelling for improving GOCE neutral thermosphere crosswind data products*, Swarm 10 Year Anniversary Science Conference 2024, 08/04/2024 – 12/04/2024, Copenhagen, Denmark.

4. **N. A. Hładczuk**, Oral presentation: *Radiation pressure modelling for improving neutral thermosphere density and crosswind data products*, European Space Weather Week 2023, 20/11/2023 – 24/11/2023, Toulouse, France.

3. **N. A. Hładczuk**, J. van den IJssel, C. Siemes, P. Visser, Poster: *Radiation pressure modelling for improving the thermosphere density and cross-wind data products*, Swarm 12th Data Quality Workshop, 10/10/2022 – 14/10/2022, Uppsala, Sweden.

2. **N. A. Hładczuk**, Oral presentation: *Radiation pressure modelling for improving the thermosphere density data products*, COSPAR Scientific Assembly, 16/07/2022 – 24/07/2022, Athens, Greece.

1. **N. A. Hładczuk**, J. van den IJssel, C. Siemes, P. Visser, Poster: *Improved radiation pressure modelling for the Swarm satellites*, Living Planet Symposium 2022, 23/05/2022 – 27/05/2022, Bonn, Germany.

ACKNOWLEDGEMENTS

I would like to dedicate this section to the people who supported me throughout these years. To start, I want to thank my promotor Pieter and my daily supervisor, Christian, for choosing me for the PhD position. Besides being experts in the field, you both were always approachable and open to listening to any concerns. I could not have imagined better supervisors, and this achievement would not have been possible without your support.

Pieter, thank you for your scientific guidance and for sharing your enthusiasm, especially during my work with GOCE. Thanks for reminding me that *perfect is the enemy of good* (particularly when it comes to writing).

Thank you, Christian, for all your support and help throughout this work, which is difficult to capture in a single paragraph. You were always responsive, available whenever a meeting was needed, and made me focus on understanding things over simply getting them done. Our meetings always helped me clarify my thoughts, get new ideas, and motivated me. Thank you for your kindness, empathy, and for always knowing when well-being should take priority over work. You also kept surprising me with themed mugs after each chapter, featuring the most important findings. Now, along with this dissertation, I also have a new mug collection to showcase my research!

I want to thank the other members of the TU Delft Thermosphere Group: Jose, João, Miguel, Sabin, and Frederik. It was a pleasure to work together, and I learned so much from each of you. In particular, our weekly meetings were invaluable to get feedback on my work and solve problems. These meetings were also an occasion to catch up, share news, and occasionally enjoy some chocolates (thanks, Jose!). I was looking forward to them each week and always left inspired and with a fresh perspective.

On this note, I would like to give a special thanks to Jose for her support during the preparation of my articles. I appreciate how you always dedicated time to reviewing my work thoroughly, you were inquisitive and made me think more in-depth and noticed details I might have overlooked otherwise. I always enjoyed our little chats and the positive energy you brought to the office.

I want to thank my paranymphs: Sabin and Frederik, with whom I shared not only a research topic and office, but also laughs and discussions about life. Your presence made these years far more enjoyable, and I hope we stay in touch after our time at TU Delft.

During my research, I relied on the work of former PhDs from TU Delft, in particular Günther March and Tim Visser, to whom I reached out several times over the years. Günther, through these years, we met multiple times during conferences, ESA Swarm Workshops, or whenever you visited TU Delft. Thank you for sharing your knowledge on aerodynamic modelling, and, more so, our first talks about life in Delft, which helped me make the final decision to come here.

Tim, thank you for sharing the (massive amount of) GOCE data, and for your time

and patience in answering my questions. Your responsiveness during that time really helped me to progress with the research on GOCE winds.

I would like to acknowledge people from the thermosphere community, in particular Eelco Doornbos, for his extremely useful insights, help, and many inspiring discussions we shared.

At the start of my PhD, I faced a steep learning curve, coming from a different academic background. Thank you, Ron Noomen, for making this task easier. Your lectures on Introduction to Aerospace Engineering were extremely helpful in diving into the new research topic. Your ability to explain complex concepts in an accessible way made the lectures not only very informative but also fun to attend.

Beyond the academic support, my gratitude also goes to Relly van Wingaarden, management assistant in the Space Engineering department, for her invaluable help during the stressful moving period from Spain to the Netherlands. I will always remember her kindness and genuine care.

The days in the office would not have been the same without such fantastic people around. Thank you, my fellow PhD colleagues: Allard, Andrea, Caroline, Emma, Fernando, Jesse, Jonas, Linh, Livio, Luigi, Rania (thank you for being so approachable, it really helped me these last months), Riva (I really enjoyed our coffee chats in LOT), Sam, Tara, Yaël. You made the office such a great place to be, full of kindness and good energy.

I also want to thank my friends: Dimitra and Michelle, as well as my cousin Ela, for their support and for always knowing how to effectively distract me from work.

Chciałabym podziękować moim rodzicom za ogromne wsparcie podczas podejmowania decyzji o doktoracie i podczas jego trwania. Tato, dziękuję Ci za cierpliwość, zainteresowanie szczegółami moich badań, przesyłanie kosmicznych ciekawostek oraz wiarę w moje umiejętności. Mamo, dziękuję za troskę, wsparcie i przypominanie mi, że istnieje życie poza doktoratem. Nasze rozmowy telefoniczne zawsze poprawiały mi humor, nawet po najbardziej chaotycznych dniach w biurze.

Finally, I would like to thank my partner, Nacho. More than five years ago, when I first started thinking about doing a PhD, you not only supported me but also encouraged me to take this step and moved to the Netherlands to make it happen. Thank you for celebrating all of my small victories over these years. Thank you for being there during endless presentation rehearsals, helping as a graphic designer, great personal chef, emotional support, but most importantly, for being such a caring and loving partner.

Last but not least, I would like to acknowledge my own perseverance and dedication, which have carried this work to completion and allowed me to grow both as a researcher and, more importantly, as a person.

Natalia Hładczuk,
Delft, July 2026

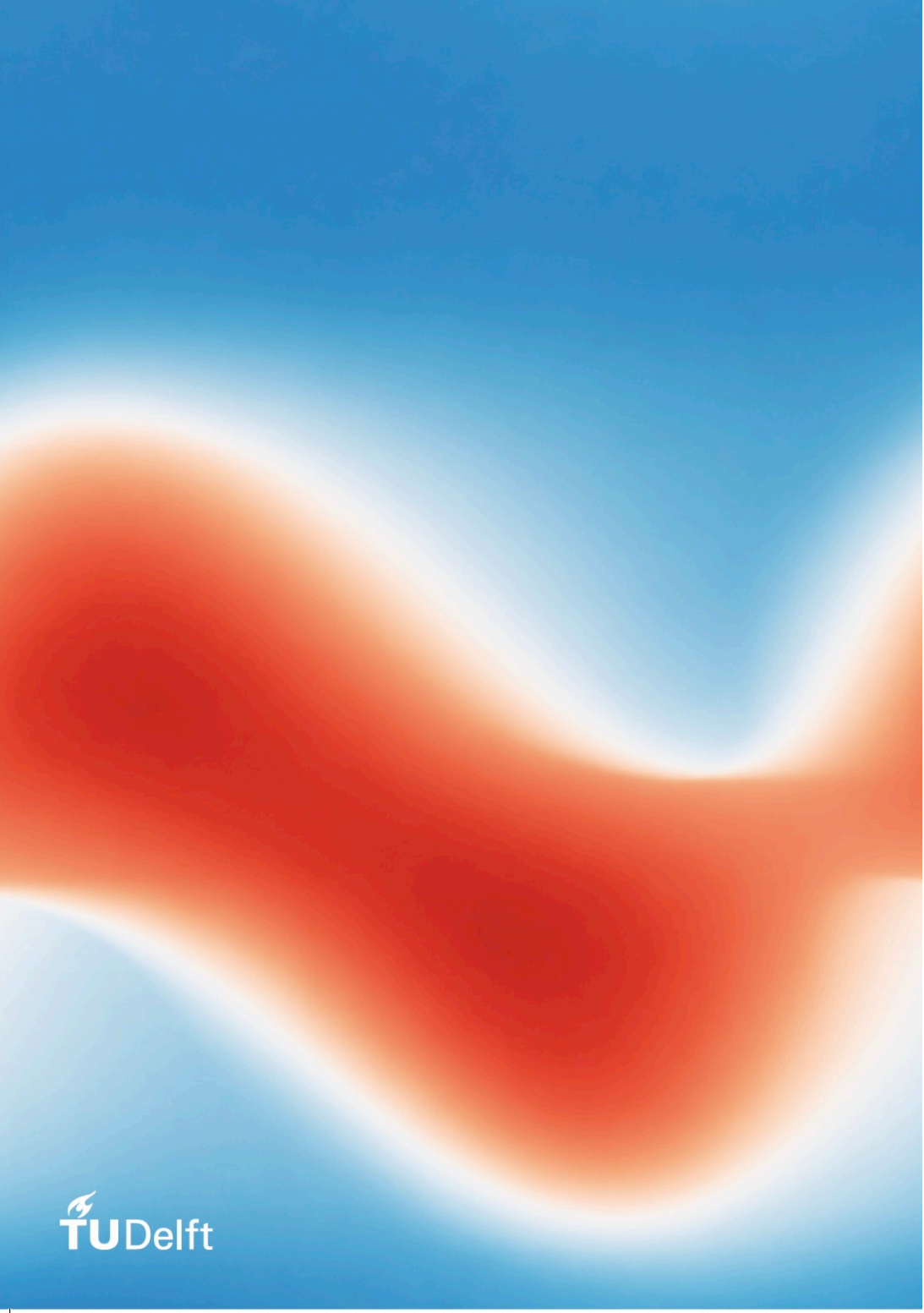
TUDelft